Chapter 1

Introduction

In 1932, the Swedish physicist Arne Olander discovered an interesting phenomenon when working with an alloy of gold (Au) and cadmium (Cd) [1]. The Au-Cd alloy could be plastically deformed when cool and then be heated to return to, or *remember*, the original dimensional configuration. This phenomenon is known as the shape memory effect (SME) and the alloys that exhibit the behavior are called shape memory alloys (SMA). In 1961, a group of U. S. Naval Ordnance Laboratory researchers led by William Beuhler made a significant discovery in the field of SME and SMA. While testing an alloy of Nickel and Titanium for heat and corrosion resistance, they found that it too exhibited the SME. The Ni-Ti SMA proved to be significantly less expensive, easier to work with, and less dangerous (from a health standpoint) than previously discovered alloys. These factors refreshed interest and research in the SME and its applications.

Shape memory alloys consist of a group of metallic materials that demonstrate the ability to return to some previously defined shape or size when subjected to the appropriate thermal stimulus. Some examples of these alloys are Ag-Cd, Au-Cd, Cu-Al-Ni, Cu-Sn, Cu-Zn-(X), In-Ti, Ni-Al, Ni-Ti, Fe-Pt, Mn-Cu, and Fe-Mn-Si. The SME occurs due to a temperature and stress dependent shift in the crystalline structure of the material between two different phases called martensite and austenite. Martensite, named after German metallographer Adolf Martensite, the low temperature phase, is relatively soft whereas austenite, named after English metallurgist William Chandler Austen, the high temperature phase, is relatively hard.

The following is an example of the shape memory effect. When a straight bar made of SMA is in its high temperature (austenitic) phase is allowed to cool below the phase transformation temperature, the crystalline structure will change to martensite. Subsequently, if the bar is deformed and then reheated above the phase transformation temperature, it will return to its original straight configuration. The change that occurs within the SMA crystalline structure during the SME is not thermodynamically reversible. In other words, there is energy dissipation due to internal friction and creation of structural defects. As a result, a temperature hysteresis occurs [1].

Pseudoelasticity effect is the other behavior of shape memory alloy. As an example, when a straight SMA bar is maintained above the phase transformation temperature it can recover seemingly plastic deformations.

Among shape memory alloys that have been discovered thus far, Nickel-Titanium (Ni-Ti)

has proven to be the most flexible and beneficial in engineering applications. The following characteristics of Ni-Ti make it stand out from the other SMAs: greater ductility, more recoverable motion, excellent corrosion resistance (comparable to series 300 stainless steels), stable transformation temperatures, high biocompatibility, and the ability to be electrically heated for shape recovery. [1]

1.1 SMA Actuators

Shape memory alloy actuators provide an interesting alternative to conventional actuation methods. Their advantages, for instance, include drastically reduced size, weight, and complexity of robotic systems. SMA actuators possess an extremely high force to weight ratio. A Ni-Ti actuator can apply an actuation stress of 600 MPa. Therefore, a 150 μm diameter Ni-Ti wire can apply a force of 10.6 N. If the wire is 10 cm long it would weigh 11.4 mg and could contract 0.8 cm [1]. Thus, the actuator can lift an object 94,000 times its own weight nearly 1 cm!

Shape memory alloy actuators also can be made very compact and simple. In the example described above, the actuator itself has a volume of only 0.002 cm^3. An SMA actuator consists only of the SMA element and a heating and cooling method. The cooling method can be a combination of natural convection, conduction, and radiation. The final advantage is noiseless operation. Whereas conventional actuators produce a significant amount of noise, SMA actuators are completely noiseless.

Shape memory alloy actuators do have disadvantages, which must be thoroughly considered and analyzed prior to deciding on their use. First, they operate with a low efficiency. Effectively, an SMA actuator is a heat engine in which the material converts thermal energy into work. Therefore, the efficiency of the actuator cannot be greater than that of the Carnot cycle. The efficiency of the Carnot cycle is low in the temperatures where typical SMA actuators operate–not exceeding 10 percent. Second, SMA actuators operate at a low bandwidth, meaning they are relatively slow to dynamic cycles. The cycling time is primarily dependent on the heat transfer characteristics of the SMA cooling mechanism. The primary parameters that affect bandwidth are the temperature and type of surrounding medium, the convection of the surrounding medium, and the surface to volume ratio of the SMA elements. Depending on the environment, heat dissipation can be a problem. For a high temperature, low convection environment, the heat transfer to the surrounding medium is reduced resulting in a lower bandwidth. For a low temperature or high convection environment, the heat transfer is improved and bandwidth is increased. Greater heat transfer, however, means that more power is needed to achieve actuation temperature [1].

Another disadvantage of SMA actuators is the small absolute strains achieved by the SMA material. With only 8.5 percent strain available (for Ni-Ti), mechanisms actuated by SMA that are required to create large motions must be cleverly designed. Converting small motions into large motions comes with the unavoidable reduction in mechanical advantage. A final disadvantage, and topic of much research, is the difficulty in controlling SMA actuators. The shape memory effect is a highly non-linear phenomenon, which complicates the control

process through hysteresis behavior (as described earlier), non-linear heat transfer, and non-linear changes in parameters that affects the phase composition of the material (temperature, stress). Another control issue is that the entire deflection of an SMA element occurs over a small temperature range, making accurate control in partial contraction difficult [1].

1.2 SMA Applications

Typical SMA applications fall into two large categories based on the specific properties that are considered: superelastic applications and shape memory effect applications. Superelastic (pseudoelastic) properties are used primarily in the biomedical field, for stents, guidewires, orthodontic wires, osteosynthesis, etc. Another typical and important application exploiting these properties is that for eyeglass frames. Shape memory effect, on the other hand, is primarily used in the industrial field for Joule effect actuators, which can take advantage of the stroke, force, and durability characteristics of SMAs. A simple SMA wire can replace an electromagnetic motor, enabling cost savings and design simplicity, especially when simple mechanical movements are required. More effective actuators can be obtained by using SMA wires showing the two-way effect. This kind of actuators can be used, for instance, in locks, both for automotive and several other industrial applications, for electronics-related applications (such as plug-in devices for PCs), for the movement of small parts in toys, and broadly speaking, when a simple mechanical movement is required and space, weight, and cost set severe production constraints. Another important application is related to sensor-

actuators, in which the SMA wire, both in wire and in spring formats, can react to a room temperature change by modifying its shape, and in doing so actuating specific devices, such as sprinklers for fire prevention [2].

SMA Blood-clot filters have been developed that can be easily deformed and inserted in a vein while cold. Upon heating by the body, the filter that is made of NiTi wire, is functionally shaped and anchors itself in the vein and catches the passing clots [3].

Cryofit hydraulic coupling are SMA cylinders made by Raychem Corporation. They are expanded while in martensite phase. When they warm up to austenite they shrink in diameter and strongly hold the tube ends. The tube diameter prevents the SMA sleeve from fully recovering its original shape. The stress created by the sleeve is strong enough to create a joint that, in many ways, is superior to a weld [4].

For force actuation besides robotic applications, SMA materials have been used as circuit board edge connectors. The SMA is biased by a linear spring. In this electrical connector system, when the connector is heated, the SMA component opens the spring. This allows force free insertion or removal of the circuit board. Upon cooling the SMA release the spring that closes tightly the circuit board and forms the connections. SMAs have found other application based on the same idea. One such example is fire safety valves that use an SMA element to shut off the toxic or flammable gas flow when fire occurs [5].

Another class of SMA actuators is designed to use a portion of the shape recovery for accurate positioning. An example of such an actuator is a flow rate control valve. The flow rate is

adjusted by raising the temperature of an SMA component enough to close the valve the desired amount [2].

Pseudoelastic property of shape memory alloys has been used in a number of commercially available products. An example is an eyeglass frame that is made of NiTi. The shape memory alloy can undergo large deformation without damaging the frame. Another example is guide wires for steering catheters that have been developed using NiTi wires into vessels in the body. The guide wire resists permanent deformation if bent severely [3].

SMAs are extremely corrosion resistant, demonstrate excellent biocompatibility, can be fabricated into very small sizes, and have properties of elasticity and force delivery. These properties make these materials a natural candidate for biomedical applications [4].

1.3 SMA Modeling

One of the critical aspects of using SMA is better understanding their behavior for the intended application. To this end, a number of past studies have suggested several models that provide the thermomechanical dynamics of SMA under different heating/cooling and loading scenarios.

SMA models can be classified into three categories:

1. free energy based,
2. history variable, and
3. geometric models.

While the first class of models are physics-based, the models of the third class are solely based on experimental data. The second class models incorporate the martensite fraction as an internal variable. The dependency of this internal variable on the stress and temperature is modeled by a kinetics law. The second class, history variable models are also referred to as the phenomenological model. They are widely used for the engineering applications mainly because their parameters are readily measurable. This group of models also have simpler structures compared to the other two classes which make them more appealing for simulations. Models introduced by Tanaka [6], Liang [7], and Brinson [8] are among the most known and used phenomenological SMA models. These and other models will be explained in more detail in the next chapters.

1.4 Problem Statement

The existing models for one dimensional shape memory alloy materials (e.g., wire) can predict the behavior of the material for simple cases. For complex thermomechanical loadings, however, the behavior predicted by these models does not always match with the experimental results. The main reason for this shortcoming is that the experimental data, commonly used for validating the models, has been exclusively collected in the two following ways. The SMA element is kept under constant stress while the temperature varies, or the temperature is kept constant while the stress loading is changed. These models have been successfully used for open-and-closed-loop simulations of SMA with linear motions for which the stress of

the wire does not change as a result of the actuation; for example, in applications including moving a mass in the vertical direction. It can be shown that, for applications in which the stress of the SMA element changes as a result of the actuation, existing models are not able to accurately predict the behavior of the SMA elements.

1.5 Objectives

The primary objective of this study is to provide more accurate constitutive/kinetics models of SMA and investigate control methods that are more effective than those currently available.

Specifically, we intend to:

1. extend the existing models for one-dimensional Shape Memory Alloy materials such that they can more accurately model the behavior of SMAs,
2. provide models that can predict an accurate representation of SMA behaviors when temperature and stress change simultaneously,
3. conduct a simulation study and a series of experiments to validate the proposed models and document their benefits over the existing models for SMAs, and
4. use the modified models to design the model-based control algorithms.

1.6 Approach

The approach that will be adopted for conducting this research will include performing a literature search to provide a summary of the models and control techniques that have been

suggested for SMAs. Next, we will use a simple simulation model (a rotary one-degree-of-freedom robotic arm) in which the stress and temperature of an SMA wire is changed simultaneously, in order to highlight the shortcomings of existing constitutive models. The numerical simulations are repeated experimentally, using a hanging-mass and also a rotary manipulator with one-degree-of-freedom to further validate our observation regarding the need for a more capable model, beyond those currently available. The results of the simulations and experiments are used to augment the current models, for improved accuracy. The enhanced model includes effect of simultaneous change of stress and temperature.

The next step in our research will include studying control techniques that lend themselves to closed-loop control of SMAs. To this end, we will look into the application of different control methods to the one-degree-of freedom rotary SMA robotic arm. These control techniques will include PID control, Variable Structure Control, Kalman Filter, Sliding Mode Control, and model-based Backstepping Control.

1.7 Outline

Chapter 1 concludes with the outlines of the intended contributions of this study. Chapter 2 presents the background on shape memory alloys. Different constitutive models are surveyed (Section 2.1) and the phenomenological constitutive models are studied in more detail in Section 2.2 followed by a discussion about other models in Section 2.3. The relative importance of different parts of the phenomenological models is discussed in Section 2.4.

In Chapter 3, an SMA-actuated robotic arm is modeled in order to further investigate the phenomenological constitutive models (Section 3.2). In Section 3.3, the model is verified using the experimental data. Section 3.4 represents the shortcoming of the developed model in simulating the closed-loop behavior of the robotic arm. An SMA wire is also used to actuate a dead-weight in vertical direction. Experimental results of actuation of the dead-weight are presented in Section 3.5. Using these results and the simulation results of the robotic arm, it is shown that better constitutive models are needed in order to describe certain behavior of the SMA wires under complex thermomechanical loads. Section 3.6 presents the enhanced phenomenological model, which is able to predict the behavior of SMA elements under complex thermomechanical loadings. Section 3.7 concludes the chapter by introducing a procedure for modeling shape memory alloy actuators.

Chapter 4 presents a few control designs for the SMA-actuated robotic arm. What makes this system interesting is that the stress of the SMA wire changes due to actuation. This makes the control of this system challenging, since the phase transformation as the basis of the SMA actuation depends on stress (Section 4.2). Several control algorithms are presented for position control of this system in sections 4.3-4.7.

Finally, Chapter 5 summarize the main steps of this research.

Chapter 2

Background

Shape memory alloys are a group of metal alloys that exhibit the characteristics of either large recoverable strains or large force due to temperature and/or load changes. The unique thermomechanical property of the SMAs is due to the phase transformation from the austenite (parent) phase to martensite (product) phase and vice versa. These transformations take place because of changes in the temperature, stress, or a combination of both. In the stress-free state, an SMA material at high temperature exists in the parent phase. The parent or austenite phase usually is a body centered cubic crystal structure. When the temperature of the material decreases, as shown in Fig. 2.1, the phase transforms into martensite which is usually a face centered cubic structure. In the stress-free state the martensite phase exists in multiple variants that are crystallographically similar but are oriented in different habit planes [8].

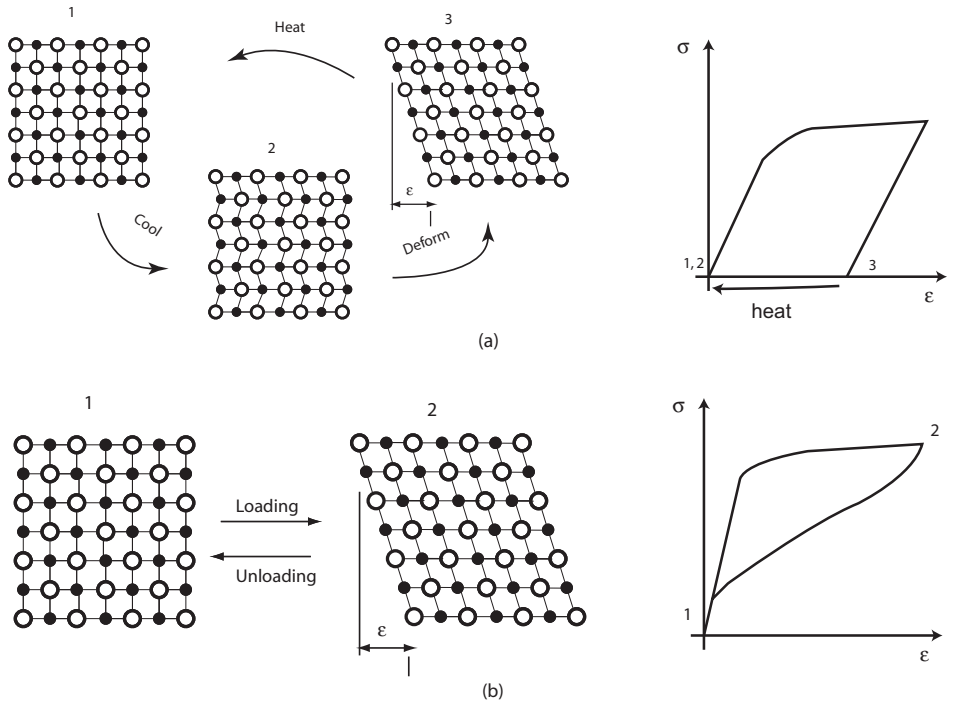

Figure 2.1: (a) The process of shape memory effect; (b) The process of pseudoelasticity

The observable macroscopic mechanical behavior of SMAs can be separated into two categories: the shape memory effect, as shown in Fig. 2.1a and pseudoelastic (superelastic) effect, as shown in Fig. 2.1b. In the shape memory effect, an SMA material exhibits a large residual strain after the loading and unloading. This strain can be fully recovered upon heating the material. In pseudoelastic effect the SMA material achieves a very large stain upon loading that is fully recovered in a hysteresis loop upon unloading [8].

When the stress-free austenite phase cools down below the martensite start temperature (M_s), the phase starts transforming to martensite. The material will be completely martensitic when the temperature drops below the martensite finish temperature (M_f). In this phase, the material has multiple variants and twins. No phase transformation to austenite

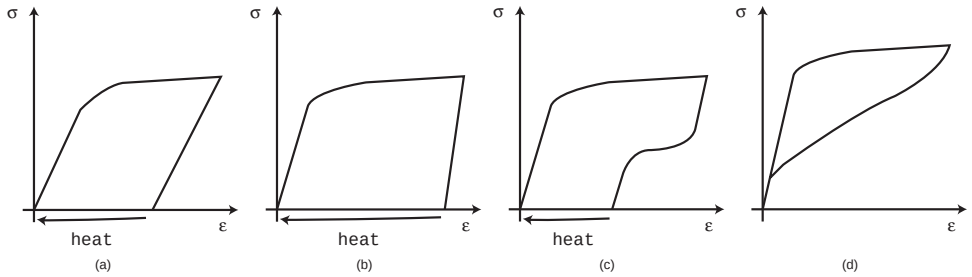

Figure 2.2: Mechanical behavior of the shape memory alloy. The nonlinear portion of the plot is due to detwinning the martensite variants or transforming the austenite to martensite. (a) $T < A_s$ at the beginning material is fully martensitic (b) $M_s < T < A_s$ at the beginning material is fully austenitic (c) $A_s < T < A_f$ at the beginning material is fully austenitic (d) $T > A_f$ at the beginning material is fully austenitic

takes place as long as the temperature of the material is below the austenite start temperature (A_s). When, however, the material is loaded, it will initially start deforming elastically. If the stress increases above a certain amount, the pairs of martensite twins begin detwinning to the stress-preferred twins. During this reorientation process, stress rises very slightly. This single variant of the martensite is thermodynamically stable at $T < A_s$. Therefore, upon unloading there is no conversion to the multiple variant martensite and only a small elastic negative strain will take place. This will leave the detwinned material with a residual strain. The detwinned material, as shown in Fig. 2.1, can recover the residual strain by heating above the austenite final temperature (A_f). The transformation to austenite, and thus creating the shape memory effect which is also illustrated in Fig. 2.2a, starts at the austenite start temperature ($A_s < A_f$).

If the temperature is above the martensite start, the material will be in the austenite phase. When the applied stress to this material exceeds a certain amount the austenite transforms to martensite leading to a seemingly plastic strain. Because of the presence of the stress,

upon completion, the material ideally consists of only a single variant of the martensite. If $T > A_f$ upon unloading the material goes through a reverse transformation to the parent phase, thus recovering the strain. The reason for the reverse transformation is that the martensite is not stable at this temperature. The recovery of the strain in the hysteresis loop which is illustrated in Fig. 2.2d is called pseudoelasticity.

If $A_s < T < A_f$, the result upon unloading is a partial pseudoelastic strain recovery. The remaining residual strain, as shown in Fig. 2.2c, can be recovered by heating the material above A_f. If the material is initially austenite but $T < A_s$, upon unloading no pseudoelastic effect takes place the result is a different case of shape memory effect [8]. This is shown in Fig. 2.2b.

From the thermodynamics perspective and based on the Clausius-Clapeyron equation:

$$\frac{dT}{d\sigma} = \frac{T\Delta V}{\Delta H} \tag{2.1}$$

it can be shown that the phase transformation temperature is a linear function of applied stress [9]:

$$\frac{dT}{d\sigma} = \text{constant}, \tag{2.2}$$

where σ is the applied stress to the SMA material, ΔV and ΔH are changes in the volume and the enthalpy that take place due to the phase transformation. Equation 2.2 shows the effect of the stress on the phase transformation. Because the applied stress can shift the transformation temperatures, the phase transformation may simply take place due to the

applied stress.

Since shape memory material behavior depends on stress and temperature and is intimately connected with the crystallographic phase of the material and the thermodynamics underlying the transformation process, formulation of adequate macroscopic constitutive laws is necessarily complex [10]. There has been an extensive body of research on modeling the phase transformation and thermomechanical behavior of SMAs that is mostly devoted to one-dimensional SMA components.

2.1 SMA Model Classification

Brinson et al. have divided these models into four categories [11]:

- models based on thermodynamics and derived from a free energy formulation ([12]-[13]),
- mathematical models for the dynamics of phase boundary motion ([14]-[15]),
- constitutive laws based on micromechanics concepts using energy dissipation guidelines ([16]), and
- phenomenological laws based on uniaxial stress-strain-temperature data ([8], [6]- [7]).

These constitutive models are each aimed at describing a different aspect of shape memory behavior and address the thermomechanical behavior of SMAs due to the phase transforma-

tion process on different scales.

Engineering applications have emphasized phenomenological models, which avoid difficult–to–measure parameters such as free energy and use only clearly defined engineering material constants. The focus of this study will be on the adequacy of the phenomenological models for describing the behavior of the SMA elements under complex thermomechanical loads.

2.2 Phenomenological Models

In 1986, Tanaka [17] presented a unified one-dimensional martensitic phase transformation model. His study was restricted to the stress-induced martensite phase transformation. The basic assumption was that the thermomechanical process of the material is fully described by three state variables: strain, temperature, and martensite fraction. The martensite fraction (ξ), as an internal variable, characterizes the extent of the martensite phase transformation. Choosing the Helmholtz free energy and using the Clausius-Duhem inequality, Tanaka developed the constitutive equation in the rate form, showing that the rate of stress is a function of the strain, temperature, and martensite fraction rates. If the expression for free energy is known, the free energy minimization may determine the equilibrium state and therefore the relation of the martensite fraction with applied stress and temperature. Instead, based on the study of the transformation kinetics, Tanaka assumed an exponential kinetics function.

The kinetics equation describes the phase transformation fraction as an exponential function

of stress and temperature:

$$\begin{aligned} \xi_{M\to A} &= \exp[A_a(T - A_s) + B_a\sigma] \\ \xi_{A\to M} &= 1 - \exp[A_m(T - M_s) + B_m\sigma] \end{aligned} \tag{2.3}$$

where A_a, A_m, B_a, and B_m are material constants in terms of transition temperatures, A_s, A_f, M_s, and M_f. Tanaka qualitatively showed that pseudoelasticity, ferroelasticity (partial pseudoelasticity), and shape memory effect can be described using the combination of the presented constitutive and kinetics models. The thermomechanical loadings that were considered are either isothermal mechanical loading or changing the temperature under stress free condition. An advantage of this model is that the parameters are simply determined by mechanical experiments.

Motivated by the need for a unified and theoretical constitutive model for SMA material, in 1990, Liang and Rogers developed a new phenomenological model based on the Tanaka model [7]. They chose the thermodynamic concept of free energy, Ψ, as a way to determine the balance between the internal energy and the entropy:

$$\Psi = E - TS \tag{2.4}$$

The internal energy, E, seeks its minimum by pulling together all particles into a temperature and stress preferred lattice. While the entropy, S, attempts to maximize the distribution of particles over all available lattice configurations.

Liang and Rogers followed Tanaka in adopting the minimization of the Helmholtz free energy. They showed that a sufficient condition for the Clausius-Duhem inequality to hold is:

$$\overline{\sigma} = \rho_0 \frac{\partial \Psi}{\partial \varepsilon} = \overline{\sigma}(\varepsilon, \xi, T) \tag{2.5}$$

where Ψ is the Helmholtz free energy that is assumed to be a function of state variables and ρ_0 is the density. By assuming that the state variables are stress, strain, and martensite fraction, the constitutive equation can be written as:

$$\dot{\overline{\sigma}} = E\dot{\overline{\varepsilon}} + \Theta\dot{T} + \Omega\dot{\xi} \tag{2.6}$$

where $\overline{\sigma}$, $\overline{\varepsilon}$, T, and ξ are Piola-Kirchhoff stress, Green strain, temperature, and martensite fraction, respectively. The term E is the Young's modules, Θ is the thermoelastic tensor, and Ω is the transformation tensor. These material properties are related to the thermodynamics as follows:

$$E = \rho_0 \frac{\partial \Psi^2}{\partial \varepsilon^2} \qquad \Theta = \rho_0 \frac{\partial \Psi^2}{\partial \varepsilon \partial T} \qquad \Omega = \rho_0 \frac{\partial \Psi^2}{\partial \varepsilon \partial \xi} \tag{2.7}$$

In their model Liang and Rogers adopted Tanaka's constitutive equation. For the phase kinetics, however, they assumed a cosine relationship to describe the martensite fraction as a function of the stress and temperature. Additionally, they assumed that the material properties are constant. The phase transformation kinetics equation for the heating is:

$$\xi = \frac{\xi_M}{2} \cos[a_A(T - A_s) + b_A\sigma] + \frac{\xi_M}{2} \tag{2.8}$$

The phase transformation equation for the cooling is:

$$\xi = \frac{1-\xi_A}{2}\cos[a_M(T-M_f)+b_M\sigma]+\frac{1+\xi_A}{2} \tag{2.9}$$

where $a_A = \frac{\pi}{A_f-A_s}$, $a_M = \frac{\pi}{M_s-M_f}$ are two material constants, A_f, A_s, M_f, and M_s are austenite final, austenite start, martensite final and martensite start temperatures, respectively. The two other material constants are defined as $b_A = -\frac{a_A}{C_A}$ and $b_M = -\frac{a_M}{C_M}$. C_A and C_M indicate the influence of stress on these four transformation temperatures. Furthermore, ξ_M and ξ_A are the martensite fraction reached before heating and cooling, respectively.

The argument for the cosine functions should be between 0 and π which means that the transformation takes place only if the temperature is in the transformation range:

$$A_s \leq T \leq A_f \quad \text{or} \quad M_f \leq T \leq M_s$$

Equivalently, the stress range for the martensite to austenite phase transformation is defined as:

$$C_A(T-A_s)-\frac{\pi}{|b_A|} \leq \sigma \leq C_A(T-A_s) \tag{2.10}$$

and the corresponding stress range for the austenite to martensite transformation is defined as:

$$C_M(T-M_f)-\frac{\pi}{|b_M|} \leq \sigma \leq C_M(T-M_f) \tag{2.11}$$

The combination of the constitutive and kinetics equations can model the isothermal stress

induced martensite phase transformation as well as elastic deformation of the alloy both for martensite and austenite phases. Maximum recoverable strain is achieved when the material is fully transformed to martensite by applying stress. During the loading phase, the martensite fraction is defined as the ratio of strain to the maximum recoverable strain that can be achieved when the alloy is fully martensitic:

$$\xi = \frac{\overline{\varepsilon}}{\overline{\varepsilon}_{\max}} \tag{2.12}$$

It also can be shown that the maximum recoverable strain is:

$$\overline{\varepsilon}_{\max} = -\frac{\Omega}{D} \tag{2.13}$$

Liang and Rogers simulated the shape memory effect in three different forms of free, restrained, and controlled recovery.

In 1993, Brinson [8] developed a one-dimensional model for SMAs based on the previous works of Tanaka and Liang. The same constitutive equation that was initially introduced by Tanaka was adopted considering the same thermodynamics principles. For the phase transformation kinetics, however, Brinson used Liang's model rewritten as:

$$\xi = \frac{\xi_0}{2}\cos[a_A(T - A_s - \frac{\sigma}{C_A})] + \frac{\xi_0}{2} \tag{2.14}$$

for $C_A(T - A_f) < \sigma < C_A(T - A_s)$, and

$$\xi = \frac{1 - \xi_0}{2} \cos[a_M(T - M_f - \frac{\sigma}{C_M})] + \frac{1 + \xi_0}{2} \tag{2.15}$$

for $C_M(T - M_s) < \sigma < C_M(T - M_f)$. Although it is not stated by Brinson, one can assume that Equation 2.14 is for heating (martensite to austenite transformation) and Equation 2.15 is for cooling (austenite to martensite transformation). C_A and C_M are defined as material properties defining the relationship between temperature and the critical stresses that induce the transformation.

The Brinson model does not have one of the shortcomings of Liang model. The Liang model cannot describe the shape memory effect, which takes place because of detwinning of the martensite, at temperatures below M_f. Brinson separated the martensite fraction into two fractions as the fraction induced by stress and the fraction induced by temperature:

$$\xi = \xi_s + \xi_T \tag{2.16}$$

The constitutive equation was also modified accordingly:

$$\dot{\sigma} = D\dot{\varepsilon} + \Theta\dot{T} + \Omega\dot{\xi}_s \tag{2.17}$$

The phase transformation equations are similar to the ones presented by Liang written in terms of critical stresses. Therefore, the Brinson model is capable of showing shape memory

effect at lower temperature which takes place as the result of detwinning, not as the result of the austenite to martensite phase transformation. Furthermore, in the Brinson model the elastic modulus and the transformation tensor were assumed to be functions of the martensite fraction.

When the SMA element is used for actuation, normally there is a bias element to restore the initial geometry of the SMA actuator after each actuation cycle. In these cases, due to the stress applied by the bias force, the phase transformation from austenite to martensite results in a single stress-preferred martensite and not the twinned martensite variants. Therefore, the Brinson model essentially reduces to the Liang model for SMA actuators with restoring bias elements.

2.3 Other SMA Models

Boyd and Lagoudas [18] used a micromechanical method to predict the thermomechanical response of composites consisting of SMA fibers reinforcing non-SMA matrix materials. The three-dimensional SMA constitutive model that they presented is based on the model presented by Tanaka. Furthermore, they only considered martensite fraction that is induced by the stress. For the transformation kinetics, the exponential form similar to the one used by Tanaka was adopted.

In developing their one-dimensional phenomenological constitutive model, Ivshin and Pence [19], considered only the single-variants martensite. In other words they ignored the twinning-

detwinning processes. Their assumption is based on the fact that stress biases the phase toward a single stress-preferred variant of martensite. They introduced an internal variable, the austenite fraction α, and used it as a state variable. Other state variables were then calculated based on the austenite phase fraction. For example, the strain of the alloy was presented as:

$$\varepsilon = (1 - \alpha)\varepsilon_M + \alpha\varepsilon_A \tag{2.18}$$

where ε_M and ε_A are the strain of the martensite and austenite phases, respectively. The phase transformation kinetics, which is based on a hysteresis model presented by Ivshin and Pence, has two main parts for modeling the effect of stress and temperature. The first part models the effect of temperature on the phase transformation. The second part includes the effect of stress on the phase kinetics. Simulating different loading conditions such as isothermal, adiabatic, and isostress, they showed that the model is capable of capturing the essential behavior of a one-dimensional SMA element.

Another one-dimensional model for SMAs was developed by Barrett [20] that is very similar to the last three models. The main difference is that the model covers both tension and compression. The constitutive equation is similar to the one used by Tanaka, Liang, and Brinson. The difference is that in this model the effect of the phase transformation is indirectly accounted for. The transformation kinetics is modeled as a linear function of temperature. The effect of the stress on the phase transformation is included in the phase transformation limit temperatures. The reported simulation results are similar to the results of the Liang model.

The other one-dimensional SMA model that follows the same principals of Tanaka, Liang, and Brinson models was developed by van der Wijst [21]. Wijist used the martensite fraction along with a newly introduced variable. Using these two variables the stress-strain hysteresis loop can be mapped into a rectangle. Therefore, both stress and strain are given as a bilinear function of these two variables:

$$\varepsilon = e_1 + e_2\xi + e_3 m + e_4 \xi m \tag{2.19}$$

$$\sigma = p_1 + p_2\xi + p_3 m + p_4 \xi m \tag{2.20}$$

where m and ξ are the two variables, and e_i and p_i are constants that are linear functions of temperature. Wijst used this model to analyze the behavior of the SMA actuators under static mechanical behavior. The reported results are similar to that of Tanaka, Liang, and Brinson.

In their study, Prahlad and Chopra [22] experimentally dealt with the complex thermo-mechanical loadings of SMAs. For simulations, they adopted the Brinson model. They performed isothermal tensile tests for which initially the SMA material was either twinned martensite or austenite depending on the initial temperature. In those tests they observed both shape memory effect and pseudoelasticity. They also performed tensile and dead-weight tests at different temperatures. They performed the stress-temperature test on a fully restrained SMA wire.

Based on these experiments, Prahlad and Chopra plotted the stress-transformation temper-

ature behavior of the SMA material and showed its agreement with previous researchers' results. They also showed effect of loading rate. In isothermal tests, for higher rates of strain the stress reaches higher values, which is followed by a stress relaxation. They attributed this and also the relaxation behavior of SMAs to the fact that at slower rates the material has time to adjust its internal structure. They also showed that the critical stress and temperatures change with faster strain rates.

Chopra, in a review paper on state of the art of smart materials and their research challenges, showed one major research front. In order to make SMA's more applicable and controllable is to investigate their dynamic behavior, i.e., looking at the behavior of SMA's at higher loading rates [23]. In this work, Chopra reviewed models of shape memory alloys and classified them. He argues that most of the constitutive models are developed based on quasistatic loading. In reaching this conclusion he reviewed models by Liang, Brinson and Lagoudas.

2.4 Summary

Most of the SMA constitutive models, as stated by Brinson and Huang [10], are made of two main parts; the mechanical law governing the stress-strain behavior and the transformation kinetics that models the martensite phase transformation. As they have shown, for phenomenological SMA models, which are the most practical models, the critical aspect is the phase transformation kinetics law. Therefore, the phase kinetics part of the models defines the behavior of the model. This is true even if a phase kinetic model is used in conjunction

with a different constitutive equation that belongs to a separate model [10].

The main SMA phenomenological models are developed by Tanaka [17], Liang and Rogers [7], Brinson [8]. Some other SMA models are developed by Pence and Ivshin [19] and by Boyd and Lagoudas [18]. By comparing and simplifying these models Brinson and Huang showed that, for the two-part one dimensional models, the kinetics law is more important than the constitutive model. Even the simplest constitutive model if paired with the appropriate kinetics model can satisfactorily predict the behavior of the SMA material.

Chapter 3

The Enhanced Phenomenological Model

In this chapter, we will further investigate the SMA phenomenological models. As presented in Chapter 2, these models belong to a group of models that initially were developed by Tanaka, and were later improved by both Liang and Brinson, respectively. In order to investigate these models, an SMA-actuated robotic arm is studied. This chapter starts with the description of the SMA robotic arm in Section 3.1. Using the existing phenomenological models, the system is modeled in Section 3.2. In Section 3.3, the derived model is simulated and the simulation results are compared with experimental data. Section 3.4 presents the shortcomings of the SMA models in predicting the complete behavior of the SMA-actuated arm. These shortcomings are shown using the simulation results of the system. Using a dead-weight system that is actuated by an SMA wire, the model shortcomings are experimentally

studied, in Section 3.5. An enhanced model is developed to address the shortcomings of the existing SMA phenomenological models. This model is presented in Section 3.6. Finally, Section 3.7 is devoted to presenting a general procedure for modeling systems that are actuated by shape memory alloys.

3.1 SMA-actuated Robotic Arm

The one-degree-of-freedom shape memory alloy (SMA) actuated arm is shown in Fig. 3.1. The shape memory effect (SME) is not reversible; the SMA wire must be deformed by a bias force in martensite to repeat the movement. There are two ways of providing the bias force and therefore two types of SMA actuators. One actuator called *bias type* is composed of an SMA element and a bias spring. The other called *differential type* is made of two SMA elements. In our design the robotic arm is actuated with a bias-type SMA wire actuator where the bias force (torque) is provided by the linear spring and the weight of the moving arm. Therefore, the generating torque is the difference between the bias torque and SMA wire torque.

When the SMA wire is heated beyond the activation temperature it contracts due to the phase transformation from martensite to austenite. The temperature is raised using the resistive electrical (Joule) heating. Upon cooling the wire's temperature drops, causing the austenite to martensite phase transformation. As a result the SMA wire is elongated under the effect of the bias torque. While elongating the twinned martensite changes to the stress-

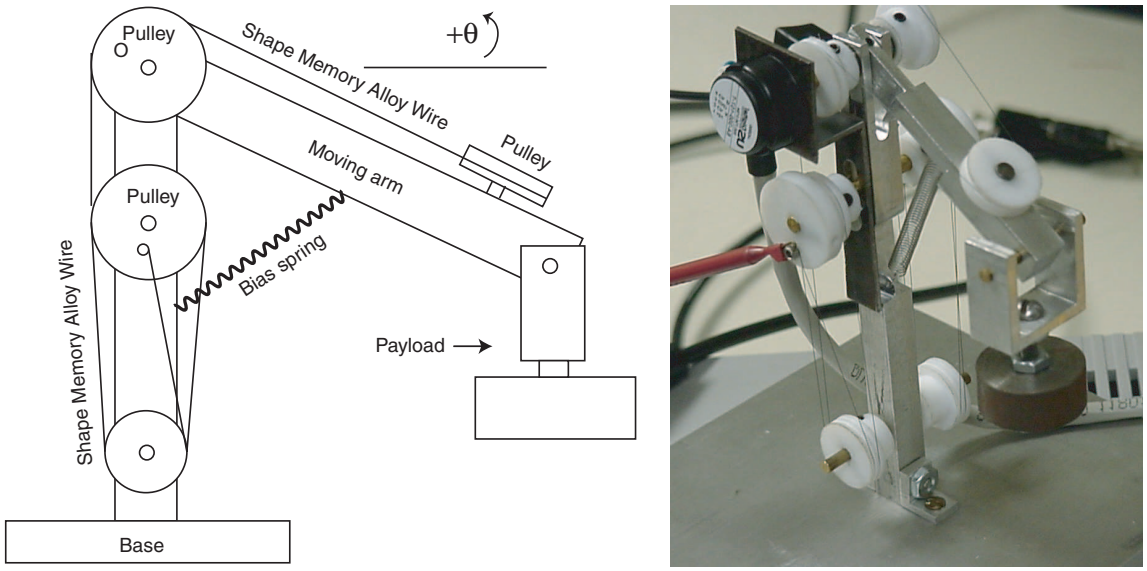

Figure 3.1: The one degree of freedom arm, actuated by SMA NiTi wire, with a bias spring preferred martensite. The initial length of the SMA wire, that is guided by the pulleys, is chosen in a way that upon full contraction it can rotate the arm from its initial position at -45^o to the top position at $+90^o$.

3.2 SMA-actuated Robotic Arm Model

An accurate model of the SMA actuated 1-DOF arm is required for simulation and evaluation of different control algorithms. The model is constructed from several related parts (blocks), each representing an element of the physical system's behavior. The model for the SMA-actuated arm consists of phase transformation kinetics, heat transfer, SMA wire constitutive, and arm dynamic model blocks. In addition, there is an amplifier, an encoder, and a signal conditioning model. The input is voltage (to the SMA wire applied through an amplifier) and

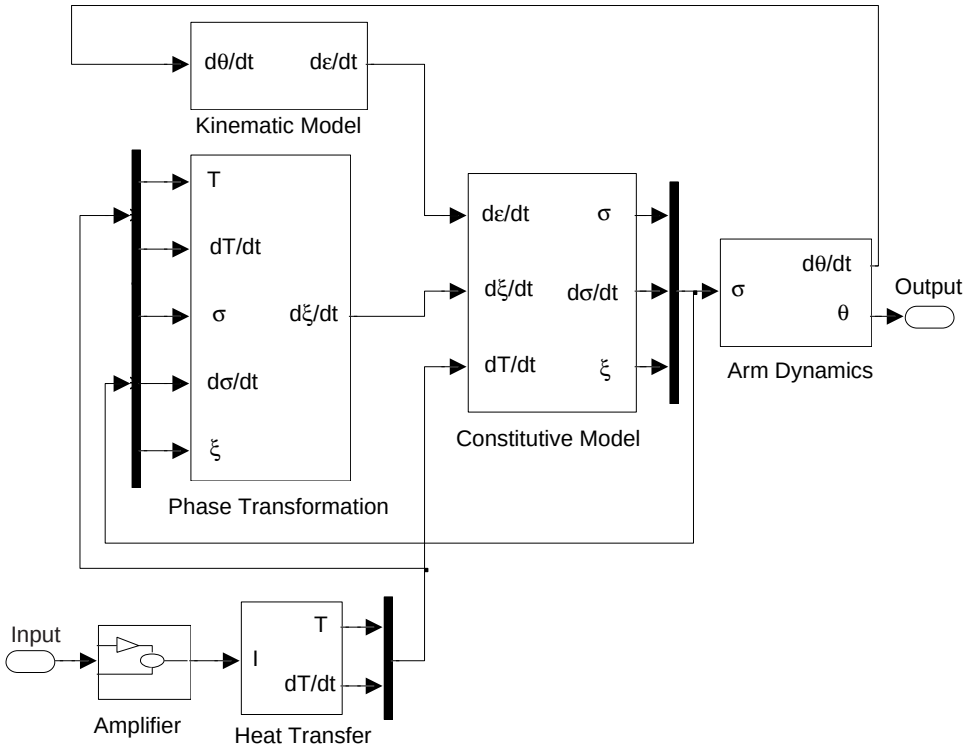

Figure 3.2: Block diagram model of the SMA-actuated robotic arm

the outputs are the arm angular position, arm angular velocity, the SMA wire's temperature, stress, and the martensite fraction. Elements of the models are bilaterally connected forming an algebraic loop. One reason for this interdependency is that physical properties of the SMA wire are dependent on stress and temperature of the wire. Thus, as shown in Figure 3.2, bilateral causality exists between dynamic model and constitutive equation and also wire constitutive equation and martensite fraction (phase transformation) equation.

3.2.1 Heat Transfer Model

SMA wire heat transfer equation consists of electrical (Joule) heating and natural convection:

$$mc_p\frac{dT}{dt} = I^2R - h_cA_c(T - T_\infty) \tag{3.1}$$

The SMA wire that is used in the system is Ni-Ti alloy. Its diameter is 150 micron and the parameters in heat transfer equation are: $m = (\rho\pi\frac{d^2}{4})$ is mass per unit length of wire, ρ is density of wire, d is diameter of wire, $A_c = (\pi d)$ is circumferential area of the unit length of wire, c_p is specific heat, I is electrical current, R is resistance per unit length of wire, T is temperature of wire, T_∞ is the ambient temperature, and h_c is heat convection coefficient. Although, here we assumed the h_c and R are both constant, detailed analysis on heat transfer as well as resistance analysis of the SMA wire can be found in Appendices A and B, respectively.

3.2.2 Wire Constitutive Model

Wire constitutive model shows the relationship between stress, strain and temperature. We used the phenomenological model presented by Tanaka [17] and later completed by Liang [7] and Brinson [8]. The basic equation is:

$$\dot{\sigma} = E\dot{\varepsilon} + \theta_T\dot{T} + \Omega\dot{\xi} \tag{3.2}$$

where E is the Young modulus, θ_T is the thermal expansion factor, $\Omega = -E\overline{\varepsilon_L}$ is the phase transformation contribution factor, and $\overline{\varepsilon_L}$ is the maximum recoverable strain.

3.2.3 Phase Transformation Model

For simulating the constitutive equation value of the martensite fraction derivative needs to be known at each instant of time. Based on the hysteresis behavior of SMA wires, a cosine phase kinetics model is developed by Liang[9]. The phase kinetics model needs temperature and stress to calculate the fraction. Due to hysteresis behavior of SMA wires the equations for heating and cooling are different.

Reverse Transformation

Reverse transformation equation describing the phase transformation from martensite to austenite (heating) is:

$$\xi = \frac{\xi_M}{2}\{\cos[a_A(T - A_s) + b_A\sigma] + 1\} \tag{3.3}$$

where ξ is martensite fraction which has a value between 1 (martensite phase) and 0 (austenite phase). ξ_M is the minimum martensite fraction the wire reached during the cooling. $a_A = \frac{\pi}{A_f - A_s}({}^oC^{-1})$ is a curve fitting parameter, T is wire's temperature, σ is wire's stress, A_s is austenite phase start temperature, A_f is austenite phase final temperature, $b_A = \frac{-a_A}{C_A}$ and C_A are curve fitting parameters.

Therefore, the derivative equation for heating can be written as:

$$\dot{\xi} = \frac{-\xi_M}{2} \sin[a_A(T - A_s) + b_A\sigma][a_A\dot{T} + b_A\dot{\sigma}] \tag{3.4}$$

If $A'_s = (A_s + \frac{\sigma}{C_A}) < T < (A_f + \frac{\sigma}{C_A}) = A'_f$.

Otherwise $\dot{\xi} = 0$. Where A'_s and A'_f are the *stress modified* austenite start and final temperatures, respectively.

Forward Transformation

Forward transformation equation describing the phase transformation from austenite to martensite (cooling) is:

$$\xi = \frac{1 - \xi_A}{2} \cos[a_M(T - M_f) + b_M\sigma] + \frac{1 + \xi_A}{2} \tag{3.5}$$

where ξ_A here is the minimum martensite fraction obtained during heating, $a_M = \frac{\pi}{M_s - M_f}$ is a curve fitting parameter, M_s is martensite phase start temperature, M_f is martensite phase final temperature, and $b_M = \frac{-a_M}{C_M}$ is a curve fitting parameter.

Therefore, the derivative equation for cooling can be written as:

$$\dot{\xi} = \frac{1 - \xi_A}{2} \{-\sin[a_M(T - M_f) + b_M\sigma]\}[a_M\dot{T} + b_M\dot{\sigma}] \tag{3.6}$$

If $M'_f = (M_f + \frac{\sigma}{C_M}) < T < (M_s + \frac{\sigma}{C_M}) = M'_s$

Otherwise $\dot{\xi} = 0$. Where M_s' and M_f' are the *stress modified* martensite start and final temperatures, respectively.

3.2.4 Kinematic Model

Kinematic model describes the relationship between strain ε and angular displacement θ. Measuring positive angle clockwise, the equation is:

$$\dot{\varepsilon} = -\frac{2r\dot{\theta}}{l_0} \tag{3.7}$$

where r is pulleys radius and l_0 is wire initial length.

3.2.5 Dynamic Model

The nonlinear dynamic model of the arm including spring and payload effects is:

$$I_{\mathrm{e}}\ddot{\theta} + \tau_{\mathrm{g}} + \tau_{\mathrm{s}} + c\dot{\theta} = \tau_{\mathrm{w}} \tag{3.8}$$

Where $\tau_{\mathrm{w}}, \tau_{\mathrm{g}}$, and τ_{s} are the resulting torques from SMA wire, gravitational loads, and spring, respectively. I_{e} is the effective mass moment of inertia of the arm, and the payload, and c is the torsional damping coefficient.

3.3 Model Simulation and Verification

Computer simulations of the SMA arm model are performed in MATLAB/Simulink® environment; dSPACE® *hardware-in-the-loop* solution is used for the experiments. The material properties of the shape memory alloy are primarily taken from Liang [9] and Waram [24], Table 3.1 shows these and other modeling parameters. Experimental evaluations, by Elahinia and Ashrafiuon [25], have demonstrated reasonable accuracy of the actuator model, as shown in Figure 3.3. The figure compares simulation and experimental results at 7.0 and 7.2 volts. Some of the differences between the simulation and experimental results are due to parameter uncertainties and model simplifications. Specifically, the modulus, transformational tensor, and thermal coefficient were all assumed to be constant. The assumptions of a linear spring force and viscous friction contributed to the discrepancy of the results.

The main qualitative aspects of the SMA arm model can be derived from Figures 3.4 and 3.5. In Figure 3.4, a 7.2 V input is applied to the actuator and the temperature of the wire rises. The beginning martensite fraction is equal to 1 and no phase transformation takes place as the temperature increases past the martensite final temperature, M_f. As the wire continues to heat, the temperature exceeds the austenite start temperature, A_s, and the martensite fraction decreases–resulting in contraction of the wire–at a rate defined by the derivative of Equation 3.4. In steady state, the temperature falls somewhere between the austenite start and final temperatures, hence only partial transformation is achieved.

As shown in Figure 3.5, only a slightly larger voltage, 7.3 V, results in a full transformation

Table 3.1: Modeling parameters and their numerical value

Parameter	Description	Unit	Value
m	SMA wire's mass per unit length	Kg	$1.14e^{-4}$
A_c	SMA wire's circumferential area per unit length	m^2	$4.712e^{-4}$
C_p	Specific heat of wire	Kcal/Kg.^{o}C	0.2
R	SMA wire's resistance per unit length	Ω	45
T_∞	Ambient temperature	^{o}C	20
h_c	Heat convection coefficient	J/m^2.^{o}CSec	150
E_A	Austenite Young modulus	GPa	75.0
E_M	Martensite Young modulus	GPa	28.0
θ_T	SMA wire's thermal expansion factor	MPa/^{o}C	0.55
Ω	Phase transformation contribution factor	GPa	-1.12
σ_0	SMA wire's initial stress	MPa	75.0
ε_0	SMA wire's initial strain		0.04
T_0	SMA wire's initial temperature	^{o}C	20
ξ_0	SMA wire's initial martensite faction factor		1.0
A_s	Austenite start temperature	^{o}C	68
A_f	Austenite final temperature	^{o}C	78
M_s	Martensite start temperature	^{o}C	52
M_f	Martensite final temperature	^{o}C	42
C_A	Effect of stress on austenite temperatures	MPa/^{o}C	10.3
C_M	Effect of stress on martensite temperatures	MPa/^{o}C	10.3
l_0	Initial length of SMA wire	mm	900
r	Pulleys diameter	mm	8.25
m_p	Pay load mass	g	57.19
m_a	Moving link mass	g	18.7
k	Bias spring stiffness	N/m	3.871

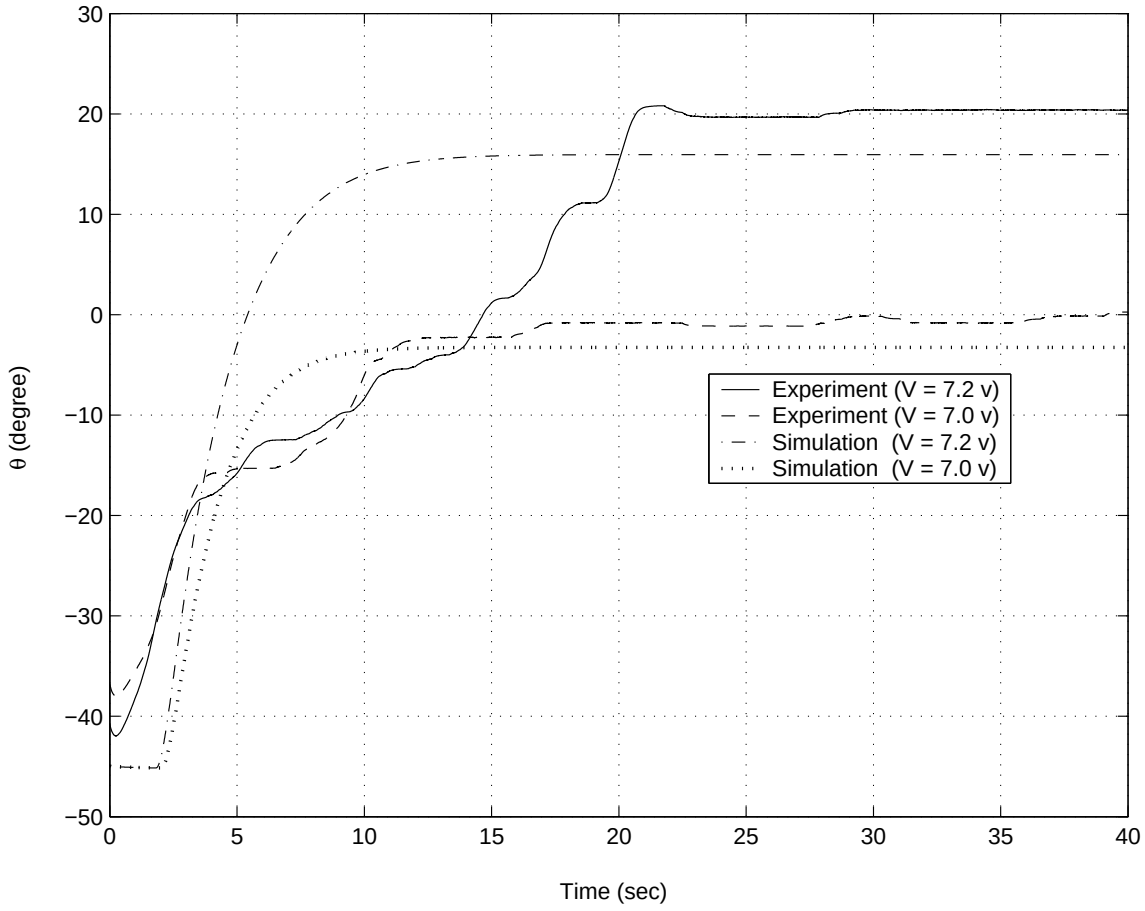

Figure 3.3: Comparison of theoretical model simulations and experimental results

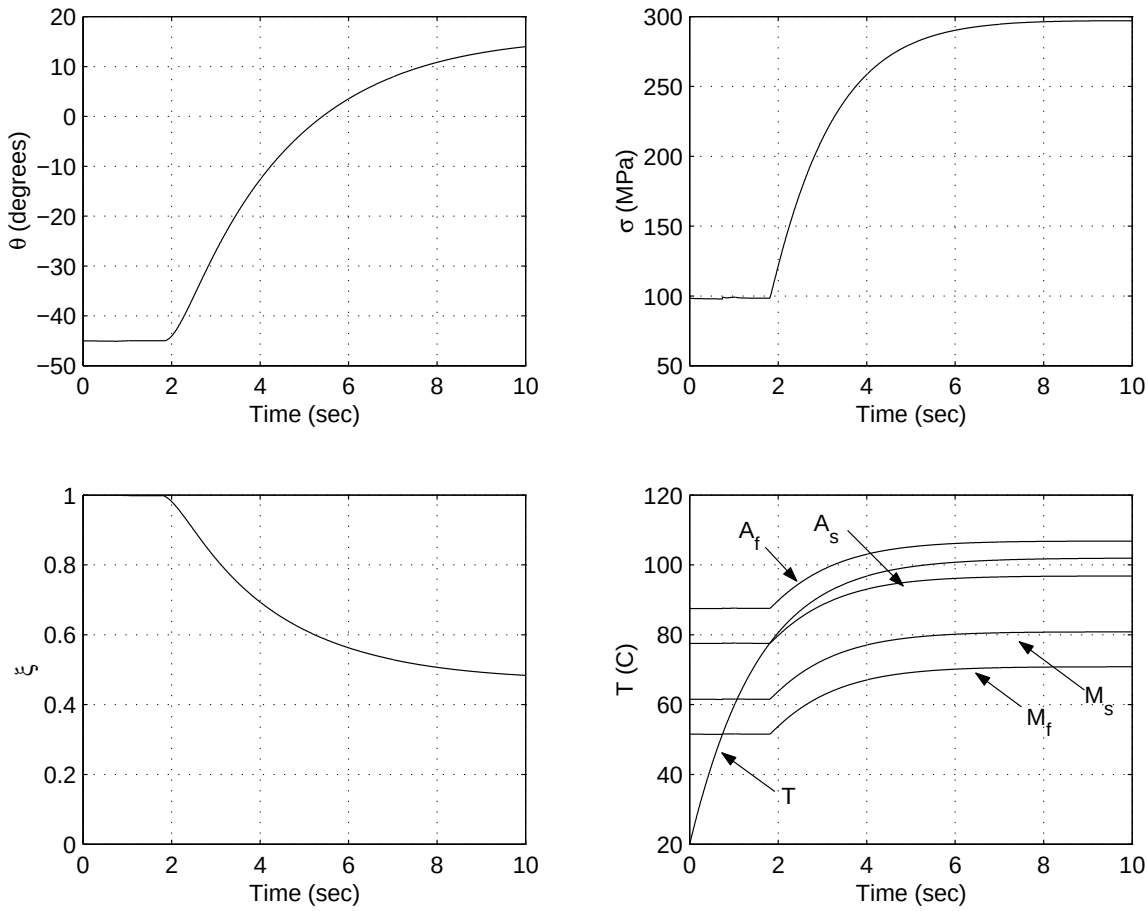

Figure 3.4: SMA model open-loop simulation for a 7.2 V input

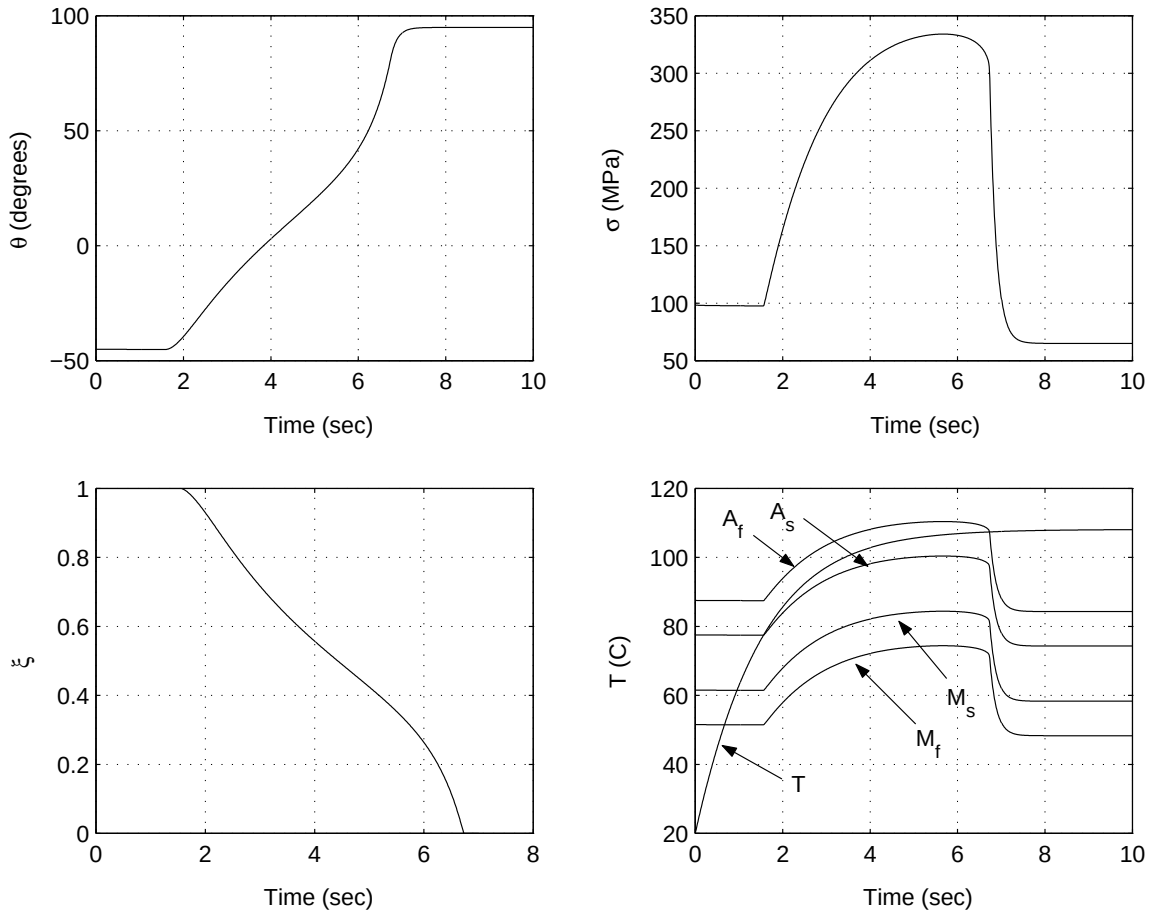

Figure 3.5: SMA model open-loop simulation for a 7.3 V input

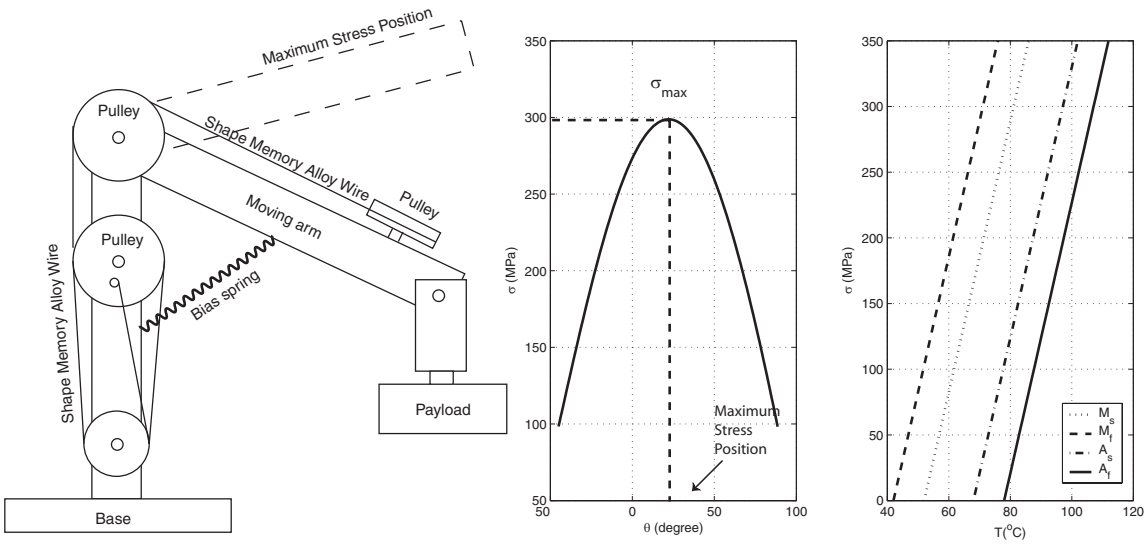

Figure 3.6: When the arm moves beyond the maximum stress position the transformation temperatures decrease

to austenite. The increased voltage heats the wire enough to cause the arm to rotate through the angle of maximum stress. At this angle, shown in Fig. 3.6, the stress of the SMA wire due to gravitational and spring torques is maximum. Upon passing this angle, the stress in the wire begins to decrease rapidly, which results in a drop in the transformation temperatures. This drop allows the temperature of the wire to pass through the austenite final temperature causing the martensite fraction to fall to zero and the wire to achieve maximum strain.

3.4 SMA Phenomenological Models: Where They Fail

While the SMA phenomenological models, presented in Section 3.2, give proper results for most cases, there are certain complex loading cases in which the output of these models does not match experimental results. An example of this shortcoming is presented in this section.

The phase transformation kinetics by Liang [7] and Brinson [8] are adopted in this study. Since in the rotary SMA actuator the wire is always under stress, by the bias spring, these two phenomenological models predict similar behaviors.

Figure 3.7 shows an example of the shortcomings of these models. In this simulation, a sliding mode controller–as presented in Section 4.7–was used to stabilize the rotary SMA actuator. As shown in the figure, the controller was not able to regulate the arm at $\theta_d = 85^o$. As Fig. 3.8 shows the controller, in an attempt to minimize the position error, applied high enough voltage such that the temperature of the wire exceeded the austenite final temperature. Even though the temperature of the wire reached beyond the austenite final temperature, according to the model, the wire did not go through the full phase transformation, as shown in Fig. 3.9. Therefore the arm did not reach the desired angular position. Such a behavior has never been observed in the experiments with the SMA-actuated arm; in other words it has never been observed that the voltage to the SMA wire was increased but the arm did not move accordingly unless the SMA wire was already in the fully austenitic phase. Furthermore, according to the aforementioned phenomenological models if the temperature of the SMA wire exceeds the austenite final temperature the material reaches the fully austenitic phase ($\xi = 0$), which clearly has not happened in this example.

Figure 3.10 illustrates why in this and similar cases the existing phenomenological models cannot predict the behavior of SMA wire: in the simulation, the temperature of the SMA wire exceeded the austenite final temperature while the temperature itself was decreasing. While the SMA wire was cooling down, the stress of the wire decreased which caused the austenite

final temperature to decrease. The rates of decrease of the temperature of the wire and the austenite final temperature are not equal; the SMA wire's temperature decays slower than the austenite final temperature, this way the wire's temperature– while decreasing–exceeded the austenite final temperature. According to the existing phenomenological models, no phase transformation takes place between the austenite start and final temperatures unless the temperature is increasing.

Similar cases exist in which the existing phenomenological models cannot predict the behavior of SMA wires. Three such cases are illustrated in Fig. 3.11. For all the cases shown in the figure, according to these models, the amount of phase transformation that takes place is the same. In all three cases, the stress of the wire decreases by the same amount, which consequently causes the austenite start and final temperatures to drop. This effect is shown in the figure as similar shifts in the hysteresis loop in the $(T-\xi)$ plane. In Fig. 3.11a the wire cools down but with a slower rate and therefore the temperature exceeds the austenite final temperature. The example with the SMA-actuated robotic arm, as illustrated in Fig. 3.10, in which the arm did not reach the desired position, falls in this category. In Fig. 3.11b the wire cools down such that the temperature remains between the austenite start and final. In the third case, as shown in Fig. 3.11c, temperature remains constant and still exceeds the austenite final temperature. For all these three cases with similar stress changes but dramatically different temperature changes the existing phenomenological models predict the same martensite fraction at point 2. In other words no further phase transformation takes place beyond point 1.

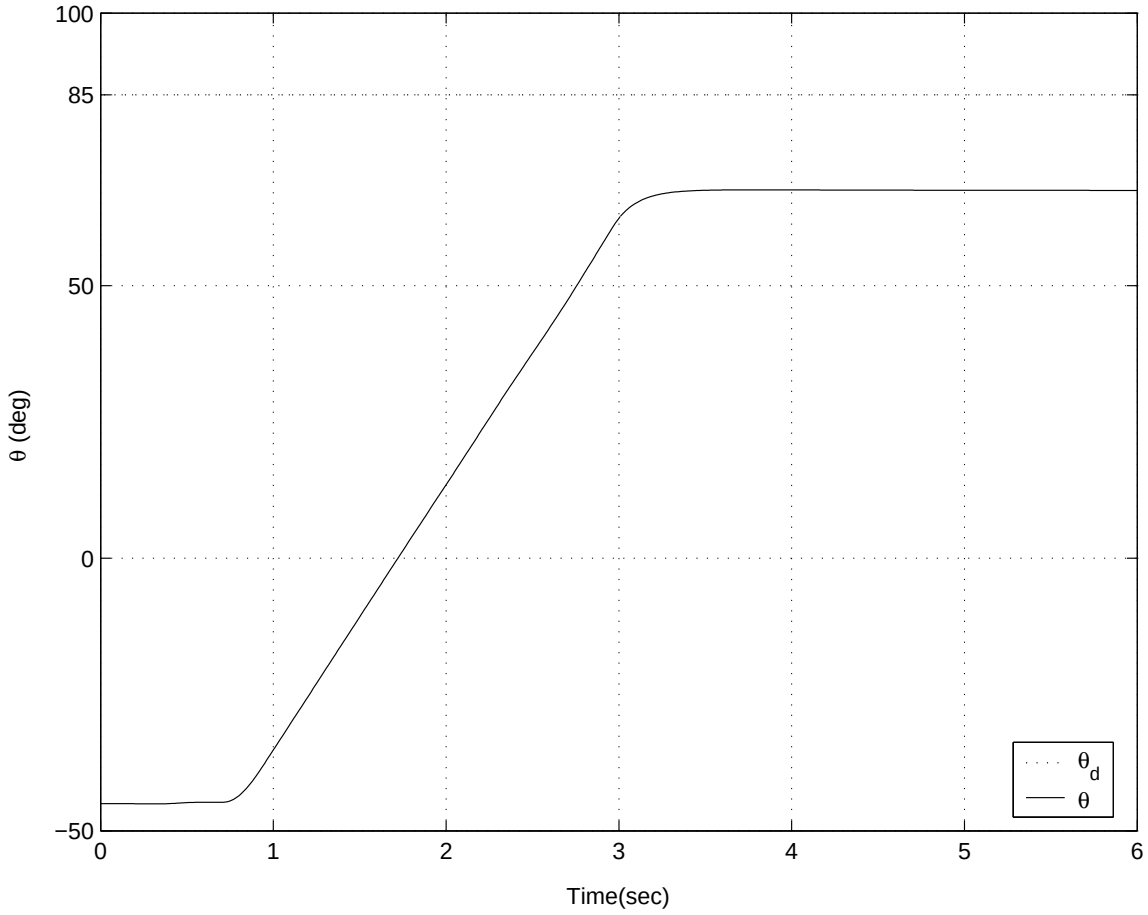

Figure 3.7: Phase transformation model problem: arm does not reach the desired position

Figures 3.12, 3.13, 3.14, and 3.15 depict the same simulation results for a simulation with SMA-actuated robotic arm. In this case the arm was to track a changing step. Since the SMA wire did not undergo any of the complex loading patterns, the existing phase transformation models calculated the martensite fraction properly.

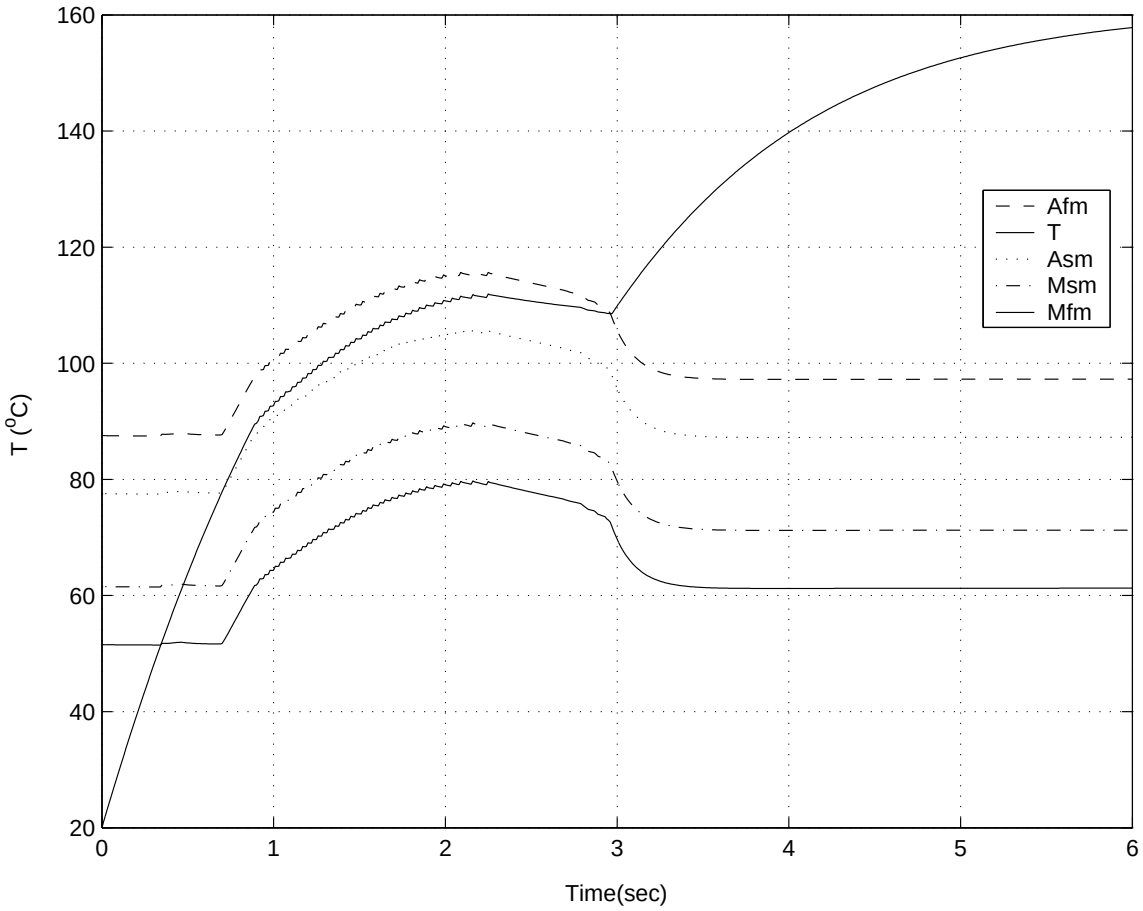

Figure 3.8: Phase transformation model problem: temperature of the SMA wire and transformation temperatures

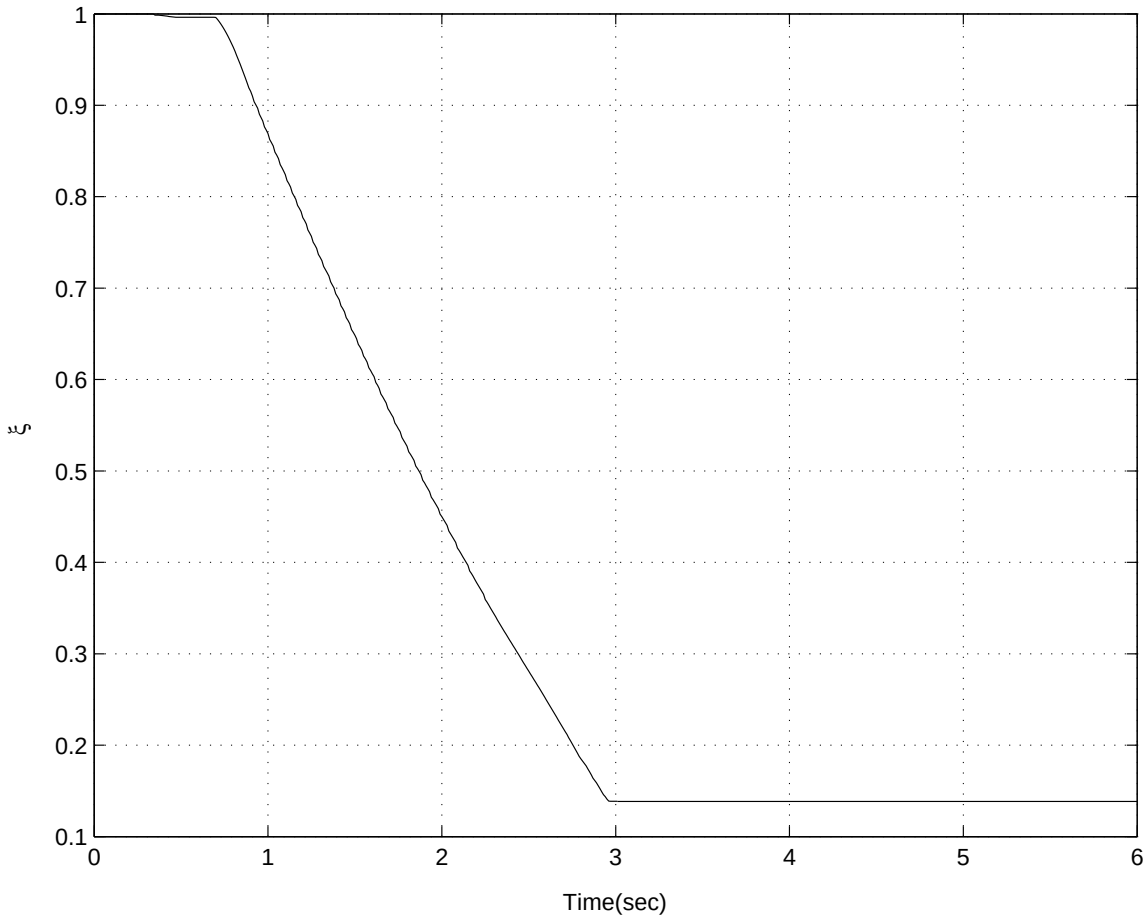

Figure 3.9: Phase transformation model problem: martensite fraction

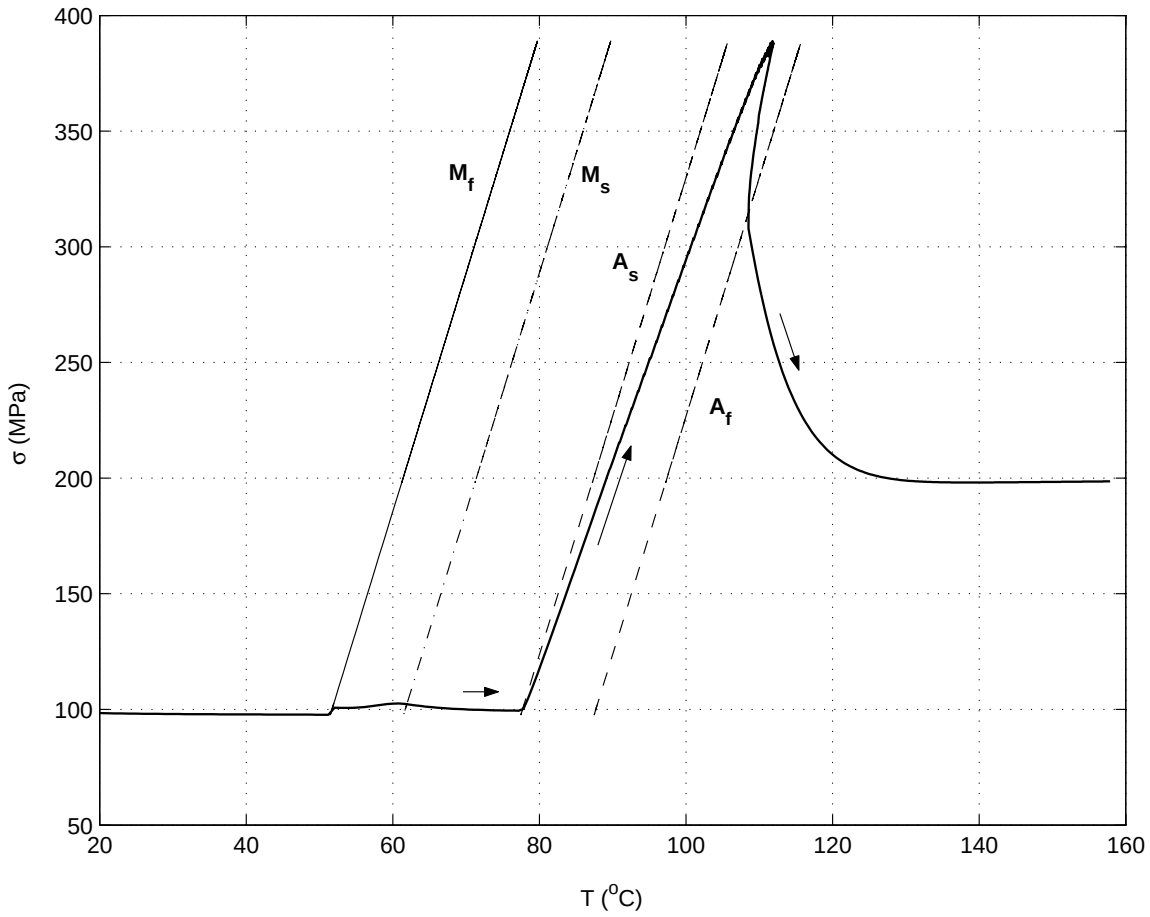

Figure 3.10: Phase transformation model problem: stress vs. temperature

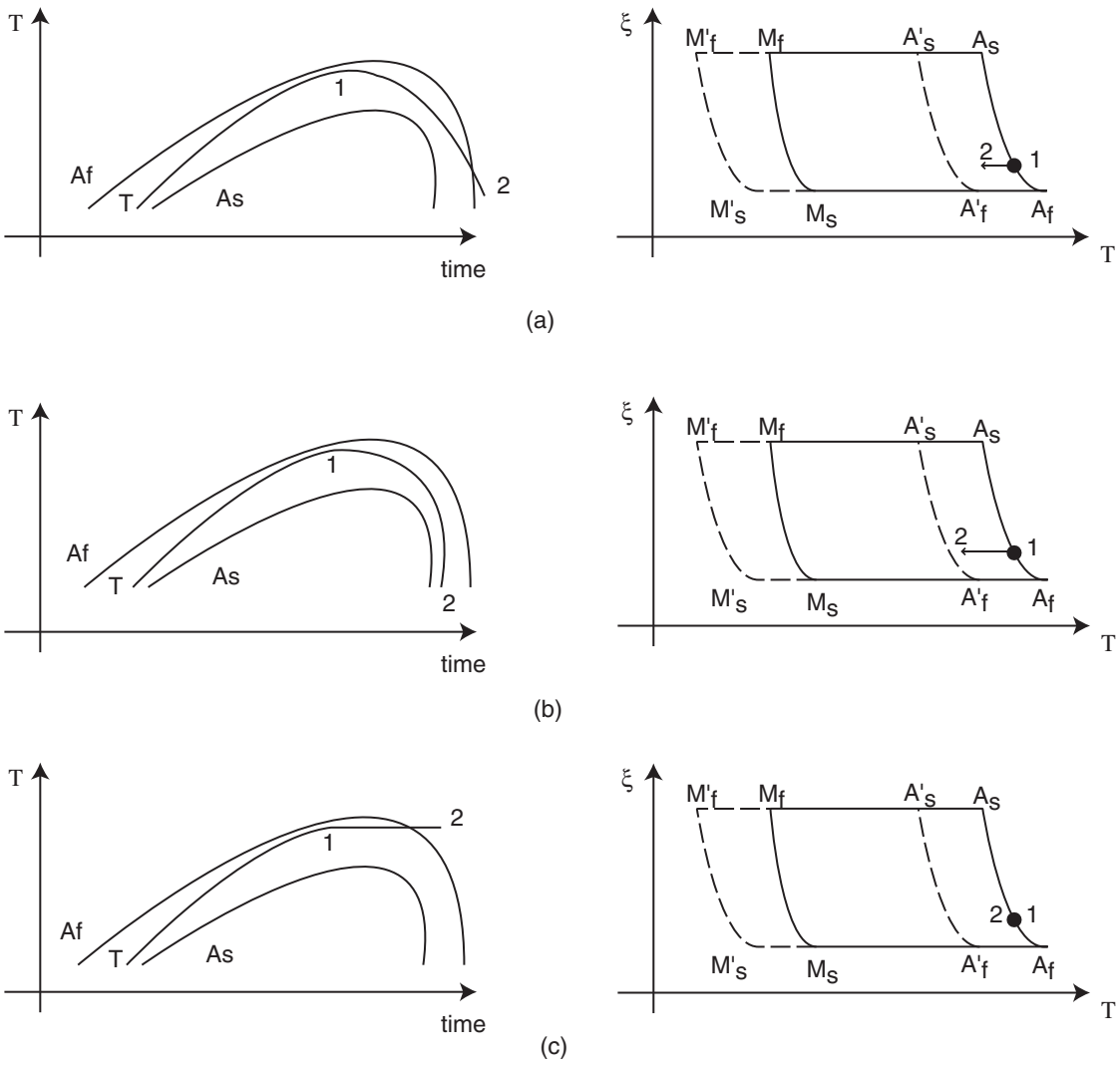

Figure 3.11: The shortcomings of the phase transformation model in predicting the martensite fraction for complex force and heat loading, (a) exceeding the austenite final temperature while cooling (b) remaining in the phase transformation range while cooling (c) exceeding austenite final temperature with constant temperature

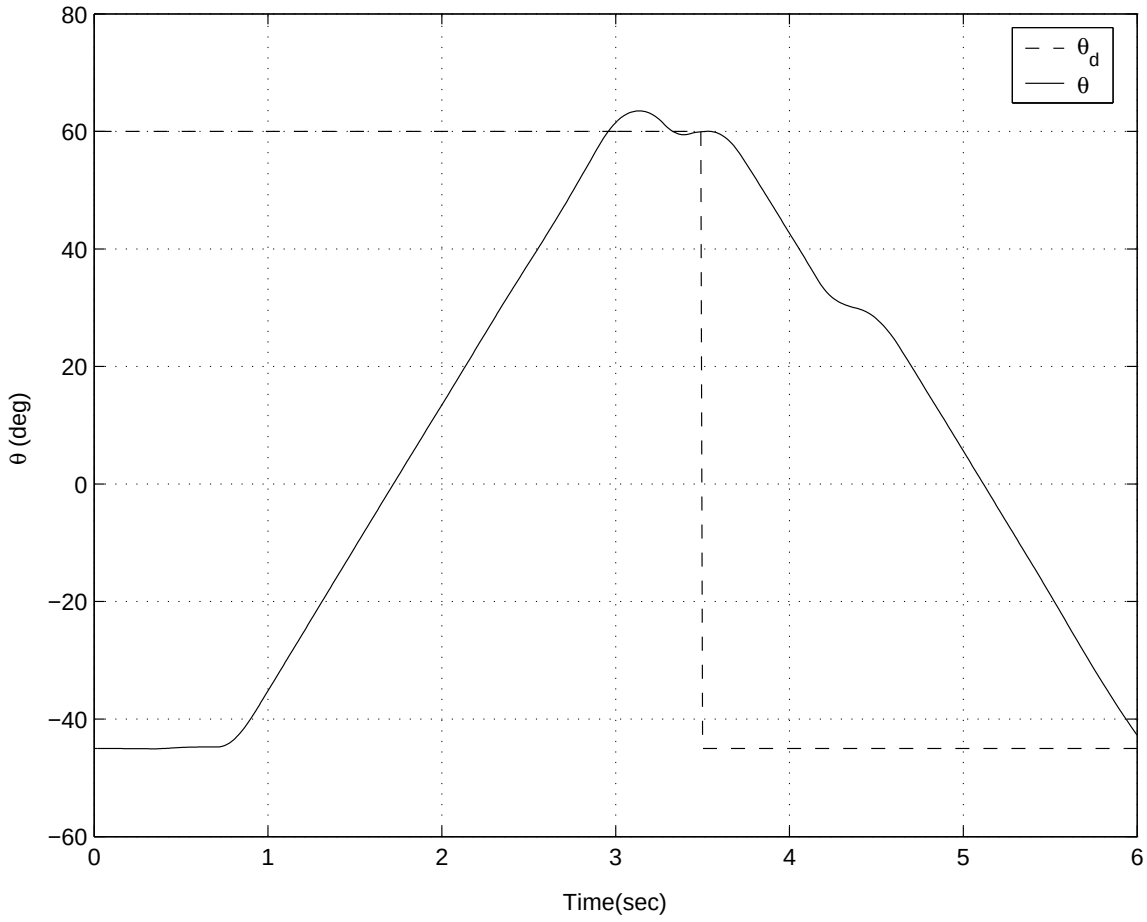

Figure 3.12: Phase transformation model works properly: arm follows the desired position

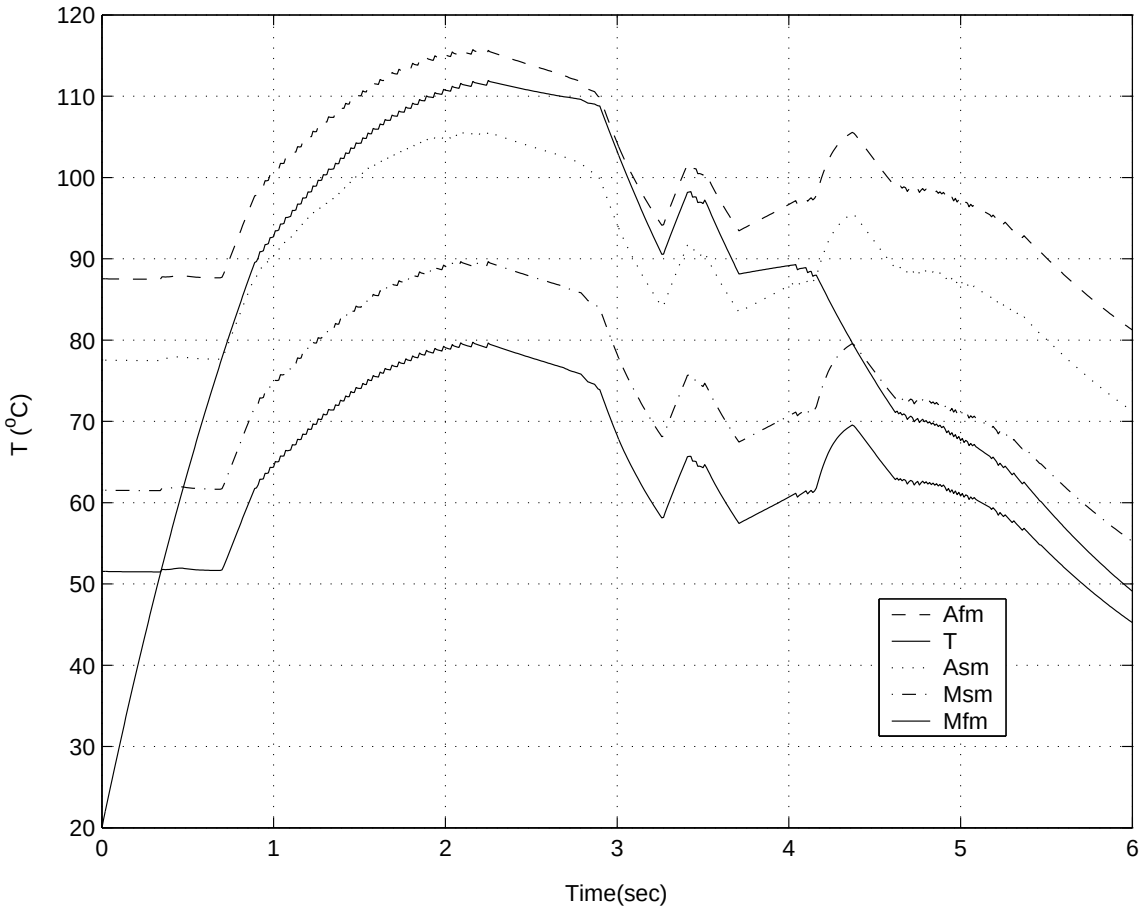

Figure 3.13: Phase transformation model works properly: temperature of the SMA wire and transformation temperatures

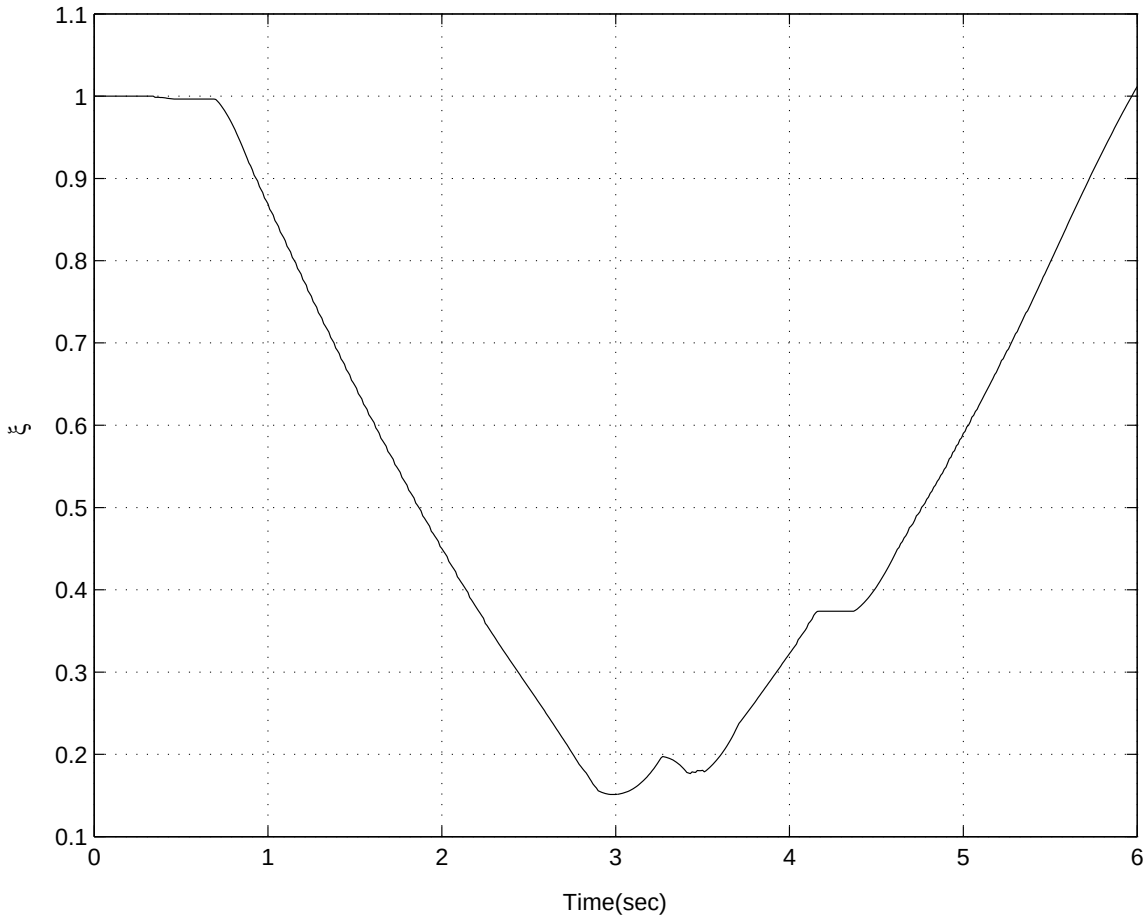

Figure 3.14: Phase transformation model works properly: martensite fraction

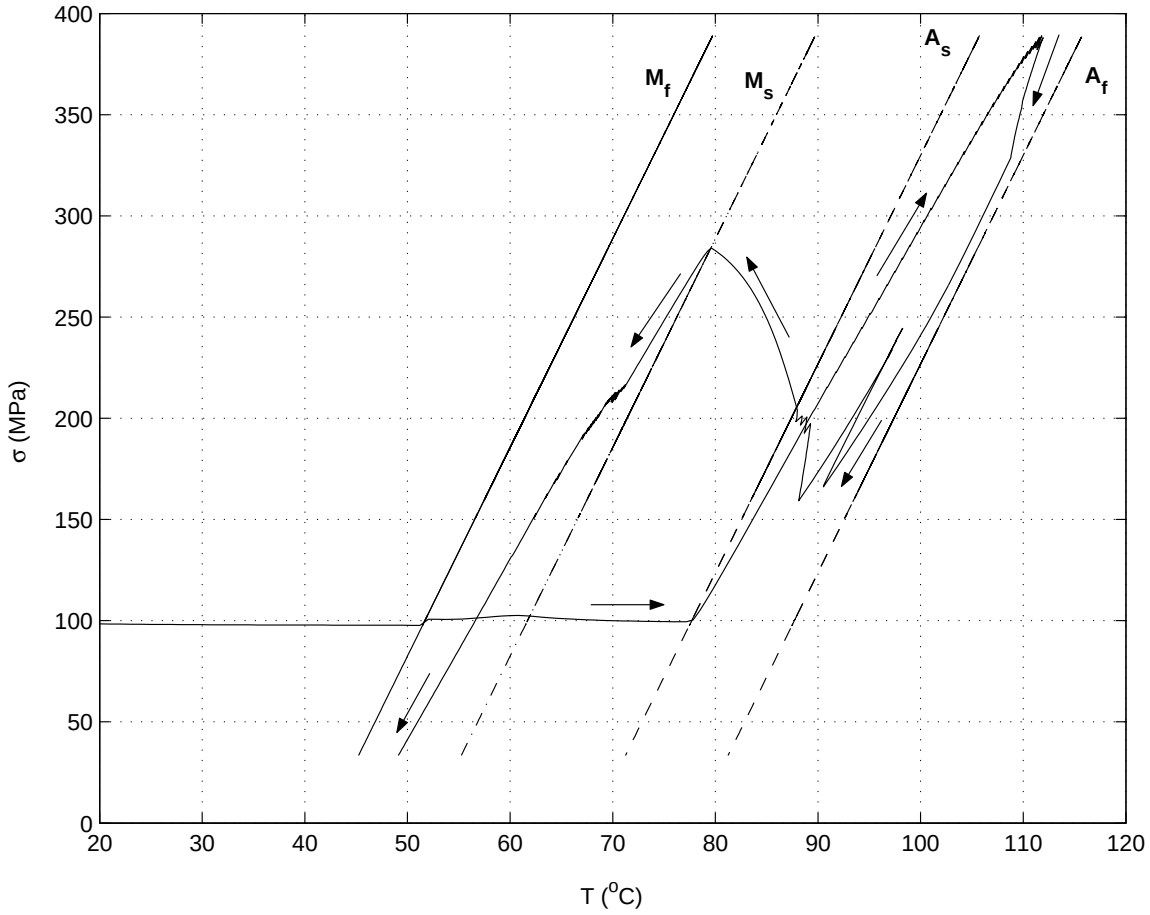

Figure 3.15: Phase transformation model works properly: stress vs. temperature

3.5 Experimental Study

To further investigate the SMA model discrepancy, a dead-weight SMA-actuator, as shown in Fig. 3.16, is experimentally studied. This simpler system is chosen to better study the models shortcomings at a more fundamental level. When the stress-free austenite phase cools down below the martensite final temperature the twinned martensite appears. Upon loading the twinned martensite above a certain stress level, the detwinning and hence the elongation process takes place . For the bias-type SMA actuators, there is always a force/torque to bring the phase from austenite back to the detwinned martensite. In this experimental study, the bias-force is provided by the weight of a variable mass. The transformation phenomenon explained in Section 2 is summarized in Fig. 3.17. For all the cases that are shown in this figure, the phenomenological models presented by Liang [9] and Brinson [8] are able to predict the behavior of the SMA wire. It is worth noting that for all these cases the phase transformation takes place while either stress or temperature is constant. However, when an SMA wire is used as an actuator, the phase transformation, most of the time, is neither isostress nor isothermal. An example of such cases was shown in Fig. 3.11c. When an SMA element is heated and therefore undergoes a partial martensite to austenite phase transformation, if the stress in the wire decreases the transformation temperature A_s and A_f also decrease. If the stress decrease is large enough, the temperature of the SMA element can exceed the austenite final temperature even if the temperature itself remains unchanged. Let's have a closer look at the phase transformation kinetics of the existing phenomenological

models, Equation 3.3 can be rewritten as:

$$\xi = \frac{\xi_M}{2}\{\cos[a_A(T - A_s) + b_A\sigma] + 1\} \tag{3.9}$$

which can be expanded as:

$$\xi = \frac{\xi_M}{2}\{\cos[(T - A_s - \sigma/C_A)\frac{\pi}{A_f - A_s}] + 1\} \tag{3.10}$$

This equation describes the martensite to austenite (reverse) phase transformation that takes place under two different thermomechanical loadings:

- In the SMA actuators, the reverse phase transformation takes place when a fully or partially martensitic material is heated.
- The reversed transformation also can occur when a previously loaded austenitic SMA element is unloaded. The reverse transformation follows the transformation of austenite to stress-induced martensite due to the loading.

Liang and Brinson have formulated the conditions for these two cases of the reverse transformation. Liang formulated the condition for the reverse transformation due to the heating ($\dot{T} > 0$) as:

$$A_s + \frac{\sigma}{C_A} \leq T \leq A_f + \frac{\sigma}{C_A} \tag{3.11}$$

According to the condition of Equation 3.11, in a case similar the one shown in Fig. 3.11c, since the wire's temperature is not increasing, even though the temperature reaches beyond the stress-modified austenite final temperature, no martensite to austenite phase transformation beyond point 1 takes place.

The Brinson's formulation of the reverse transformation due to unloading ($\dot{\sigma} < 0$) is written as:

$$C_A(T - A_s) \geq \sigma \geq C_A(T - A_f) \tag{3.12}$$

The thermomechanical loading shown in Fig. 3.11c and hence the possible phase transformation caused by it cannot be described with Brinson's condition, Equation 2.14. No stress-induced martensite has been previously formed in the SMA wire that can be transformed back to austenite upon unloading.

In the next two sections, it is shown experimentally that a thermomechanical loading similar to the one shown in Fig. 3.11c can cause further martensite to austenite phase transformation. Therefore, the existing phenomenological models need further improvements to predict the behavior of the SMA elements under similar complex thermomechanical loadings.

Experimental Setup

The experimental setup, as illustrated in Fig. 3.16, consists of a stack of mass that is actuated vertically by an SMA wire. The stress applied to the SMA wire can be adjusted by adding mass to or removing mass from the stack. The motion of the mass is measured using a Linear

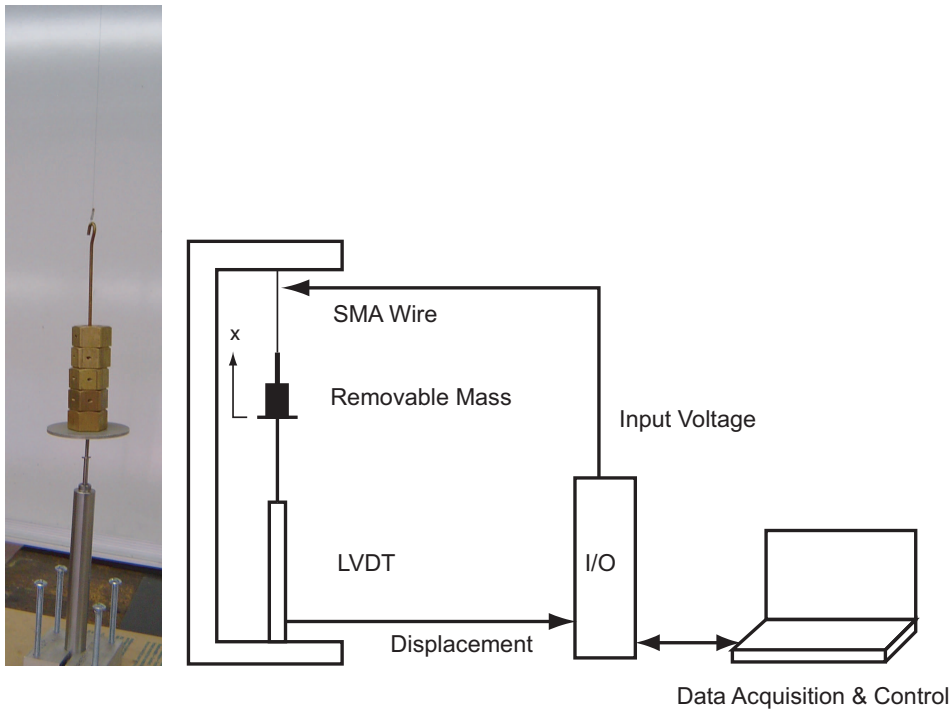

Figure 3.16: Test setup consists of an SMA wire, a removable mass, LVDT, and a personal computer

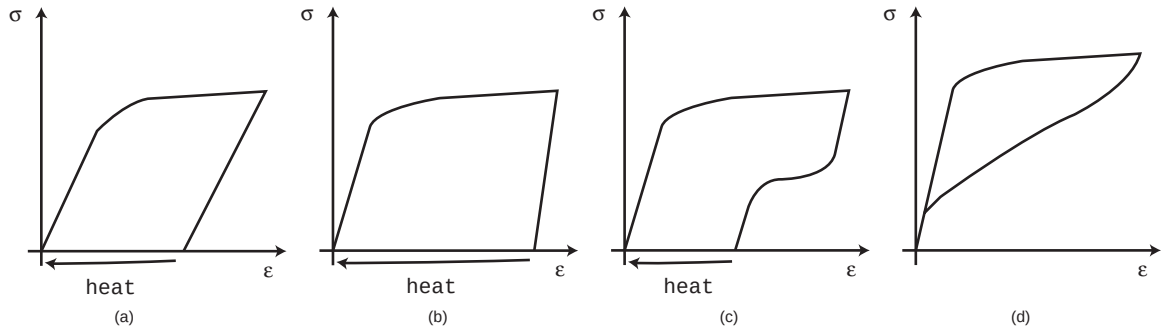

Figure 3.17: Mechanical behavior of the shape memory alloy. The nonlinear portion of the plot is due to detwinning the martensite variants or transforming the austenite to martensite. (a) $T < A_s$ at the beginning material is fully martensitic (b) $M_s < T < A_s$ at the beginning material is fully austenitic (c) $A_s < T < A_f$ at the beginning material is fully austenitic (d) $T > A_f$ at the beginning material is fully austenitic

Variable Differential Transformer (LVDT). A personal computer records this measurement and generates the voltage signals, which are amplified before being applied to the SMA wire. The system can be modeled as:

$$m\ddot{x} + b\dot{x} + mg = F_w \tag{3.13}$$

where x is the mass vertical displacement, m is the mass, and b is the viscous friction that approximates the effect of damping and friction. F_w is the force applied by the SMA wire on the mass in the vertical direction. The strain of the SMA wire and the displacement of the mass form a kinematic relationship:

$$\dot{\varepsilon} = -\frac{\dot{x}}{l_0} \tag{3.14}$$

here l_0 is the initial length of the SMA wire. In this analysis the Young's modulus and the resistance of the wire are assumed to change as the result of the phase transformation:

$$\begin{aligned} R &= R_A + \xi(R_M - R_A) \\ E &= E_A + \xi(E_M - E_A) \end{aligned} \tag{3.15}$$

the subscripts A and M, respectively indicate the austenite and martensite phases. The Flexinol® SMA wire's diameter, used to actuate the system, is 150μm and the initial stress, created by a mass of 75g, is 41.6MPa. This stress is enough to elongate the wire to fully

Table 3.2: Flexinol SMA wire parameters and their value

Parameter	Description	Value
$R_{eM}(\mu\Omega\text{cm})$	Resistivity (martensite)	76
$R_{eA}(\mu\Omega\text{cm})$	Resistivity (austenite)	84
$A_s(^o\text{C})$	Austenite start temperature	68
$A_f(^o\text{C})$	Austenite final temperature	78
$M_s(^o\text{C})$	Martensite start temperature	52
$M_f(^o\text{C})$	Martensite final temperature	42
$C_p(\text{cal/g}^o\text{C})$	Specific heat	0.077
$\Delta H(\text{Joule/g})$	Latent heat	24.2
$E_M(\text{GPa})$	Young modulus (martensite)	28
$E_A(\text{GPa})$	Young modulus (austenite)	75
$C_M(\text{MPa/}^o\text{C})$	Effect of stress on transformation temperatures (martensite)	6.89
$C_A(\text{MPa/}^o\text{C})$	Effect of stress on transformation temperatures (austenite)	6.89
$\rho(\text{g/cc})$	Density	6.45

detwinned martensitic phase at the ambient temperature $T_\infty = 23^oC$, therefore, the SMA wire is initially fully martensitic, i.e., $\xi = 1$. The initial length of the wire is $l_0 = 537$mm. Other properties of the wire are shown in Table 3.2.

3.5.1 Experimental Results

The behavior of the SMA wire for several step function inputs is presented in Fig. 3.18. It can be seen that for large enough voltage inputs ($U > 4$V) the SMA wire undergoes a significant martensite to austenite phase transformation, hence the mass moves up. The steady state temperature of the SMA wire increases as higher voltages are applied. As a result, the SMA wire transforms more from martensite to austenite and therefore the mass moves higher as the applied voltage increases. When the input voltage is switched to zero,

the SMA wire is cooled down and the stress applied by the mass elongates the wire to its initial length as shown in the Fig. 3.19.

Figures 3.18- 3.22 illustrate variation in the behavior of the SMA wire with similar voltage inputs. In these experiments the wire is stretched by the mechanical load of m = 75g. This elongation is partly recovered upon heating. The recovered strain depends on the applied-constant-voltage, which has the range of 1V to 16V. It is worth noting that with the same voltage, the amount of recovered strain is slightly different. The variation of the recovered strain in steady state, as shown in Fig. 3.23, is a function of applied voltage and therefore is a function of the phase transformation. This variation is smaller when the wire either has recovered a very small amount of strain or is close to the full strain recovery. The variation in the recovered strain can be associated with nonuniform temperature distribution for the middle voltage range.

In order to simulate a thermomechanical loading under which the behavior of SMA wires cannot be predicted by the existing SMA models, the temperature of a partially transformed wire was maintained constant while the stress was reduced. This thermomechanical loading is similar to the one shown in Fig. 3.11c. To this end, a constant voltage was applied to the SMA wire. Due to the applied stress by the hanging mass the SMA wire was initially extended in the martensite phase. When the temperature was raised, the wire contracted due to martensite to austenite phase transformation. After the wire reached the steady state length part of the mass was removed and the wire was allowed to again reach the steady state. Finally, the removed mass was added to the hanging mass. Figures 3.24- 3.33 illustrate the

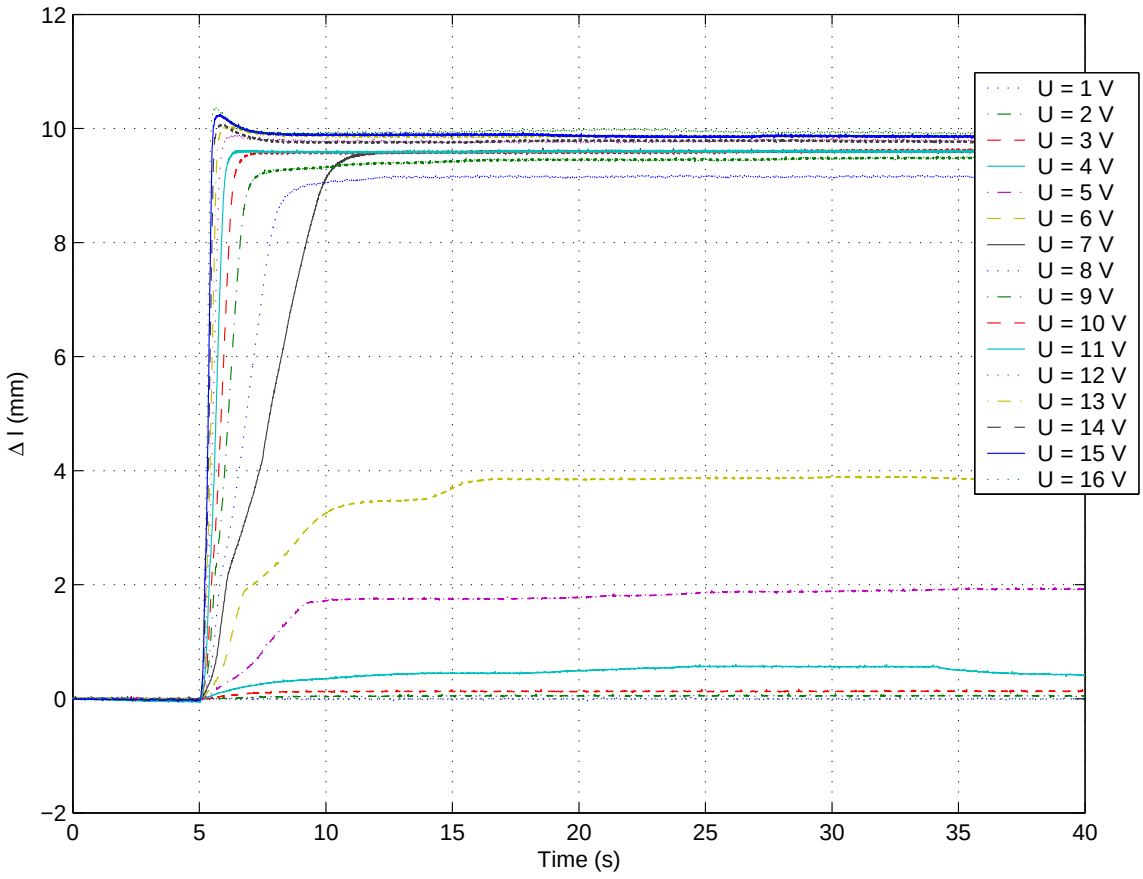

Figure 3.18: Experimental behavior of the SMA wire for several step voltage inputs with mechanical load of m = 75g

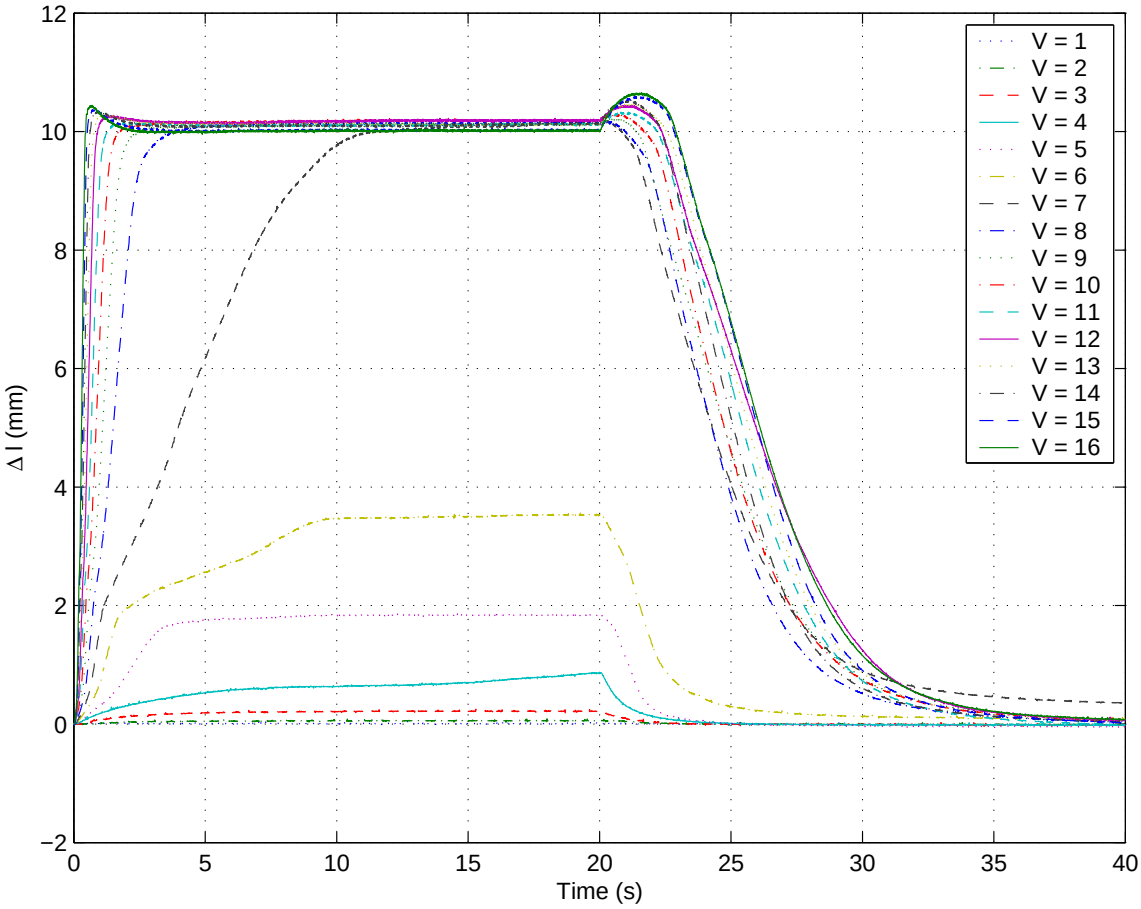

Figure 3.19: Experimental heating (form 0 to 30 sec) and cooling (form 30 to 60 sec) behavior of the SMA wire for several step voltage inputs with mechanical load of m = 75g

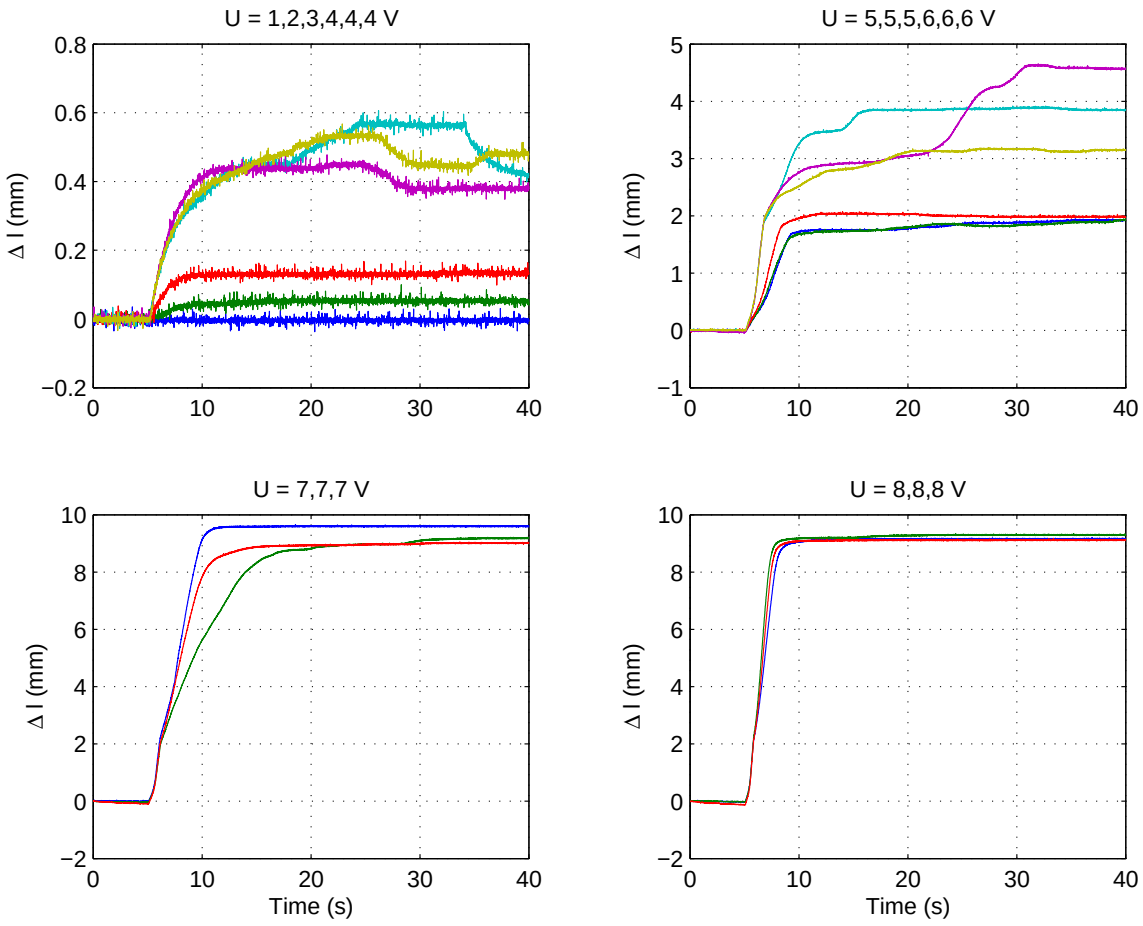

Figure 3.20: Variation of the experimental behavior of the SMA wire for V = 1V to V = 8V with mechanical load of m = 75g

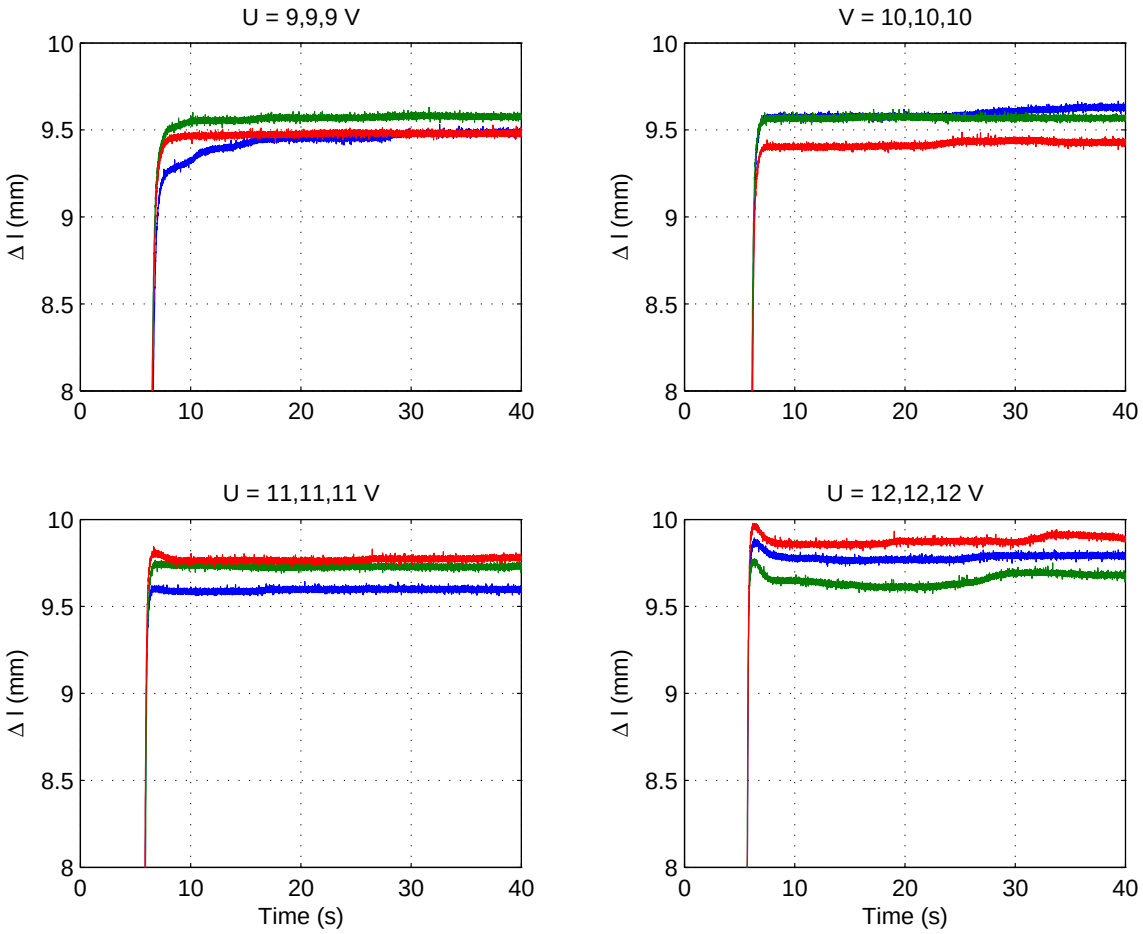

Figure 3.21: Variation of the experimental behavior of the SMA wire for V = 9V to V = 12V with mechanical load of m = 75g

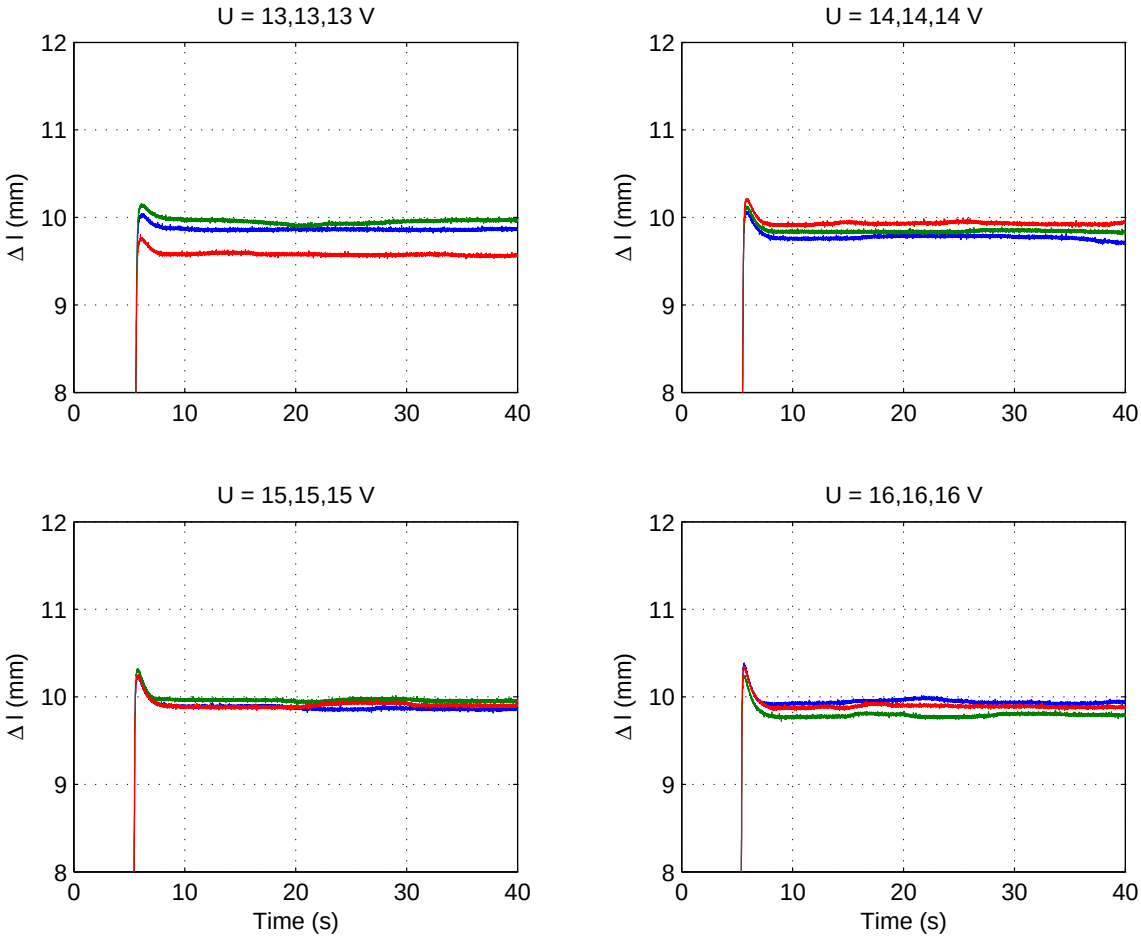

Figure 3.22: Variation of the experimental behavior of the SMA wire for V = 13V to V = 16V with mechanical load of m = 75g

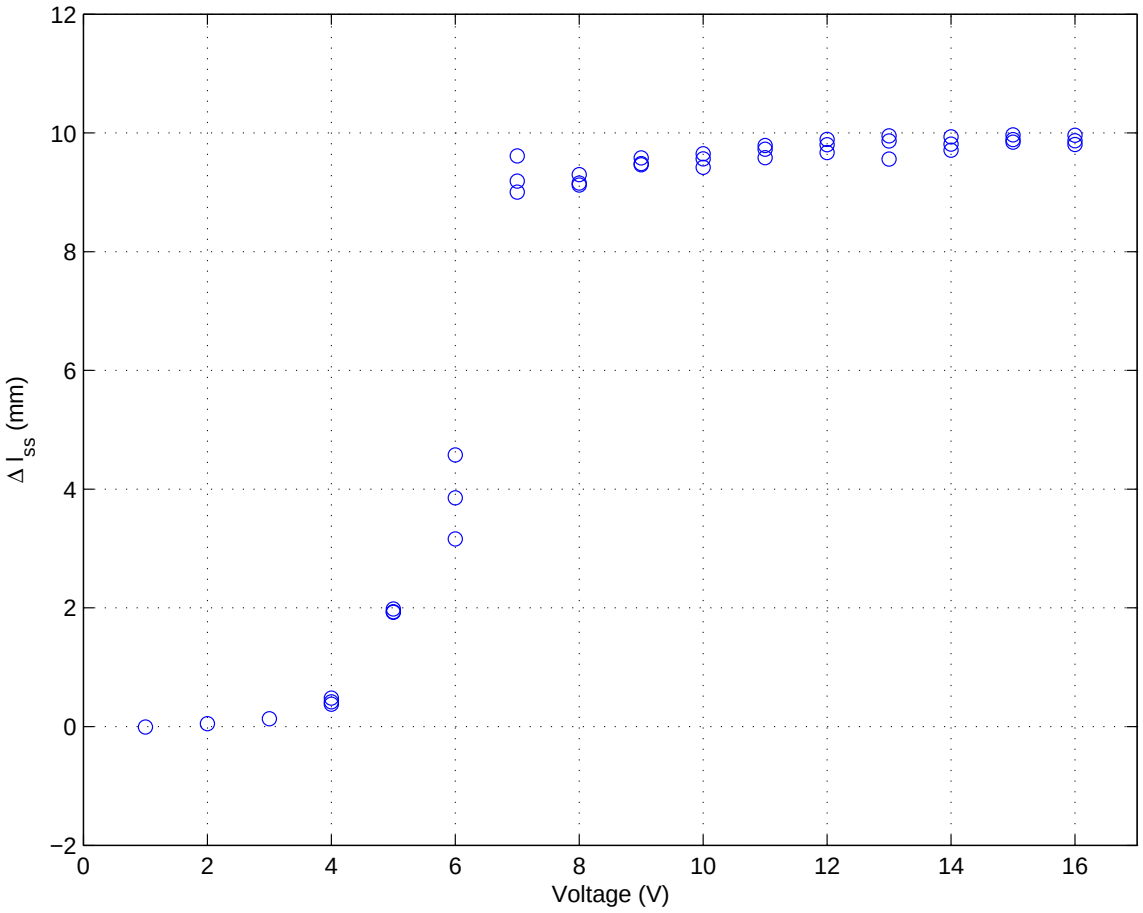

Figure 3.23: Variation of the experimental behavior of the SMA wire as a function of the input voltage with mechanical load of m = 75g

result of several such experiments. Each figure shows results of three experiments that were performed with the same mechanical load change. In all these experiments the initial mass was 388g, which was reduced and then increased either in one step, as shown in Figs. 3.24-3.31 or in several steps, as illustrated in Figs. 3.32 and 3.33.

As a representative example, Figs. 3.24, 3.25, and 3.26 show that the SMA wire actuated the hanging mass farther upwards when the mass was reduced by 96g. The wire underwent some deflection upon addition of the removed mass. The net deflection of the wire is a representative of the additional martensite to austenite phase transformation. This deflection is the difference of the steady-state length of the wire measured before removing part of the mass and after adding the removed mass. The net deflection for the three trials are slightly different:

$$\begin{aligned} \text{(Trial 1) } \Delta l_{\text{net}} &= 24.34 - 24.02 = 0.32\text{mm} \\ \text{(Trial 2) } \Delta l_{\text{net}} &= 24.19 - 23.92 = 0.27\text{mm} \\ \text{(Trial 3) } \Delta l_{\text{net}} &= 23.80 - 23.52 = 0.28\text{mm} \end{aligned} \tag{3.16}$$

In the next section it will be shown that the phase transformation can be calculated using the measured net deflection.

As previously mentioned, the transformation due to reducing the external load and hence the stress of the wire, is not predicted by the existing phase transformation models. Therefore, there is a need for further investigation of the phase kinetics models to be used for SMA

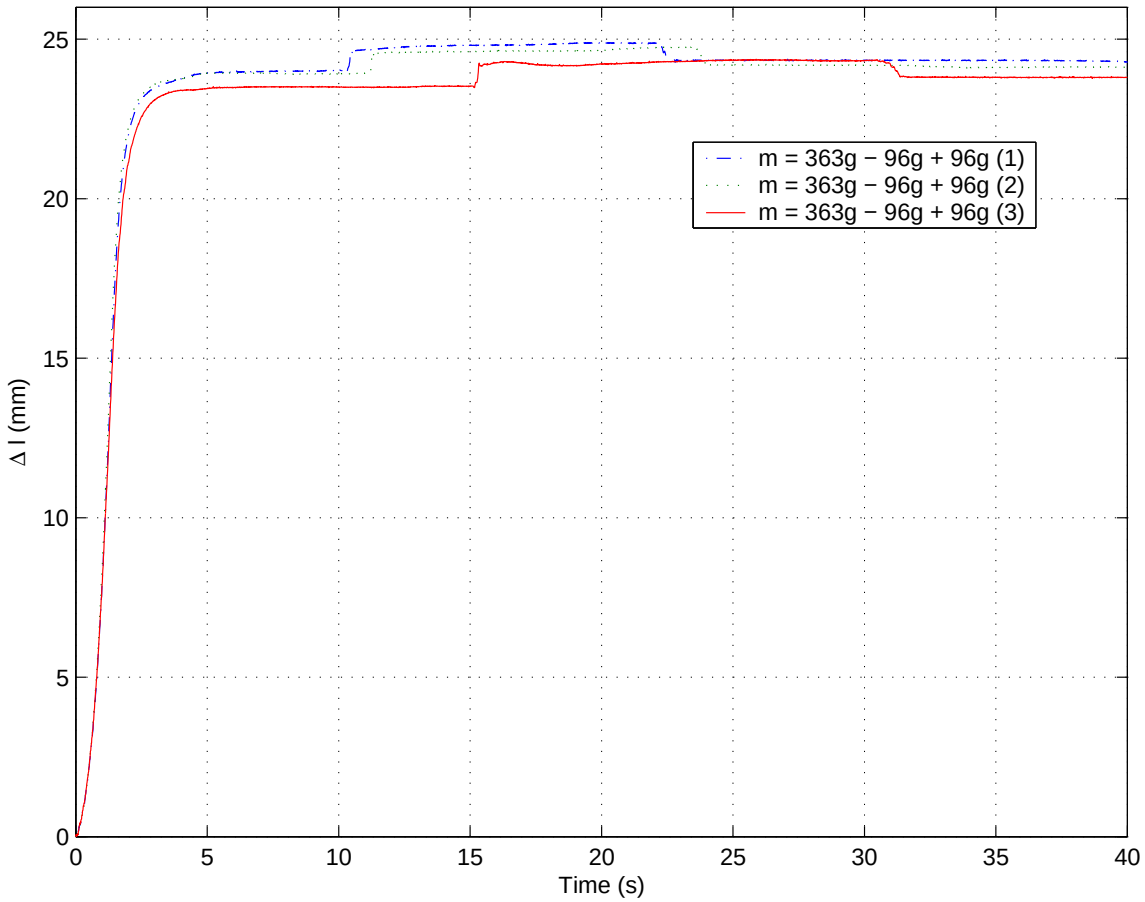

Figure 3.24: Experimental behavior of the SMA wire with changing mechanical load, initial mass m = 363g, change in mass Δm = 96g, voltage U = 16V

actuator design and simulations.

3.6 The Enhanced Phenomenological Model

In this section, an SMA phenomenological model, which is capable of describing the behavior of SMA wires under complex thermomechanical loadings is presented. To this end, the existing phase kinetic models are modified to include the effect of complex thermomechanical

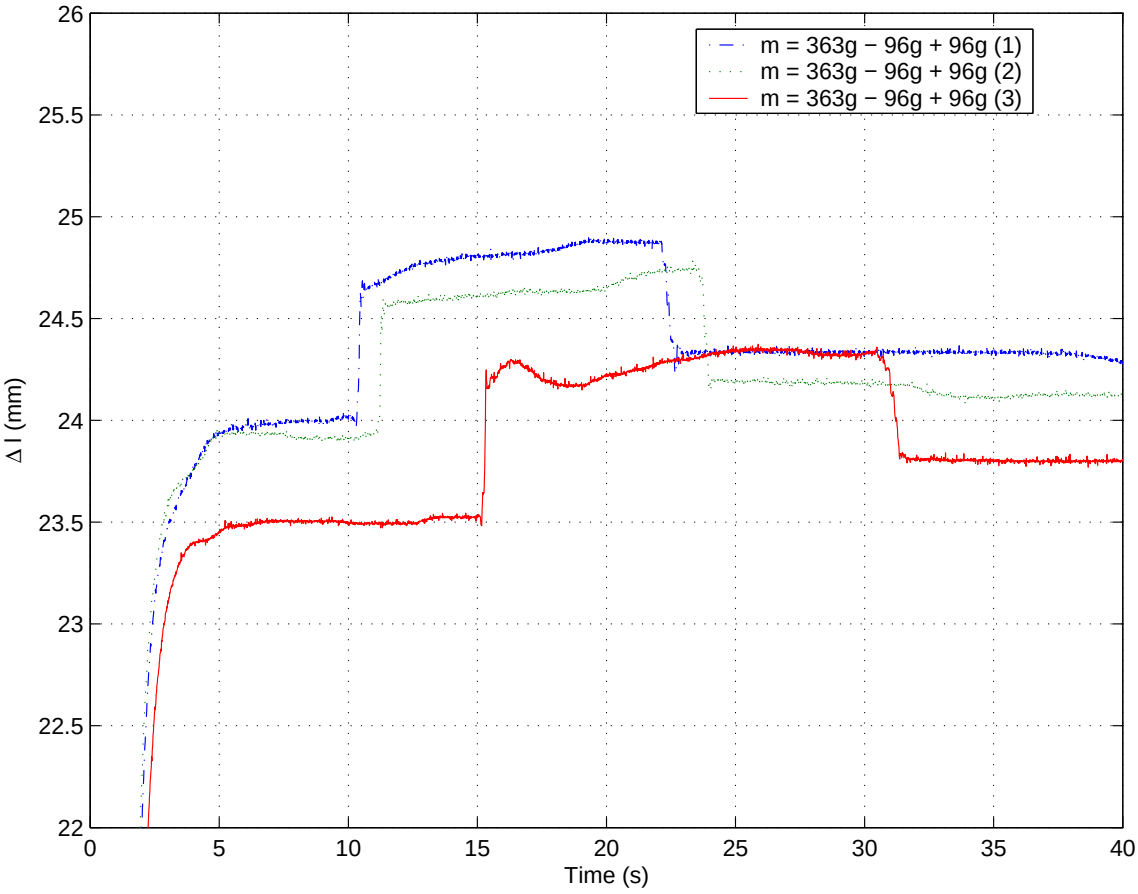

Figure 3.25: Experimental behavior of the SMA wire with changing mechanical load, initial mass m = 363g, change in mass Δm = 96g, voltage U = 16V (closer view)

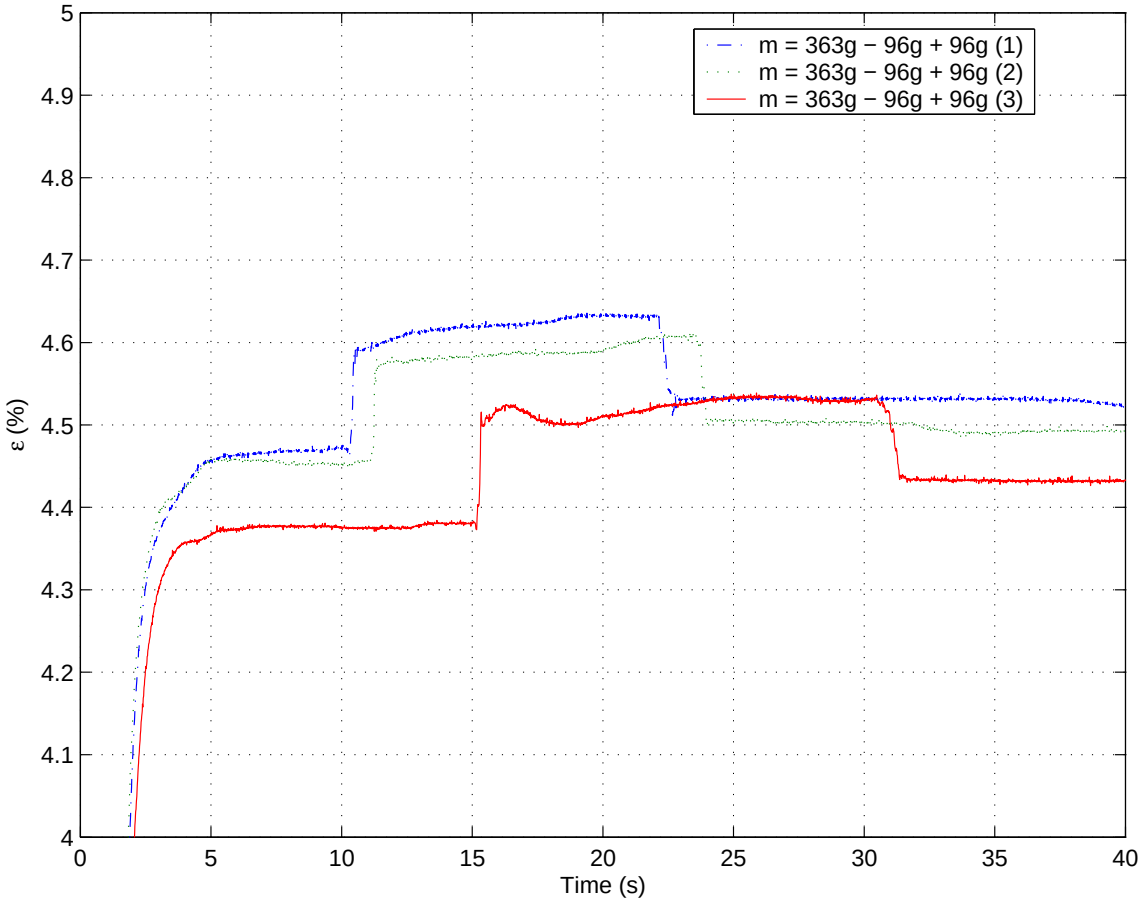

Figure 3.26: Experimental behavior of the SMA wire (strain) with changing mechanical load, initial mass m = 363g, change in mass Δm = 96g, voltage U = 16V

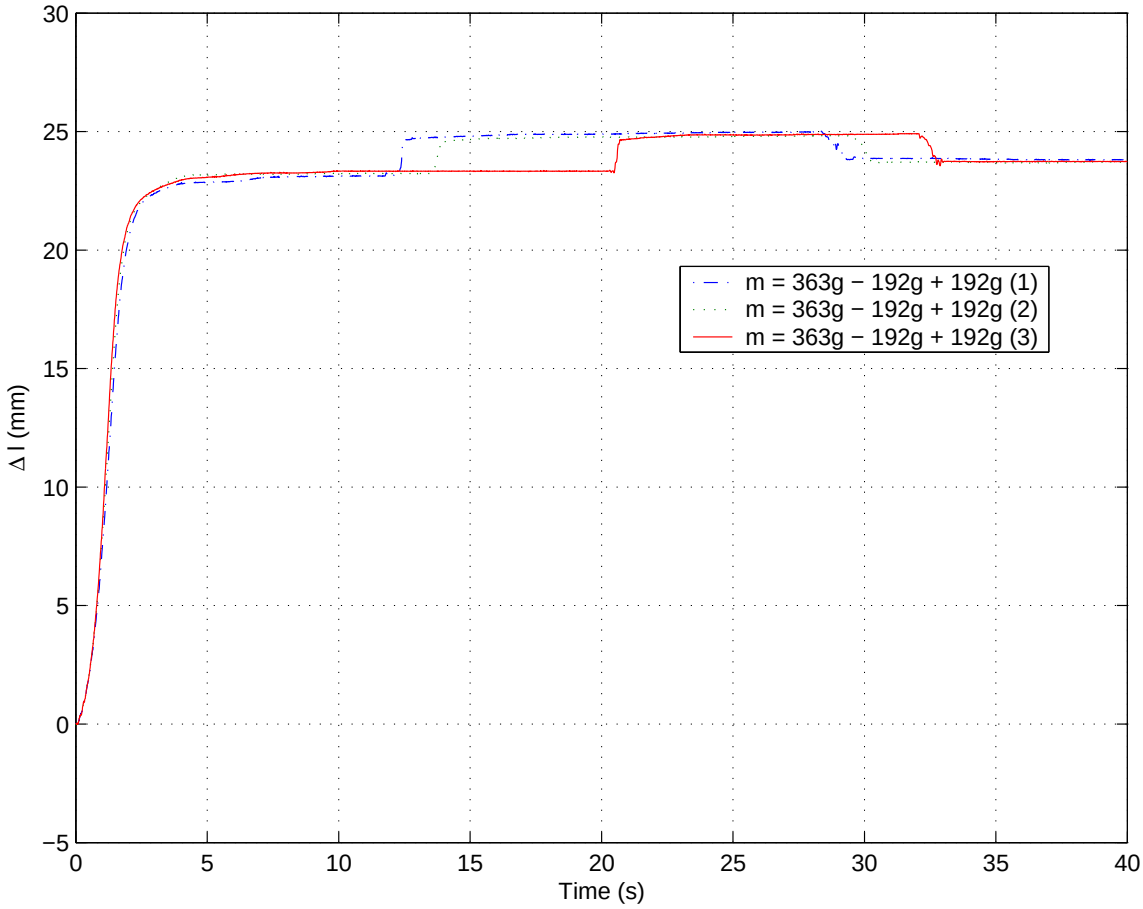

Figure 3.27: Experimental behavior of the SMA wire with changing mechanical load, initial mass m = 363g, change in mass Δm = 192g, voltage U = 16V

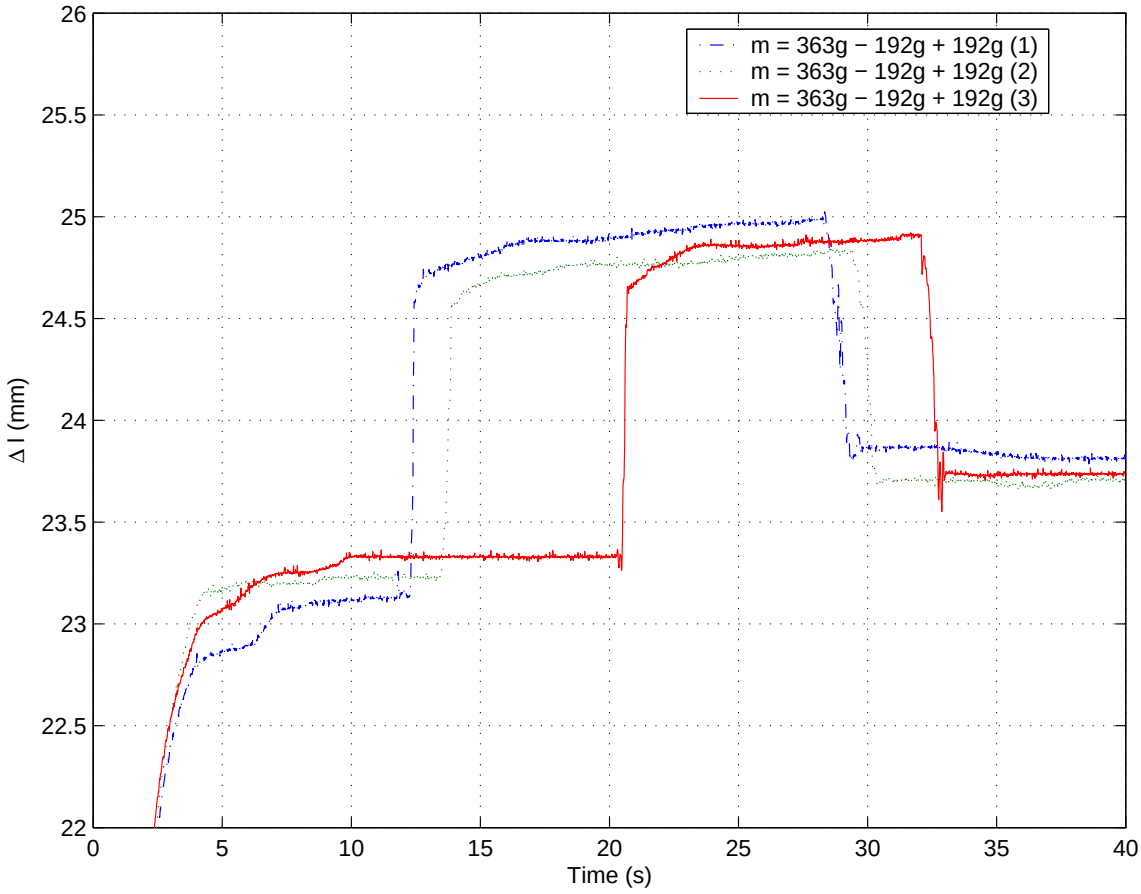

Figure 3.28: Experimental behavior of the SMA wire with changing mechanical load, initial mass m = 363g, change in mass Δm = 192g, voltage U = 16V (closer view)

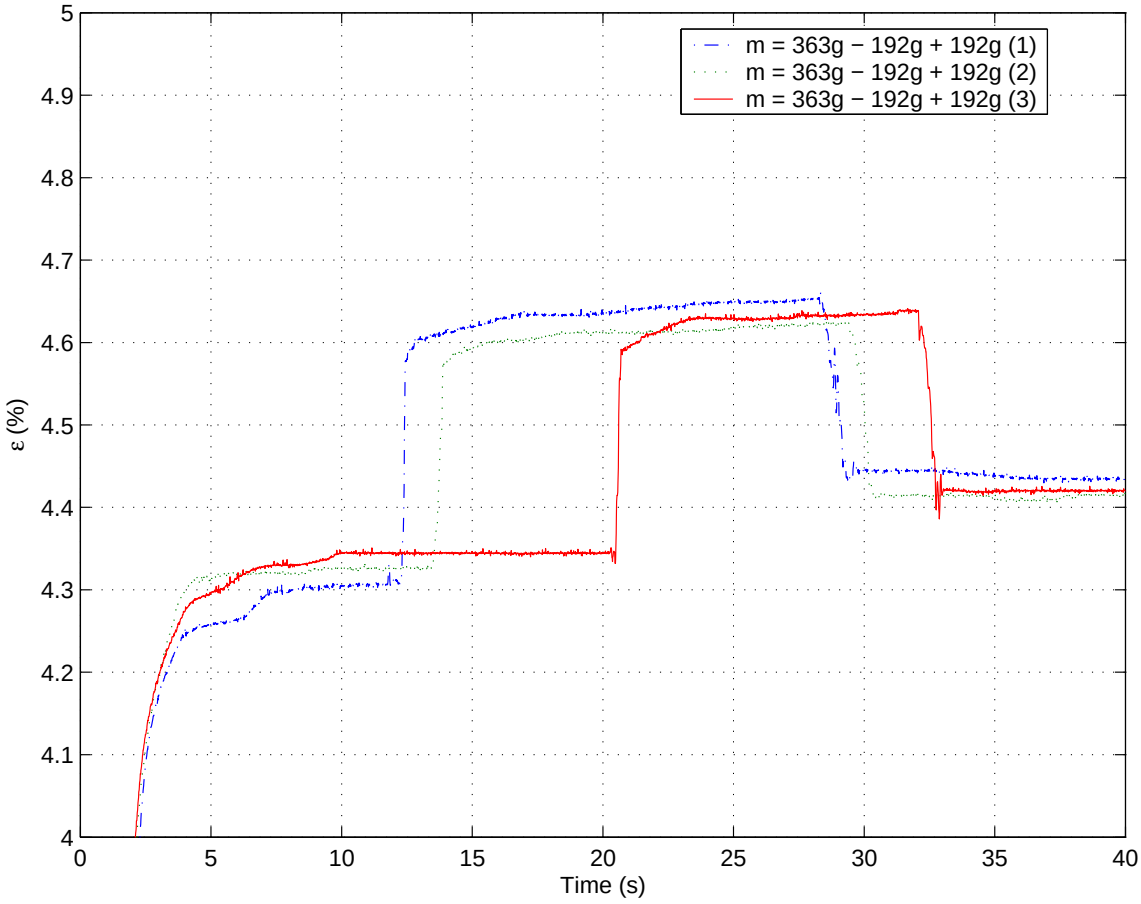

Figure 3.29: Experimental behavior of the SMA wire (strain) with changing mechanical load, initial mass m = 363g, change in mass Δm = 96g, voltage U = 16V

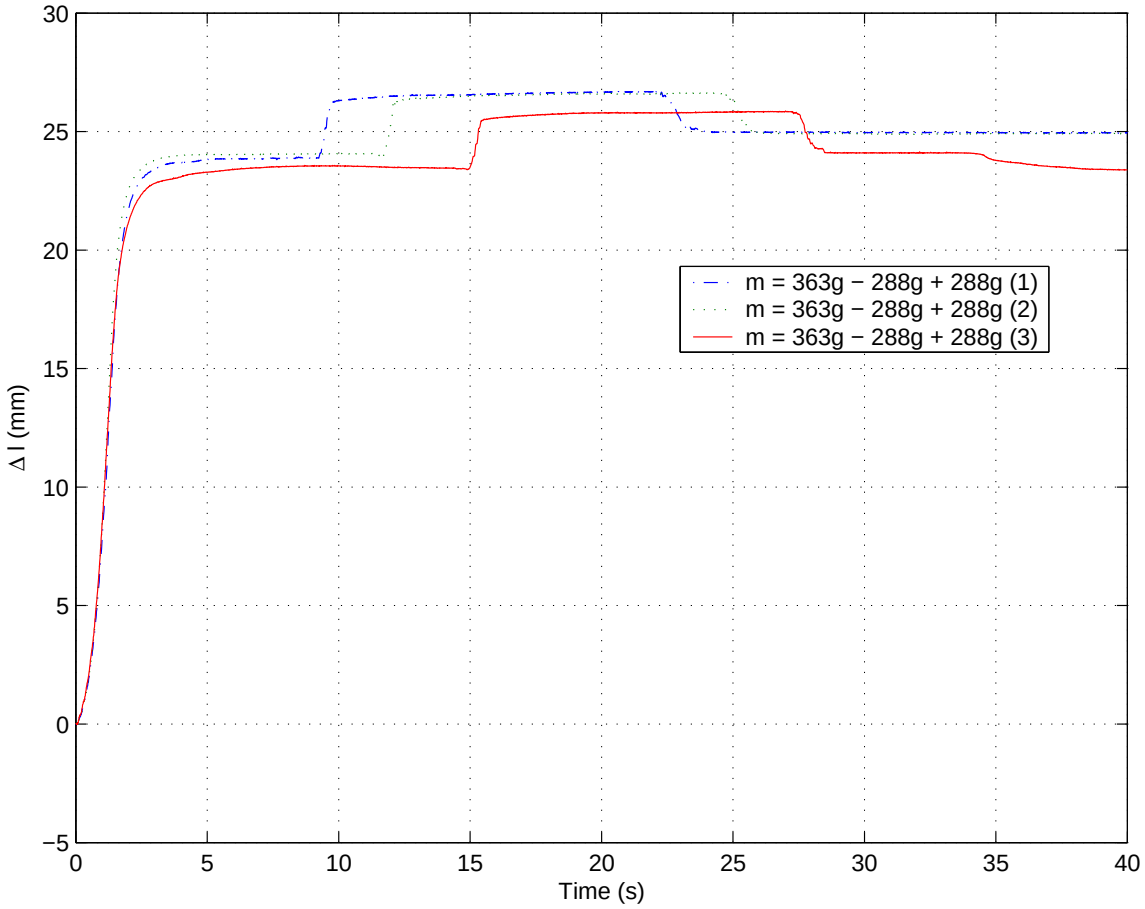

Figure 3.30: Experimental behavior of the SMA wire with changing mechanical load, initial mass m = 363g, change in mass Δm = 288g, voltage U = 16V

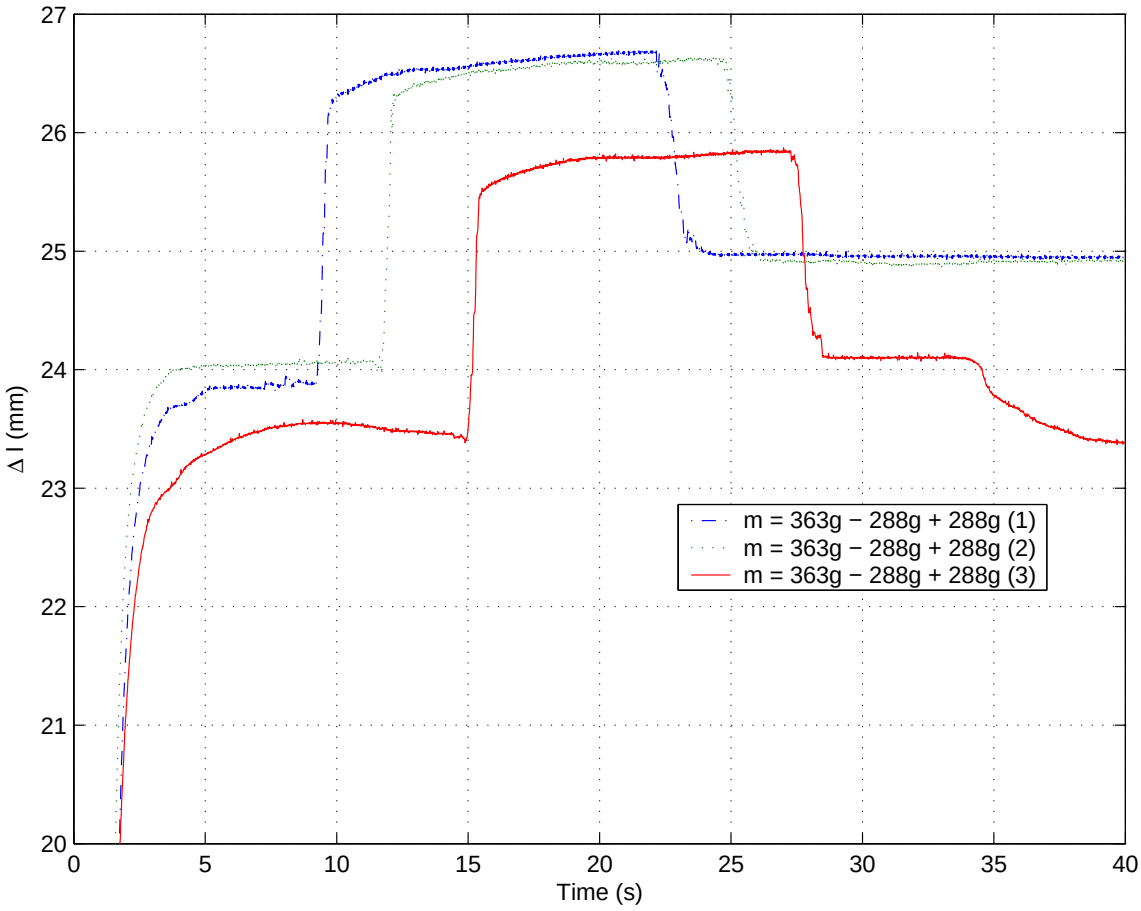

Figure 3.31: Experimental behavior of the SMA wire with changing mechanical load, initial mass m = 363g, change in mass Δm = 288g, voltage U = 16V (closer view)

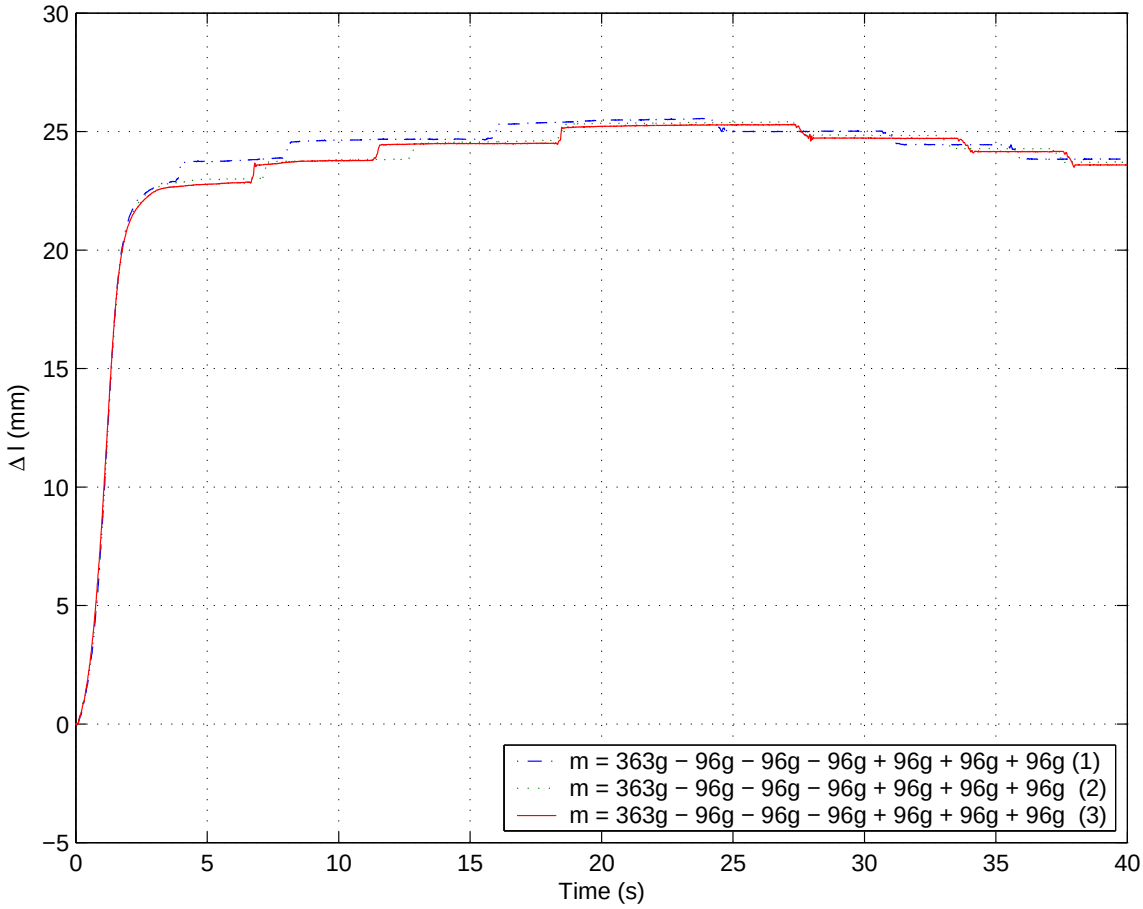

Figure 3.32: Experimental behavior of the SMA wire with changing mechanical load, initial mass m = 363g, change in mass Δm = 288g in three steps, voltage U = 16V

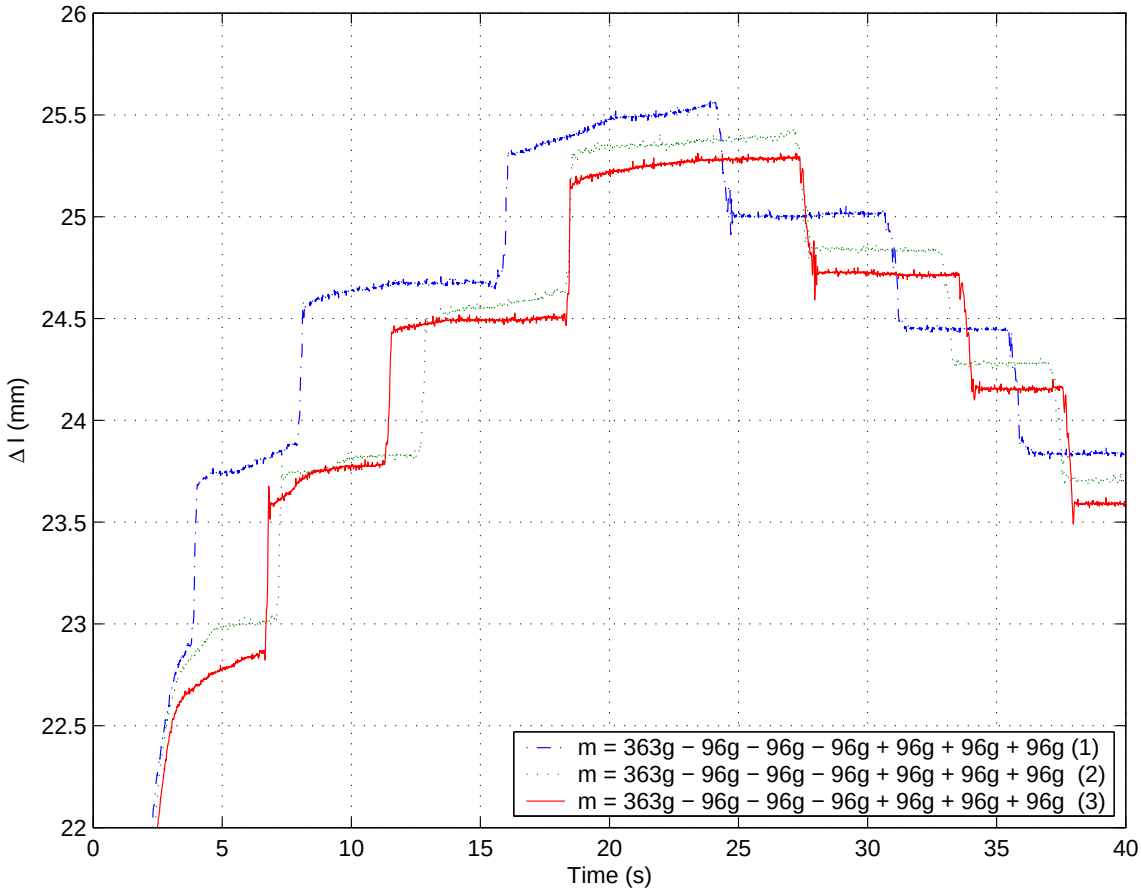

Figure 3.33: Experimental behavior of the SMA wire with changing mechanical load, initial mass m = 363g, change in mass Δm = 288g in three steps, voltage U = 16V (closer view)

loadings. Examples of such complex loadings were presented in Sections 3.4 and 3.5.

The enhanced model is a phenomenological model consisting of two parts: the constitutive equation and the phase kinetics equations. The constitutive equation is the same constitutive equation developed by Tanaka and adopted by both Liang and Brinson, written in the derivative form:

$$\dot{\sigma} = E(\xi)\dot{\varepsilon} + \theta_T \dot{T} + \Omega\dot{\xi}$$

The phase kinetics model is based on the same cosine functions developed by Liang and later adopted by Brinson rather than the exponential functions used by Tanaka. The conditions for the phase transformation are modified to include the effect of the complex loadings. The resulting model is able to predict the behavior of SMAs under complex thermomechanical loadings.

The martensite to austenite phase transformation kinetics, as was presented in Equation 3.3, is a cosine function of the temperature and stress:

$$\xi = \frac{\xi_M}{2}\{\cos[a_A(T - A_s) + b_A\sigma] + 1\}$$

The conditions under which this transformation takes place were presented by Liang and Brinson as Equations 3.11 and 3.12, respectively. In the enhanced model, we have modified these conditions as follows. The SMA element will undergo the martensite to austenite phase transformation while , in the stress-temperature plane, the distance between the stress-modified austenite final temperature and the temperature of the SMA element are reduced.

This condition can be written as:

$$\dot{T} - \frac{\dot{\sigma}}{C_A} > 0$$

and

$$A_s + \frac{\sigma}{C_A} < T < A_f + \frac{\sigma}{C_A} \tag{3.17}$$

Similarly, the austenite to martensite phase transformation kinetics, which is rewritten here, is adopted.

$$\xi = \frac{1 - \xi_A}{2} \cos[a_M(T - M_f) + b_M\sigma] + \frac{1 + \xi_A}{2}$$

The conditions under which the phase transformation takes place are modified as:

$$\dot{T} - \frac{\dot{\sigma}}{C_M} < 0$$

and

$$M_f + \frac{\sigma}{C_M} < T < A_s + \frac{\sigma}{C_M} \tag{3.18}$$

Equations 3.17 and 3.18 define the transformation paths as illustrated, on the stress-temperature plane, in Fig. 3.34. All the experiments performed in this chapter follow the martensite to austenite phase transformation that takes place along the "a-c" path on Fig. 3.34.

It is worth noting that the modified phase transformation kinetics will be reduced to the

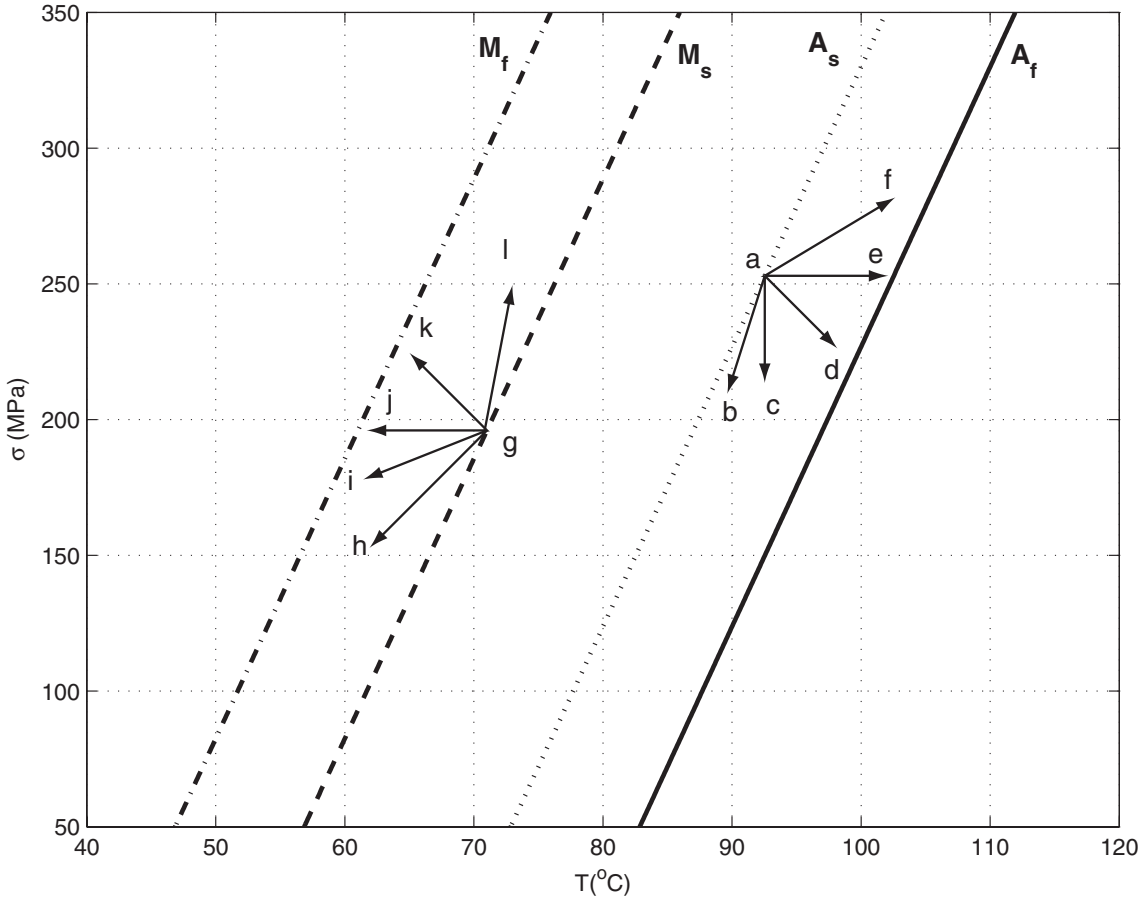

Figure 3.34: Phase transformation as predicted by the enhanced phenomenological model; martensite to austenite transformation takes place for all the loading paths starting from point a; austenite to martensite phase transformation takes place for all the loading paths starting from point g

Table 3.3: Comparing phase transformation condition of four SMA phenomenological models: Tanka, Liang, Brinson, and the Enhanced Model

Author	Martensite to Austenite Transformation	Austenite to Martensite Transformation
Tanaka [1986]	$\dot{\sigma} < 0$ $\sigma \leq -(T - A_s)\frac{A_a}{B_a}$	$\dot{\sigma} > 0$ $\sigma \geq (T - M_s)\frac{A_m}{B_m}$
Liang [1990]	$\dot{T} > 0$ $A_f + \frac{\sigma}{C_A} \geq T \geq A_s + \frac{\sigma}{C_A}$	$\dot{T} < 0$ $M_s + \frac{\sigma}{C_M} \geq T \geq M_f + \frac{\sigma}{C_M}$
Brinson [1993]	$\dot{\sigma} < 0$ $C_A(T - A_s) \geq \sigma \geq C_A(T - A_f)$	$\dot{\sigma} > 0$ $C_M(T - M_f) \geq \sigma \geq C_M(T - M_s)$
Elahinia [2004]	$\dot{T} - \frac{\dot{\sigma}}{C_A} > 0$ $A_f + \frac{\sigma}{C_A} \geq T \geq A_s + \frac{\sigma}{C_A}$	$\dot{T} - \frac{\dot{\sigma}}{C_M} < 0$ $M_s + \frac{\sigma}{C_M} \geq T \geq M_f + \frac{\sigma}{C_M}$

models presented by Liang and Brinson, if the transformation is either isostress ($\dot{\sigma} = 0$) or isothermal ($\dot{T} = 0$). Table 3.3 compares this enhanced model with Tanka, Liang, and Brinson models.

In order to verify the improved prediction of the SMA behavior provided by the presented model, the rotary SMA actuated arm is simulated under conditions similar to the ones presented in Section 3.4.

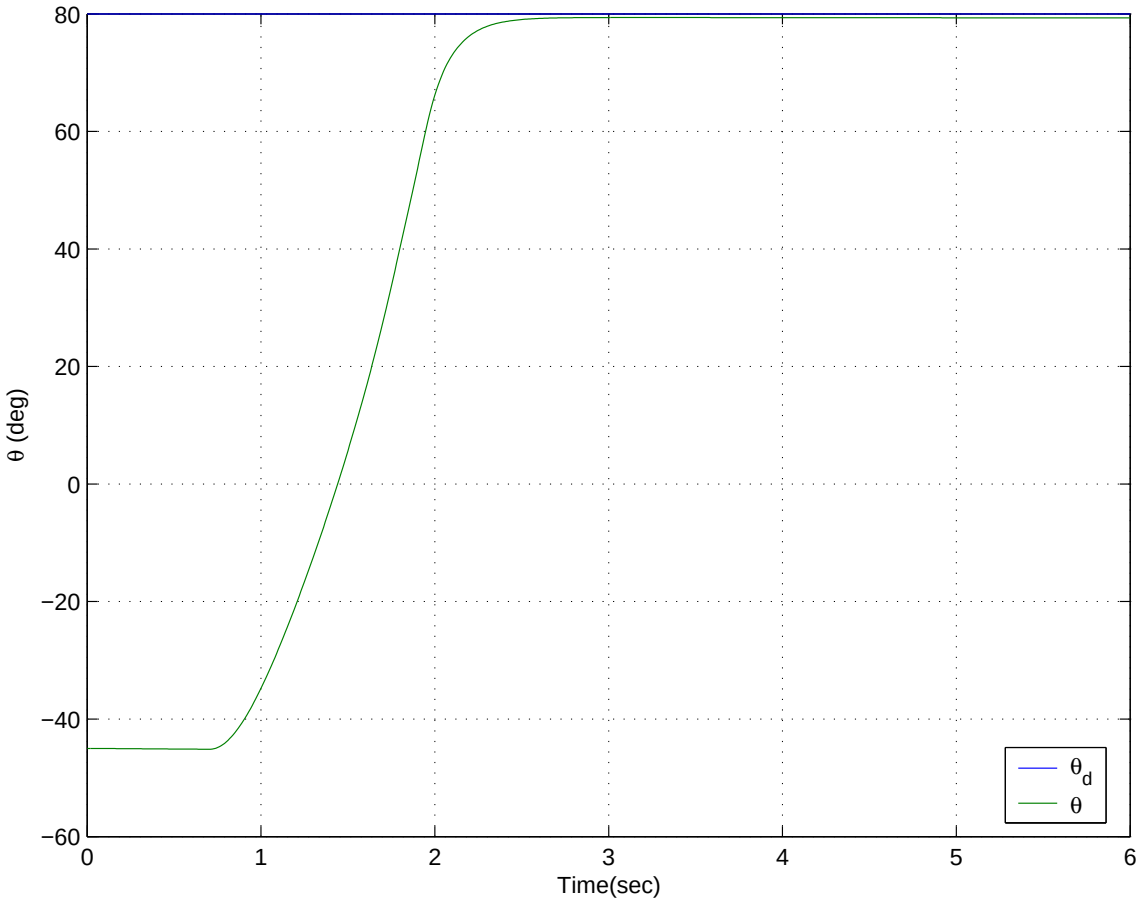

Figure 3.35: Enhanced phase transformation model: arm does reach the desired position

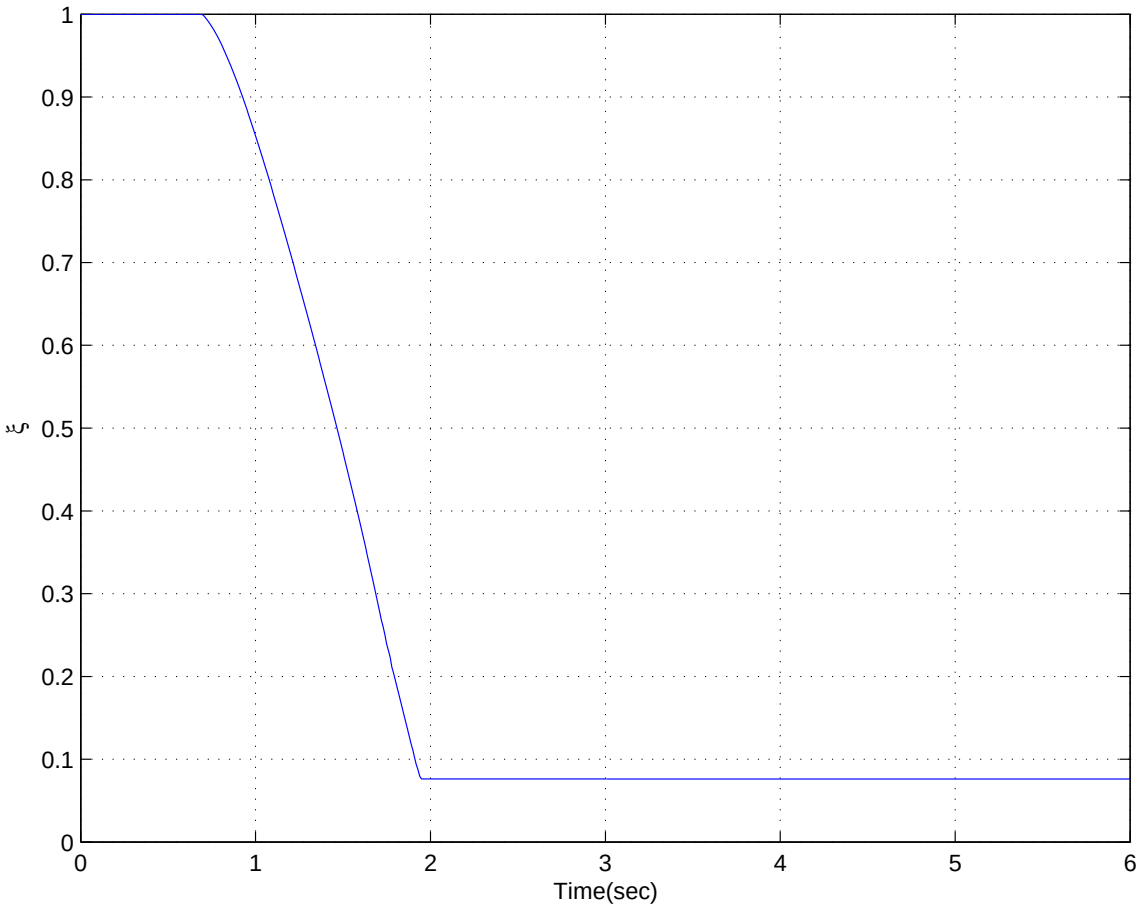

Figure 3.36: Enhanced phase transformation model: martensite fraction

Fig. 3.35 shows the simulation results with the sliding mode control. In contradiction to Fig. 3.7, with the enhanced model the arm reaches the desired position. The effectiveness of the enhanced model can be further demonstrated by comparing Figure 3.36 and 3.9. The SMA wire goes through enough transformation for the arm to be positioned at the desired angular position. In other words the enhanced model predicts more martensite to austenite phase transformation despite the fact that the temperature of the SMA wire decreases.

The enhanced model is also able to predict the behavior of the dead-weight SMA wire actuator, which was studied experimentally is Section 3.5. When some of the mass, actuated by the SMA wire, is removed the stress of the wire decreases. According to the enhanced martensite to austenite phase transformation condition, Equation 3.17, the SMA wire undergoes further martensite to austenite phase transformation and therefore, as was verified experimentally, the mass moves farther upward. The transformation takes place because the conditions for the martensite to austenite phase transformation is satisfied:

$$\dot{T} = 0$$

$$\frac{\dot{\sigma}}{C_A} < 0$$

therefore

$$\dot{T} - \frac{\dot{\sigma}}{C_A} > 0 \tag{3.19}$$

and

$$A_s + \frac{\sigma}{C_A} < T < A_f + \frac{\sigma}{C_A} \tag{3.20}$$

when the mass is increased to its initial value the stress increases. However, no phase transformation takes place because the condition for the austenite to martensite phase transformation, Equation 3.18, is not satisfied. Although, $\dot{T} - \frac{\dot{\sigma}}{C_M} < 0$ the SMA wire's temperature is not in the transformation range of $M_f + \frac{\sigma}{C_M} < T < A_s + \frac{\sigma}{C_M}$.

In order to further demonstrate that the enhanced model is capable of predicting the phase transformation that occurs as the result of isothermal-stress-change, the measurement of the second trial of Equation 3.16 is used. Considering the constitutive equation:

$$\dot{\sigma} = E(\xi)\dot{\varepsilon} + \theta_T \dot{T} + \Omega\dot{\xi}$$

the amount of mass is the same before removing and after adding the removed mass. Therefore, the stress of the SMA wire is the same. Also, the temperature of the wire is constant because the applied voltage and the ambient temperature were unchanged. The constitutive equation, therefore, reduces to:

$$E(\xi)\Delta\varepsilon = -\Omega\Delta\xi = \varepsilon_L E(\xi)\Delta\xi \tag{3.21}$$

the net phase transformation can be calculated as:

$$\begin{aligned} \xi_2 - \xi_1 &= \frac{\varepsilon_2 - \varepsilon_1}{\varepsilon_L} = \frac{\Delta l_{\text{net}}}{\varepsilon_L l_0} = \frac{\Delta l_{\text{net}}}{\Delta l_{\max}} \\ \xi_2 - \xi_1 &= \frac{0.27}{24.75} = 0.011 \end{aligned} \tag{3.22}$$

It is worth noting that the transformation temperatures were reduced as a result of reducing the mass by $m = 96$g. The stress of the SMA wire was reduced by:

$$\Delta\sigma = \frac{\Delta mg}{A_w} = \frac{(.343 - .096)g}{A_w} = 137.12\text{MPa} \tag{3.23}$$

Due to the reduced stress, both austenite start and austenite final temperature dropped by:

$$\frac{\Delta\sigma}{C_A} = 13.3^oC \tag{3.24}$$

The actual value of the martensite fraction can be calculated based on the wire elongation caused by the added mass. The Young modulus of the wire can be written as:

$$\begin{aligned} E(\xi) &= (E_M - E_A)\xi + E_A \\ E(\xi) &= \frac{\sigma}{\varepsilon} = \frac{mg}{A_w\varepsilon} \\ \xi &= \frac{\frac{mg}{A_w\varepsilon} - E_A}{E_M - E_A} \end{aligned} \tag{3.25}$$

3.7 Modeling Procedure for SMA Actuators

In this section a general procedure for modeling SMA actuators is presented, and its important steps are highlighted. This procedure was used in Section 3.2 for modeling the SMA-actuated rotary arm. The model for each SMA actuator consists of four main sections:

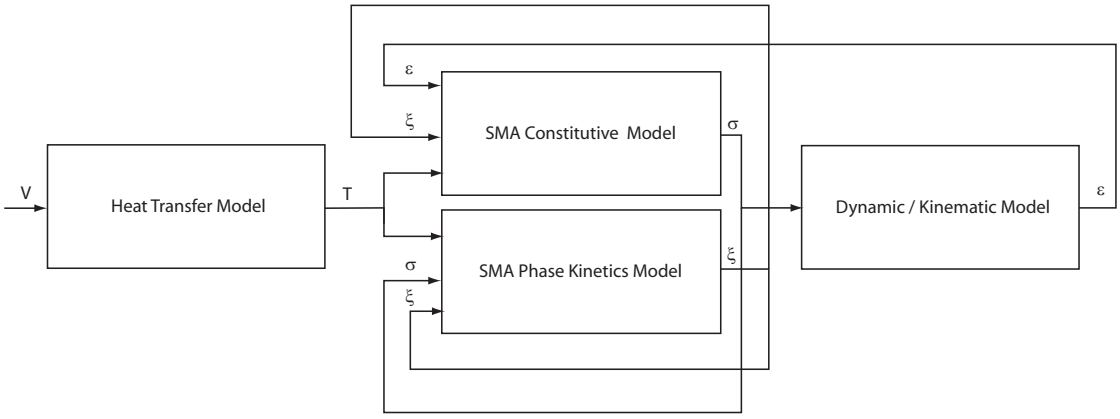

Figure 3.37: Modeling of the SMA actuators; four sub-models are inter-connected

1. heat transfer model,

2. dynamic/kinematic model,

3. SMA constitutive model, and

4. phase kinetics (transformation) model.

These sub-models need to be interconnected as illustrated in Fig. 3.37.

The phase kinetics of an SMA wire, as discussed in Section 3.6, can be modeled for martensite to austenite and austenite to martensite, respectively as:

$$\begin{aligned} \xi &= \frac{\xi_M}{2}\{\cos[a_A(T - A_s) + b_A\sigma] + 1\} \\ \xi &= \frac{1 - \xi_A}{2}\cos[a_M(T - M_f) + b_M\sigma] + \frac{1 + \xi_A}{2} \end{aligned}$$

where ξ_M and ξ_A are the initial martensite fractions before each phase transformation begins. These two variables are determined by the phase kinetics model and are initialized as:

$$\xi_M = 1 \quad \text{and} \quad \xi_A = 0$$

At each iteration of this sub-model, the derivative of the martensite fraction defines the value of ξ_M and ξ_A as:

$$\begin{aligned} &\text{if} \;\; \dot{\xi}(k) \;\; < \;\; 0 \quad \xi_A = \xi(k) \\ &\text{if} \;\; \dot{\xi}(k) \;\; \geq \;\; 0 \quad \xi_M = \xi(k) \end{aligned} \tag{3.26}$$

where $\xi(k)$ is the value of the martensite fraction calculated in the last step of the iteration. Equation 3.26 shows that the values of these two variables should be updated as the SMA element undergoes phase transformation. It is worth noting that, at each iteration, the SMA element only undergoes the phase transformation in one direction (martensite to austenite or austenite to martensite). Therefore, at each iteration, only one of these two variables (ξ_A or ξ_M) is needed to calculate the martensite fraction.

3.8 Summary

In this chapter, it was shown that the existing phenomenological models are not able to predict the complete behavior of SMA wires. To this end, two systems that are actuated by

the SMA wires, were studied. The first system, an SMA-actuated robotic arm was modeled and the model was verified against experimental results. It was shown using simulations that the existing models for the SMA wires cannot completely predict the behavior of this system. This system will be used in the next chapter to study the control of the SMA actuators. The shortcomings of the SMA models were also investigated experimentally. To this end, an SMA-actuated dead-weight system was studied and it was shown that the behavior of the SMA wire under complex thermomechanical loads is not predicted by the existing SMA models. Furthermore, an enhanced phenomenological model was developed to predict the behavior of SMAs under complex thermomechanical loadings. The effectiveness of the enhanced model was shown both through simulations, using the SMA- actuated robotic arm, and through experiments, which were done on the SMA-actuated dead-weight. Finally, a procedure was outlined for modeling the SMA-actuated systems.

Chapter 4

Control of SMA Actuators

This chapter discusses the control problem of the SMA actuators. For this purpose, we use the SMA-actuated robotic arm that was introduced in Chapter 3. The model of the system (as shown in Fig. 4.1) is used for simulating different angular-position-control algorithms. This chapter starts with an overview of the past control research on SMA actuators in Section 4.1. The chapter continues with describing the control challenge of this system in Section 4.2. Section 4.3 presents different control methods for the robotic arm starting with a PID controller followed by the nonlinear control methods. Variable Structure Control based on the angular position error is introduced in Section 4.4. This nonlinear controller was modified using an Extended Kalman Filter that is presented in Section 4.5. The modified Variable Structure Controller uses the stress and temperature of the SMA wire to improve the position control of the robotic arm (Section 4.6). Section 4.7 presents a stress-based Sliding Mode Controller that also uses the Extended Kalman Filter for estimating the stress of the SMA

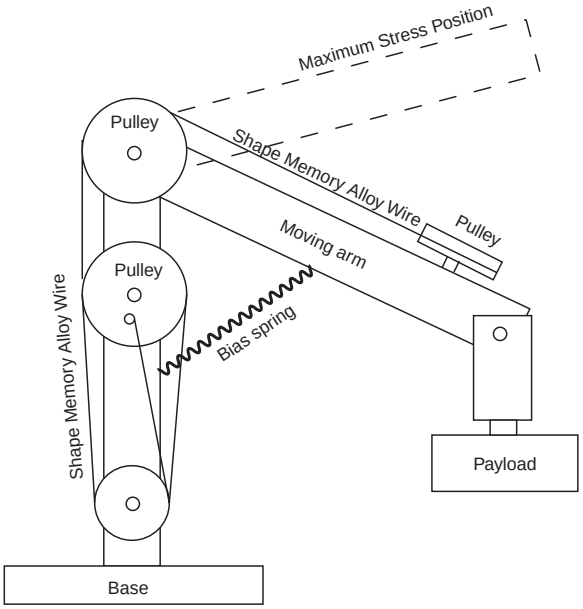

Figure 4.1: The one degree of freedom arm, actuated by SMA NiTi wire, with a bias spring wire. Finally, in Section 4.8, design and stability analysis of a model-based control algorithm is explained.

4.1 Background

There are two types of SMA actuators. One actuator called *bias type* is composed of an SMA element and a bias spring. The other called *differential type* is made of two SMA elements. Many of the designs of actuators using shape memory alloy depend on the mechanical amplification of the displacement either through the use of long straight fibers [26, 27, 28, 29, 30, 31, 32] or through the use of SMA coils [33, 34, 35, 36, 37, 38, 39, 40, 41].

In 1984, Hitachi Co. developed a four-fingered robotic hand that incorporated twelve groups of 0.2mm SMA wires that closed the hand when activated. Dario et. al. [34] proposed

an articulated finger unit using antagonistic SMA coils and a heat pump. Gharaybeh and Burdea [35] used several SMA springs to the Exos Dextrous Hand Master for use as a force feedback controller. Some other notable works in actuator design include the work by Zerkus and Akers [41], who designed a thermoelectric heat pump using Peltier effect to actively cool the SMA. Gorbet and Russell [42] proposed a movable heat sink for a differential pair of fibers that only comes in contact with the cooling fiber.

More recently, Ishii and Ting [43] have designed and analyzed an SMA-actuated compliant bistable mechanism . A compliant bistable mechanism possesses two stable positions in its range of motion. These actuators have several advantages, which include requiring no input to stay at the stable positions, high repeatability in positioning, lightweight and simple control. As an example of SMA actuators for aerospace applications, Sing et al. [44] developed an SMA actuator for rotor blade tracking . The actuator consists of a pair of antagonistic SMA wires and a passive friction brake. It is designed to provide in-flight tracking capability for a helicopter rotor in order to minimize the vibration due to rotor dissimilarities. In the field of optics, Li et al. [45] used an SMA actuator to design a high-aspect-ratio variable-pitch grating device. The SMA actuator moves the miniature-size deformable grating device and therefore changes its diffraction angle. Lim et al. [46] designed an SMA actuator for the slider of the hard disk drives. In regular hard disks the writing head is in contact with the disk surface at the start and stop of the drive. The SMA actuator suspends the slider, which makes the data storage device more durable and opens the door for designing more compact storage devices.

Designing a controller is one of the major steps in the development of SMA actuators. The control research applied to SMA's can be divided into three categories:

1. pulse width modulation,

2. linear control, and

3. nonlinear control.

4.1.1 Pulse Width Modulation Control

A number of researchers have used pulse width modulation (PWM) including Honma et al. [47], Hashimoto et. al. [27], Kuribayashi [28], Tanaka and Yamada [30], and Gharaybeh and Burdea [35].

In 1984, Honma et. al. [47] demonstrated that it is possible to control SMA actuation by electric heating. They used open loop PWM to operate their SMA-actuated robots. Later, Kuribayashi [28] proposed an antagonistic pair of SMA wires for the operation of a rotary joint in 1986. PWM was used in a feedback controller to control both position and force. The controller adjusted the duty cycle between the two antagonistic actuators by switching the applied voltage between the two actuators. Hashimoto et al. [27] proposed a similar rotary joint employing two SMA wires. They applied the actuator to a 6-DOF biped robot and implemented heat sink to improve the response time of the cooling cycle. They validated the operation of the antagonistic actuator arrangement in the dynamic control of an inverted

pendulum. They also introduced a refinement to the PWM switching control by applying the duty cycle to only the driving actuator.

4.1.2 Linear Control

Linear proportional (P) and proportional integral derivative (PID) controls have been applied to SMA actuators by several researchers including Dario et. al. [34], Hirose et al. [48], Ikuta et. al. [37], Reynaerts and van Brussels [29], Tanaka and Yamada [30], Madill [49], Arai et. al. [50], Gorbet and Russell [51], Carpenter et. al. [33], and Singh et al. [44].

Hirose et al. [48] developed a differential type actuator in order to overcome the low energy efficiency and slow response problem of SMAs. The proposed actuator, called ξ-array, is composed of SMA springs which are connected in parallel mechanically and connected in series electrically. Because of electrical connection the overall resistance of the actuator is high. Since the resistance changes with phase transformation, the resistance was used as an indicator of phase transformation and also as a displacement indicator. A PID controller was designed based on resistance measurement of the SMA springs. The actuator was used to position a pair of hanging loads.

Ikuta [37] classified feedback control variables into two categories of external variables (displacement and stress) and internal variables (temperature and electric resistance). He showed that since electric resistance is almost a linear function of the phase transformation (negligible hysteresis), and is also easy to measure, it can be used as a feedback variable. Stiffness of

an SMA spring is also shown to be a linear function of normalized electric resistance. They used two feedback variables to control the motion and force of a gripper. The motion of the finger was controlled by a PID controller with position feedback. For the force control they used a PID control based on the resistance of the SMA springs.

4.1.3 Nonlinear Control

More recently, nonlinear control methods have been employed for SMA-actuated systems. Nakazato et. al. [52] designed a fuzzy logic controller to control the duty cycle of a PMW controller for an SMA actuator with antagonistic wires. Arai et al. [53] used feedback linearization, Choi and Choeung [54] applied variable structure controllers.

Fuzzy logic control has been used for differential type actuators based on position and temperature measurements [52, 55]. Experimental results showed better control performance compared with a PID controller.

van der Wijist et al. [56] presented a control law for an SMA wire actuator consisting of open and closed loop parts. The open loop part takes into account the SMA stress-strain-temperature behavior and the heat transfer model. The constitutive model is used in the open loop part of the controller for calculating the desired SMA wire temperature. Subsequently desired electric power, as the actual input to the system, is calculated. This input is then added to the control input from the closed loop part of the controller, which is a PI-controller. Using simulations they showed the combination of open and closed-loop

control systems perform better than a PI-controller.

Grant and Hayward [57, 58, 59] presented a two-stage variable structure control (VSC) with boundary layer. The VSC consists of a high and a low electric current gain. The layer thickness is chose to be proportional to the actuator's speed [60]. This controller could quench the limit cycle, which is caused by the switching nature of the controller. In this and their other related works, Grant and Hayward chose the parameters of VSC based on experiments.

Pons et al. [61] investigated the two major control problems of SMA actuators: hysteresis and slow cooling response. They implemented three different control approaches on a test setup. It was shown that better overshoot avoidance and faster response can be achieved by using resistance self-sensing capability of the SMA.

Lim et al. [46] applied sliding mode algorithm to control the position of a hard disk head slider actuated by SMA wires. The SMA actuator positions the head at the desired height during the hard disk's starting and stopping processes. Sliding mode control was also used by Han et al. [62] to control the position of a single-link SMA-actuated system. The controller was experimentally tested for tracking various end-point position trajectories.

4.2 Control Challenge

It is worth noting that almost exclusively all control systems applied to SMA actuators are not model-based control algorithms. In other words, the control system is designed based on

the intuitive knowledge of the system, through a combination of simulations and experiments. Therefore, the parameters of the controller are not derived based on the system's parameters. As a result, stability analysis, a major step in designing control systems, has rarely been done for SMA-actuated systems.

It is also important to recognize the co-dependent relationship between stress, martensite fraction, and transformation temperatures of the SMA materials. This complex nonlinear relationship causes many difficulties with regards to control system design for SMA actuators. It is also worth noting that SMAs are one way actuators and they are sensitive to changes in the ambient temperature. In this work, we have studied the control problem of an SMA-actuated robotic arm. This system is chosen as a representative of a class of SMA actuators with complex thermomechanical loadings. In this and similar systems the phase transformation temperatures change dramatically as a result of the actuation. The controllers designed in this study can be applied to systems with similar as well as systems with simpler thermomechanical loadings.

As previously demonstrated, when the SMA-actuated robotic arm moves beyond the angle of maximum stress the transformation temperatures begin to decrease at a rate proportional to the change in stress. In terms of control design, if the desired position is beyond the maximum stress position, the controller should first apply high enough voltage to reach the maximum stress position. Beyond this position, while the position error is still not zero, the voltage should drop rapidly in order to prevent the wire from undergoing the full transformation (see Fig. 4.2). Consequently, when a control system is based solely on the position error it will

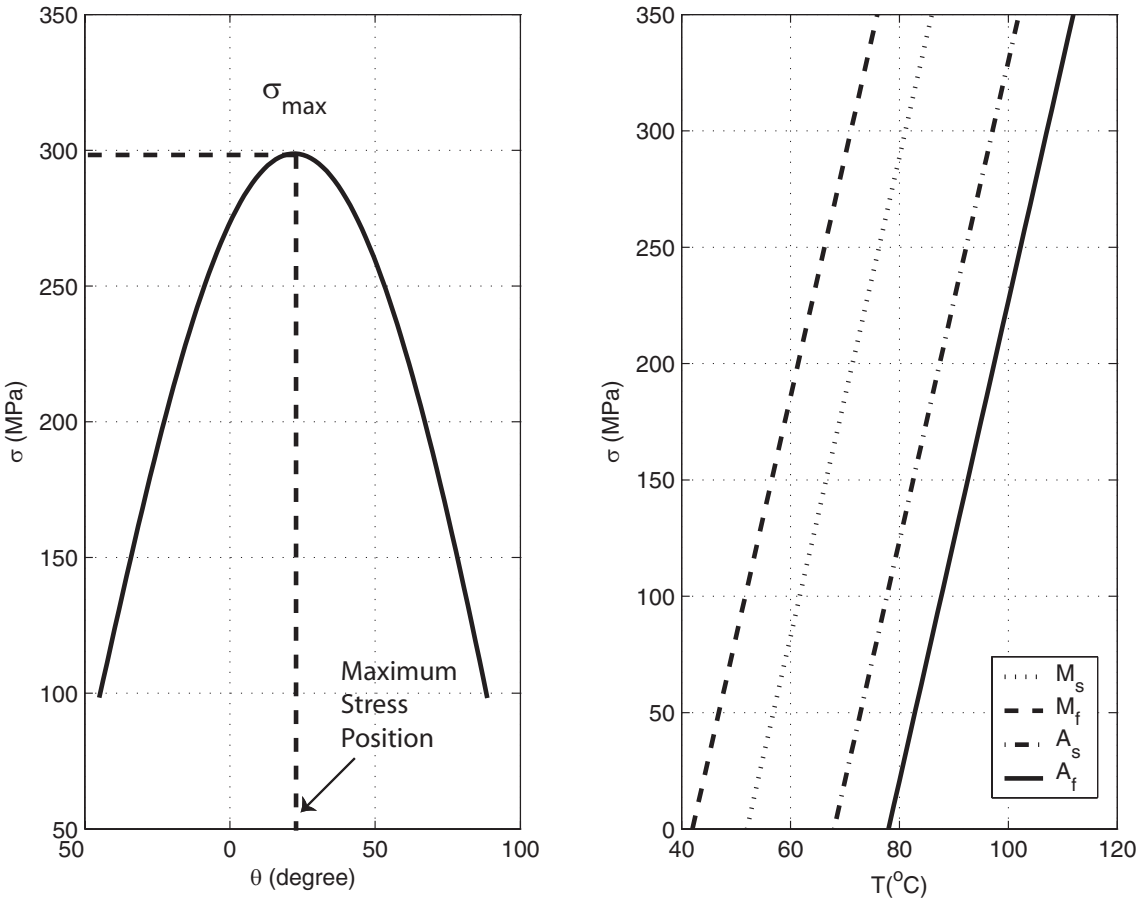

Figure 4.2: When the arm moves beyond the maximum stress position the transformation temperatures decrease, which makes the position control more difficult

apply high voltage to the wire, even when the arm is beyond the maximum- stress-position and the wire will be overheated to the point of full transformation. Although it is possible to tune such a position-based controller to work well for certain positions, it can not work well for all set points.

4.3 PID control

Due to the nonlinearity of both system (robotic arm) and actuator (SMA wire) it is not expected that a PID controller can demonstrate an acceptable control performance. However, we have designed PID controllers through simulations to highlight the inadequacy of the linear controller for controlling the SMA-actuated systems with complex thermomechanical loadings. The results achieved with the PID controller are presented in this section.

Figure 4.3 shows the simulation results for three different desired positions. The PID controller is initially designed to stabilize the moving arm at $\theta_d = 10^o$. It can be seen that the closed-loop system has a reach time of 2.5 seconds and has no overshoot for this set point. But the performance of the controller is not as good for other set-points as shown in the Fig. 4.3. Similar results are shown in Fig. 4.4. In this case, the PID controller is tuned to stabilize the system at $\theta_d = 40^o$. For this angle, the system has a reach time of 4 seconds and has no overshoot. As can be seen in the figure, however, the controller's performance is not the same for other desired positions. For other set-points system has both steady-state error and overshoot.

Experimental results show similar trends as shown in Fig. 4.5. In the experiment, the controller gains are tuned for $\theta_d = 0^o$. Again, the closed-loop system performs worse for set-point both below and above zero degrees. While the system shows overshoot only for higher set-points the overall response is slow for all the set-points.

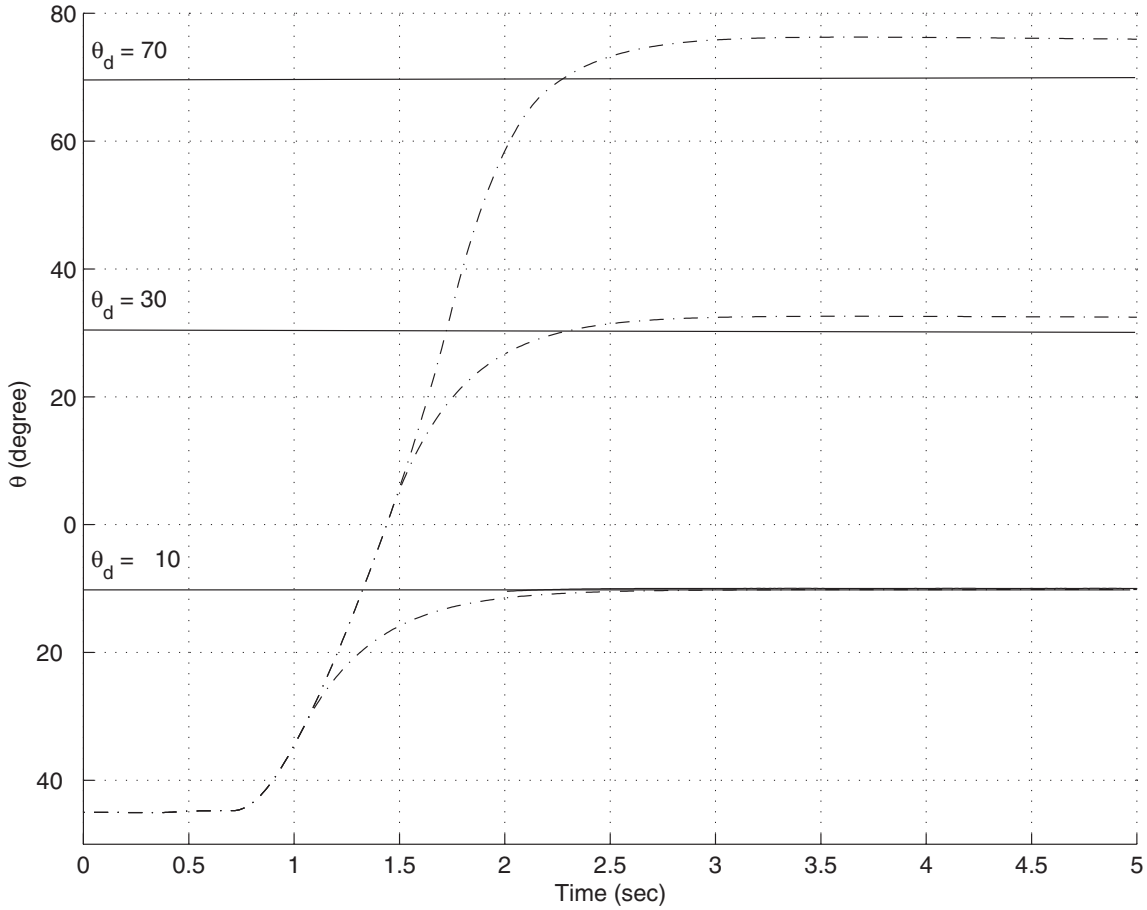

Figure 4.3: Simulation results for the PID controller that is tuned for $\theta_d = 10^o$

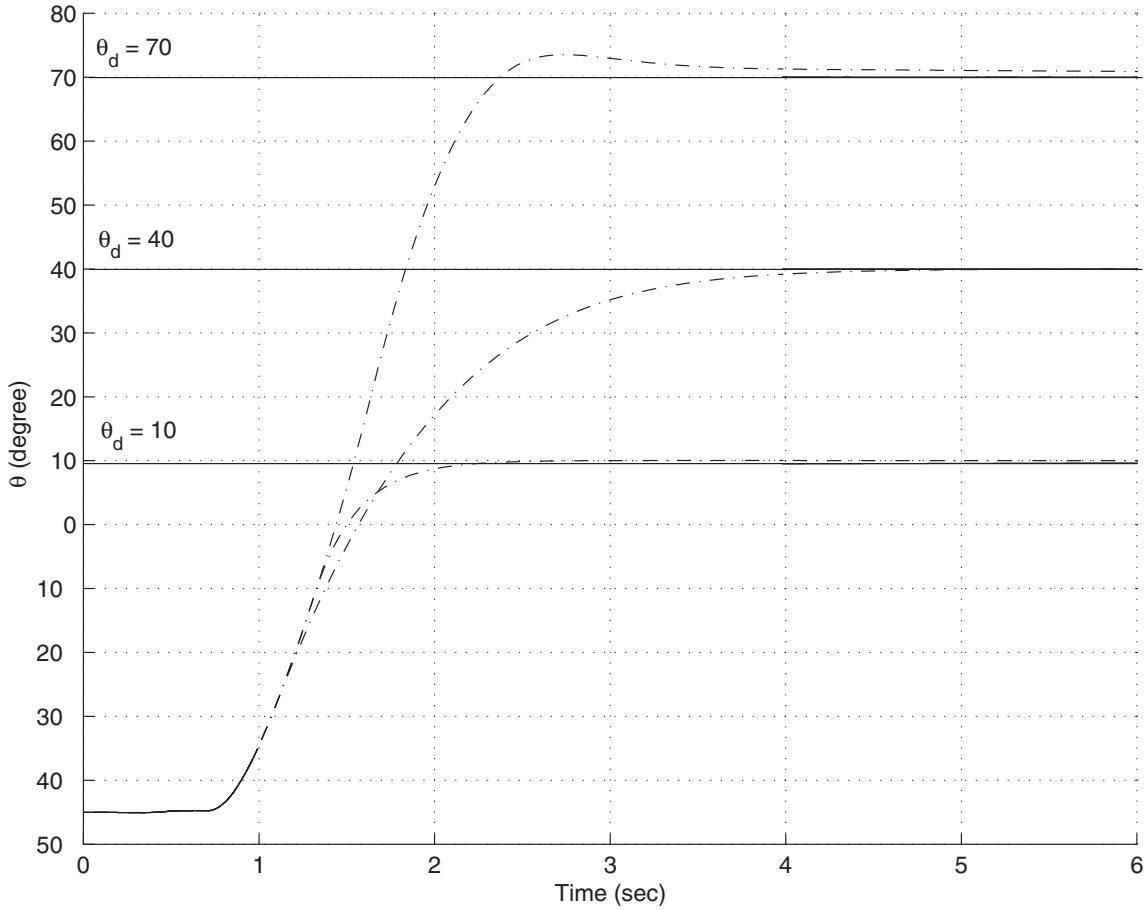

Figure 4.4: Simulation results for the PID controller that is tuned for $\theta_d = 40^o$

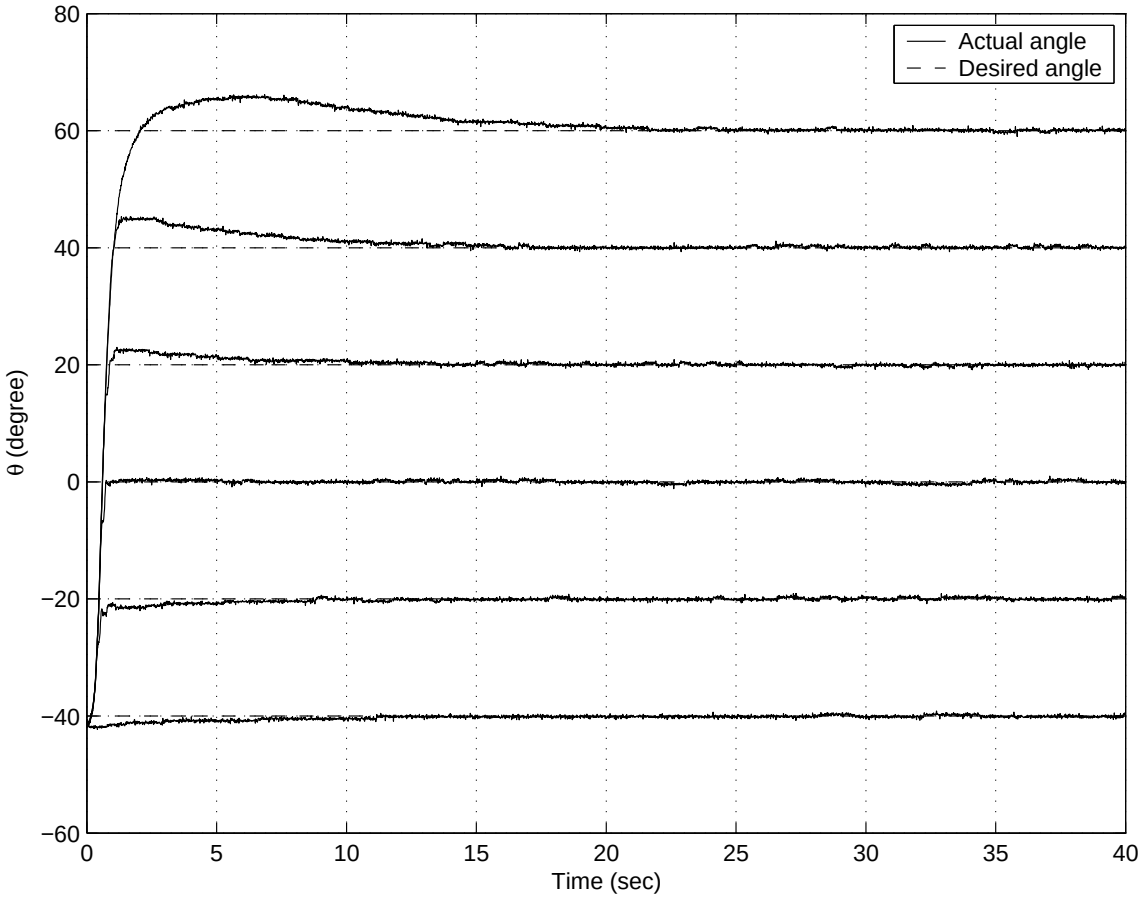

Figure 4.5: Experimental results for the PID controller that is tuned for $\theta_d = 0^o$

4.4 Variable Structure Control

The model presented in Section 3.2 can be represented by a set of nonlinear state equations as

$$\dot{\mathbf{x}} = \mathbf{A}(\mathbf{x}, t) + \mathbf{B}(\mathbf{x}, u, t) \tag{4.1}$$

where the state vector $\mathbf{x}$ and the control input u are given as:

$$\mathbf{x} = [\ \theta \quad \dot{\theta} \quad T \quad \sigma\ ] \qquad \text{and} \qquad u = V \tag{4.2}$$

where state equations are presented by Equations 3.8, 3.1, 3.2, and 3.4 (heating) or 3.6 (cooling), respectively. It is worth noting that some algebraic manipulations are required since Equations 3.2, 3.4 and 3.6 are coupled.

The variable structure control is introduced using the switching function $\mathbf{s}(\mathbf{x})$ as [63]:

$$u(\mathbf{x}, t) = \begin{cases} u^{+}(\mathbf{x}, t) & \text{if } \mathbf{s}(\mathbf{x}) > 0 \\ u^{-}(\mathbf{x}, t) & \text{if } \mathbf{s}(\mathbf{x}) < 0 \end{cases} \tag{4.3}$$

such that $\mathbf{s}(\mathbf{x}) = \mathbf{0}$ (switching surface) can be reached in finite time. The sliding mode takes place on the switching surface, following the desired system dynamics to ensure that the overall VSC system is globally asymptotically stable. Furthermore, a boundary layer around the switching surface can be introduced to avoid chattering which is a common phenomenon in many VSC designs. The subsequent sections describe three VSC designs for the SMA-

actuated arm. The effectiveness of the controllers are compared through both simulations and experiments.

4.4.1 VSC1: Simple Switching

Initially, we designed a two-stage VSC that is a simple switch between a high voltage for quick heating and a low voltage for cooling or reverse motion. The switching is defined based on the position error $s = \widetilde{\theta} = \theta - \theta_d$. Hence, system input is defined as

$$u = \begin{cases} V_{\text{high}} & \text{if } \mathbf{s} < 0 \\ V_{\text{low}} & \text{if } \mathbf{s} > 0 \end{cases} \tag{4.4}$$

4.4.2 VSC2: Simple Switching with Boundary Layer

Next, a boundary layer is introduced around the switching surface $s = \widetilde{\theta}$, to suppress chattering. Denoting the layer thickness as ϕ, the control input is written as:

$$u = \begin{cases} V_{\text{high}} & \text{if} \quad \dfrac{s}{\phi} < -1 \\ V_{\text{low}} & \text{if} \quad \dfrac{s}{\phi} > +1 \\ Ks & \text{if} \quad -1 < \dfrac{s}{\phi} < +1 \end{cases} \tag{4.5}$$

where K is a proportional gain. Generally, increasing the boundary layer thickness, reduces chattering but increases steady-state error.

4.4.3 VSC3: Modified Switching with Boundary Layer

The switching condition (surface) introduced above can be modified using a weighted combination of position and velocity errors:

$$s = (\frac{d}{dt} + \lambda)\widetilde{\theta} = \dot{\widetilde{\theta}} + \lambda\widetilde{\theta} \tag{4.6}$$

In this system, $-\lambda$ is the slope of sliding surface in the phase plane. Although, the angular velocity is not measured experimentally, a numerical derivative approximation is obtained by filtering out the noise.

4.4.4 VSC Results

In the VSC schemes, we chose $V_{\text{high}} = 10V$ according to the hardware restrictions and $V_{\text{low}} = 4V$ based on simulations and experimental trials. Simulation results for the three controllers are shown in Figs. 4.6 and 4.7. The desired position is $\theta_d = 0^o$ with zero angular velocity. The simple switch with no boundary layer controller (VSC1) does not achieve a sliding mode and chattering, shown as limit cycle in the phase plane, persists in the response. The addition of boundary layer to the simple switch (VSC2) eliminates chattering. However, there is still an overshoot problem leading to slow settling of the arm (8 sec) due to cooling.

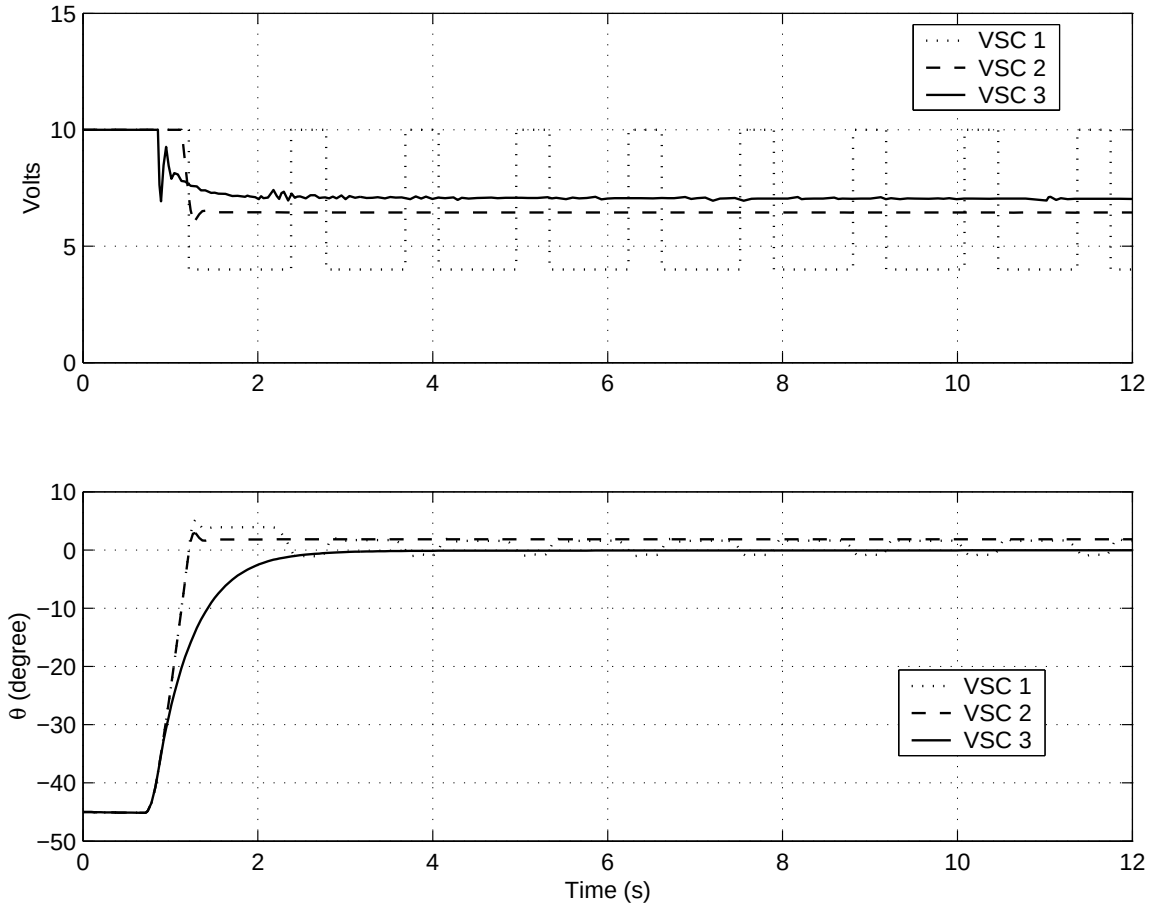

Figure 4.6: Simulation results with simple switch (VSC1), simple switch with boundary layer (VSC2), and modified switch with boundary layer (VSC3) controllers; (top) control input V, (bottom) system output θ

Finally, when the simple switch is modified (VSC3), a sliding mode is achieved and the steady state error is greatly reduced. Also, the system response is much faster (3 sec) since there is no overshoot. Experimental results verify that the modified switch controller with boundary layer is fast and accurate regardless of the desired angular position, as shown in Fig. 4.8. Although the variable structure control methods solve the overshoot problem for all set-points, the steady state error is still a problem that needs further consideration [25].

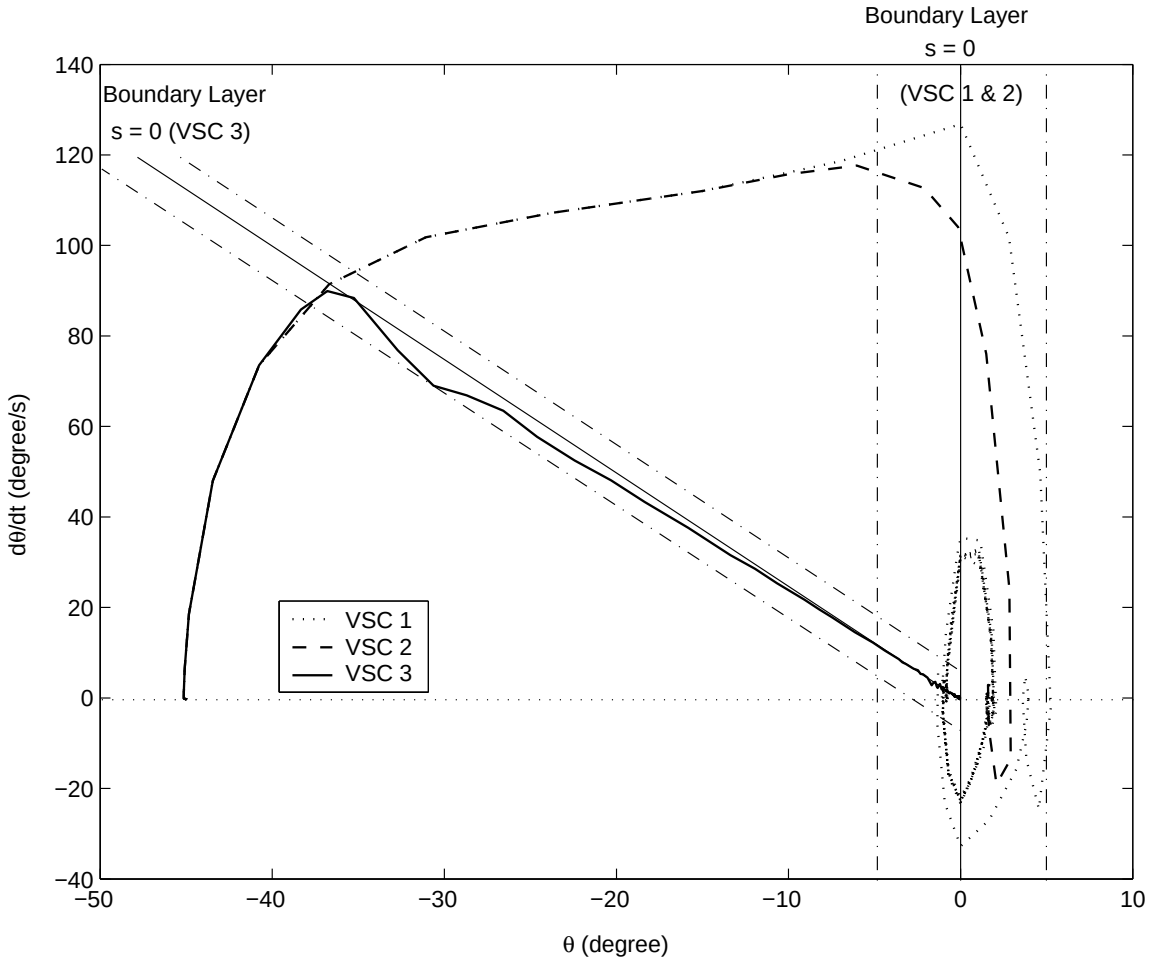

Figure 4.7: Phase plane of simulations with simple switch (VSC1), simple switch with boundary layer (VSC2), and modified switch with boundary layer (VSC3) controllers

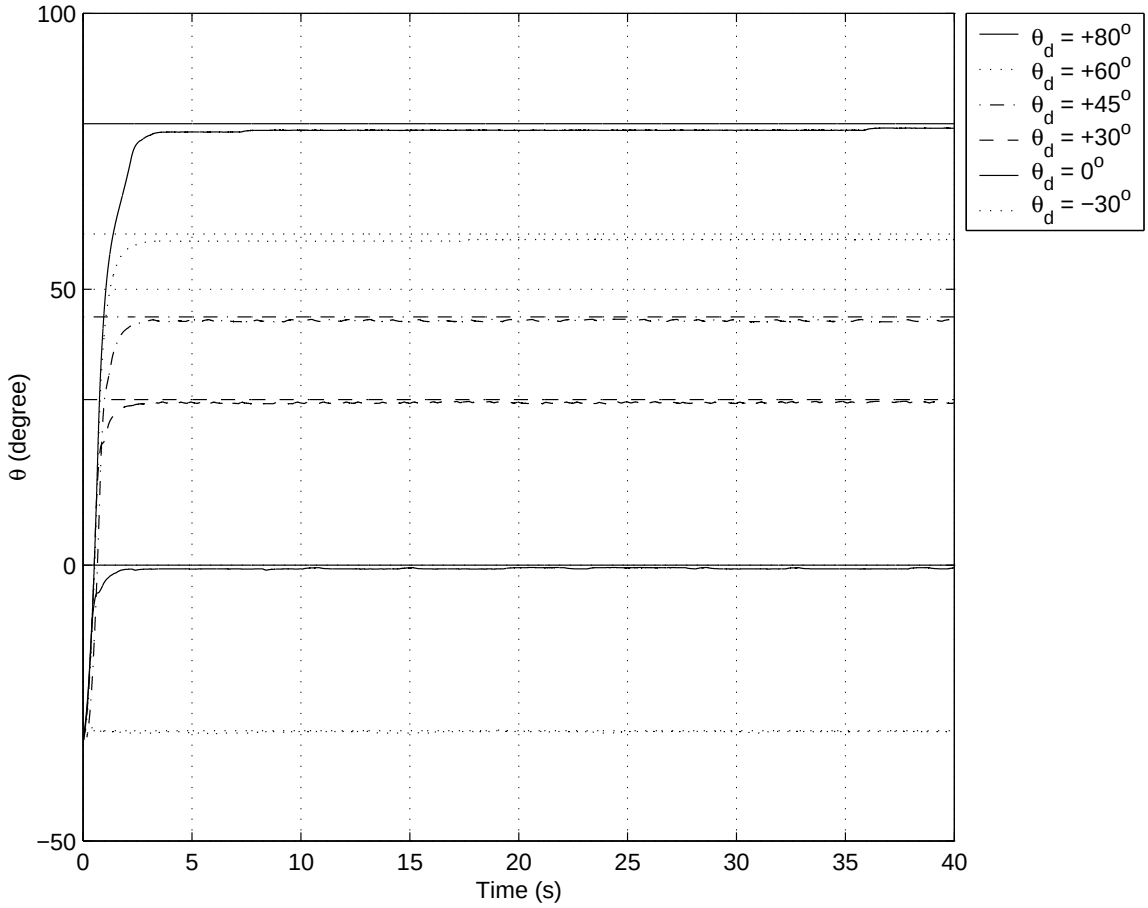

Figure 4.8: Modified switch with boundary layer controller experimental results for different desired angles

4.5 Extended Kalman Filter

Having access to more state variables generally helps improving the performance of control systems. Measuring the state variables of systems actuated by shape memory alloys (SMA) is normally a difficult task. In such cases, as an alternative, observers are used to estimate the state vector. In the experimental setup, the angular position of the arm is the only state variable that is measured. The other state variables of the system are the arm's angular velocity, SMA wire's stress and temperature. These variables are not available experimentally due to difficulty in measuring them. This section presents an Extended Kalman Filter (EKF) for estimation of the state variables of a the SMA rotary actuator [64].

Within the significant toolbox of mathematical tools that can be used for stochastic estimation from noisy sensor measurements, one of the most well-known and often-used tools is what is known as the Kalman Filter [65, 66]. Extended Kalman Filter is the nonlinear version of the Kalman Filter. The filter recursively predicts the state vector by using all or some of the system and sensor dynamics, statistical description of the noise and uncertainties, and initial conditions of the system.

Let's assume that the process has a state vector x $\in R^n$ and a control vector u. The system's dynamic is modeled by a nonlinear stochastic difference equation:

$$\mathbf{x}_k = \mathbf{f}(\mathbf{x}_{k-1}, \mathbf{u}_k, w_{k-1}) \tag{4.7}$$

with the (measurable) output $\mathbf{z} \in R^m$ that could also be a nonlinear function of the state variables:

$$\mathbf{z}_k = \mathbf{h}(\mathbf{x}_k, v_k) \tag{4.8}$$

where the random variables w_k and v_k represent the process and measurement noise, respectively. They are assumed to be independent (of each other), white, and with normal probability distributions with covariance matrices Q and R, i.e.

$$p(w) \sim N(0, Q) \tag{4.9}$$

$$p(v) \sim N(0, R) \tag{4.10}$$

Defining $\hat{\mathbf{x}}_k$ as the a posteriori estimate of the state (from previous time step k) one can approximate the state and measurement vector without the noise effects:

$$\tilde{\mathbf{x}}_k = \mathbf{f}(\hat{\mathbf{x}}_{k-1}, \mathbf{u}_k, 0) \tag{4.11}$$

and

$$\tilde{\mathbf{z}}_k = \mathbf{f}(\tilde{\mathbf{x}}_k, 0) \tag{4.12}$$

The linear governing equations can be obtained by linearizing an estimate about Equations

(4.11) and (4.12)

$$\mathbf{x}_k \approx \tilde{\mathbf{x}}_k + A(\mathbf{x}_{k-1} - \hat{\mathbf{x}}_{k-1}) + W w_{k-1} \tag{4.13}$$

$$\mathbf{z}_k \approx \tilde{\mathbf{z}}_k + H(\mathbf{x}_k - \hat{x}_k) + V v_k \tag{4.14}$$

where $\mathbf{x}_k$ (to be estimated) and $\mathbf{z}_k$ (measured by the sensors) are the actual state and measurement vectors and A, W, H, and V are Jacobian matrices defined at each iteration. Let us define the prediction error:

$$\tilde{\mathbf{e}}_{\mathbf{x}_k} \equiv \mathbf{x}_k - \tilde{\mathbf{x}}_k \tag{4.15}$$

and the measurement residual as:

$$\tilde{\mathbf{e}}_{\mathbf{z}_k} \equiv \mathbf{z}_k - \tilde{\mathbf{z}}_k \tag{4.16}$$

Now we can write the governing equations for an error process as:

$$\tilde{\mathbf{e}}_{\mathbf{x}_k} \approx A(\mathbf{x}_{k-1} - \hat{\mathbf{x}}_{k-1}) + \varepsilon_k \tag{4.17}$$

$$\tilde{\mathbf{e}}_{\mathbf{z}_k} \approx H\tilde{e}_{\mathbf{x}_k} + \eta_k \tag{4.18}$$

where ε_k and η_k present new independent random variables:

$$p(\varepsilon_k) \sim N(0, WQ_kW^T) \tag{4.19}$$

$$p(\eta_k) \sim N(0, VR_kV^T) \tag{4.20}$$

It can be shown that the time update equations of the EKF is:

$$\begin{aligned} \hat{\mathbf{x}}_k^- &= \mathbf{f}(\hat{\mathbf{x}}_{k-1}, \mathbf{u}_k, 0) \\ P_k^- &= A_k P_{k-1} A_k^T + W_k Q_{k-1} W_k^T \end{aligned} \tag{4.21}$$

where $\hat{\mathbf{x}}_k^-$ is the a priori state estimate [66]. These time update equations project the state and covariance estimate (P_k) from the previous time step $k-1$ to the current time step k. And the measurement update equations of the EKF are:

$$\begin{aligned} \mathbf{K}_k &= P_k^- H_k^T (H_k P_k^- H_k^T + V_k R_k V_k^T)^{-1} \\ \hat{\mathbf{x}}_k &= \hat{\mathbf{x}}_k^- + \mathbf{K}_k(\mathbf{z}_k - \mathbf{h}(\hat{\mathbf{x}}_k^-, 0)) \\ P_k &= (I - K_k H_k) P_k^- \end{aligned} \tag{4.22}$$

where $\mathbf{K}$ is the correction gain vector and $\hat{\mathbf{x}}_k$ is the a posteriori estimate. The gain is found in a way to minimize the a posteriori error covariance. These measurement update equations correct the state and covariance estimate using the current measurement $\mathbf{z}_k$. Figure 4.9 shows the schematic of the Extended Kalman Filter for the SMA actuator. The design process of this filter is explained next.

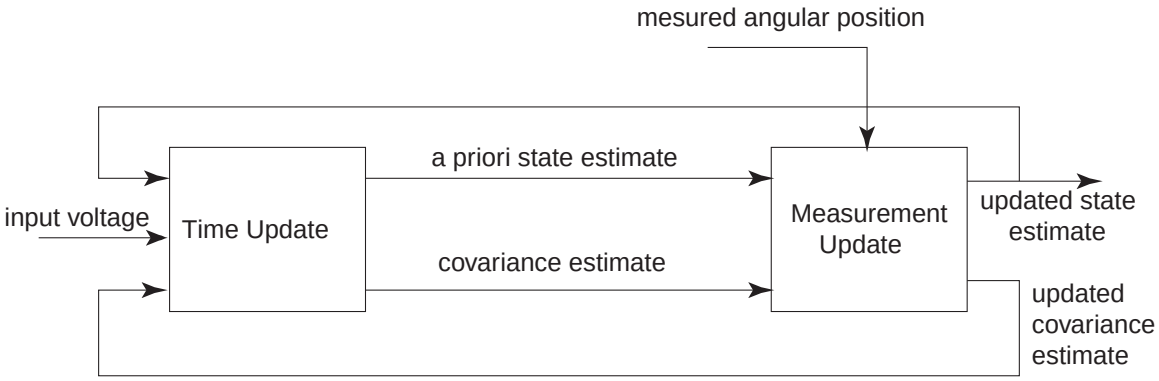

Figure 4.9: The schematic of the Extended Kalman Filter designed to predict the state vector of the SMA-actuated manipulator

4.5.1 EKF for SMA actuator

The SMA manipulator model state vector is defined as:

$$\mathbf{x} = [\theta \quad \dot{\theta} \quad \sigma \quad T] \tag{4.23}$$

The martensite fraction (ξ) is not a state variable since it is a function of the stress and the temperature. The model can be discretized by converting the differential equations presented in the modeling section 3.2 to their corresponding backward difference equations. Angular position of the arm at current time may be predicted using previous values of the angular position and velocity as:

$$\hat{x}_k^-(1) = f_1 = \hat{x}_{k-1}(1) + \hat{x}_{k-1}(2)T_s \tag{4.24}$$

where T_s is the sampling time. The angular velocity is predicted using the previous two angular position samples:

$$\hat{x}_k^-(2) = f_2 = \frac{\hat{x}_{k-1}(1) - \hat{x}_{k-2}(1)}{T_s} \tag{4.25}$$

Therefore, the estimated angular velocity is directly related to the angular position, which is the only measured state variable, instead of integrating the angular acceleration in equation of motion (Equation 3.8). Furthermore, since the SMA wire's stress is a function of strain, temperature, and martensite fraction, using Equation 3.2 to estimate the stress would create a loop. Instead, the stress is estimated using Equation 3.8, which relates the stress directly to the measured angular position:

$$\hat{x}_k^-(3) = f_3 = [I\ddot{\theta} + \tau_{\mathrm{g}}(\hat{x}_k^-(1)) + \tau_{\mathrm{s}}(\hat{x}_k^-(1)) + c\hat{x}_k^-(2))/(2r_{\mathrm{p}}A_{\mathrm{w}}) \tag{4.26}$$

where A_w is the SMA wire's cross-sectional area and r_p is the diameter of the pulley. The angular acceleration of the arm in the above equation is computed using the previous two values of the angular velocity

$$\ddot{\theta} = \frac{\hat{x}_{k-1}(2) - \hat{x}_{k-2}(2)}{T_s} \tag{4.27}$$

Finally, the temperature estimate is simply based on the convection heat transfer Equation

3.1 which depends only on previous temperature value:

$$\hat{x}_k^-(4) = f_4 = \hat{x}_{k-1}(4) + \frac{\mathrm{V}^2/R - h_c A_c(\hat{x}_{k-1}(4) - T_\infty)}{mc_p} T_s \tag{4.28}$$

The Jacobian matrix at each iteration can be derived by using the state Equations 4.24-4.28:

$$A = \begin{bmatrix} 1 & T_s & 0 & 0 \\ \frac{1}{T_s} & 0 & 0 & 0 \\ A_{31} & A_{32} & 0 & 0 \\ 0 & 0 & 0 & A_{44} \end{bmatrix} \tag{4.29}$$

where

$$\begin{aligned} A_{31} &= \frac{\partial f_3}{\partial x_1}(x_k(1), x_k(2), x_{k-1}(2), T_s) \\ A_{32} &= \frac{c}{2r_\mathrm{p} A_\mathrm{w}} \\ A_{44} &= \frac{\partial f_4}{\partial x_4}(x_k(4), T_s) \end{aligned} \tag{4.30}$$

The angular position of the arm is measured, hence

$$\begin{aligned} z_k &= H\mathbf{x}_k + v_k \\ &= [1 \;\; 0 \;\; 0 \;\; 0] x_k + v_k \end{aligned} \tag{4.31}$$

Initially, the SMA wire is prestressed at room temperature and fully martensitic while the arm is at the lower position. Therefore, the initial state vector is

$$\mathbf{x}_{\text{initial}} = [-\frac{\pi}{4}(\text{rad}) \;\; 0(\text{rad/s}) \;\; 98.1(\text{MPa}) \;\; 20(^{o}\text{C})] \tag{4.32}$$

We add uncertainty by selecting the initial state error covariance $P_0 = I_{4\times4}$ and the initial measurement noise covariance $Q = 1e^{-2}I_{4\times4}$. Thus we developed all the necessary elements of the EKF for the SMA rotary actuator. In the next section the results of simulating the filter is presented.

4.5.2 Estimation Results with EKF

An essential phenomenon of SMA wire behavior is hysteresis. This behavior is accurately predicted by the EKF as shown in Fig. 4.10. In this simulation a step input voltage of 8V is applied to the model and the filter. After 3 seconds, the input switches to zero. As the result of this input, after a short delay for reaching the austenite start temperature, the arm moves up. Upon reducing the voltage the arm moves back down again after a short delay due to the time required to cool the wire below the martensite start temperature. The estimation error is small, with the exception of when the arm changes the direction. The sign of the velocity changes when the direction of motion of arm changes and hence the estimation is accompanied with larger errors.

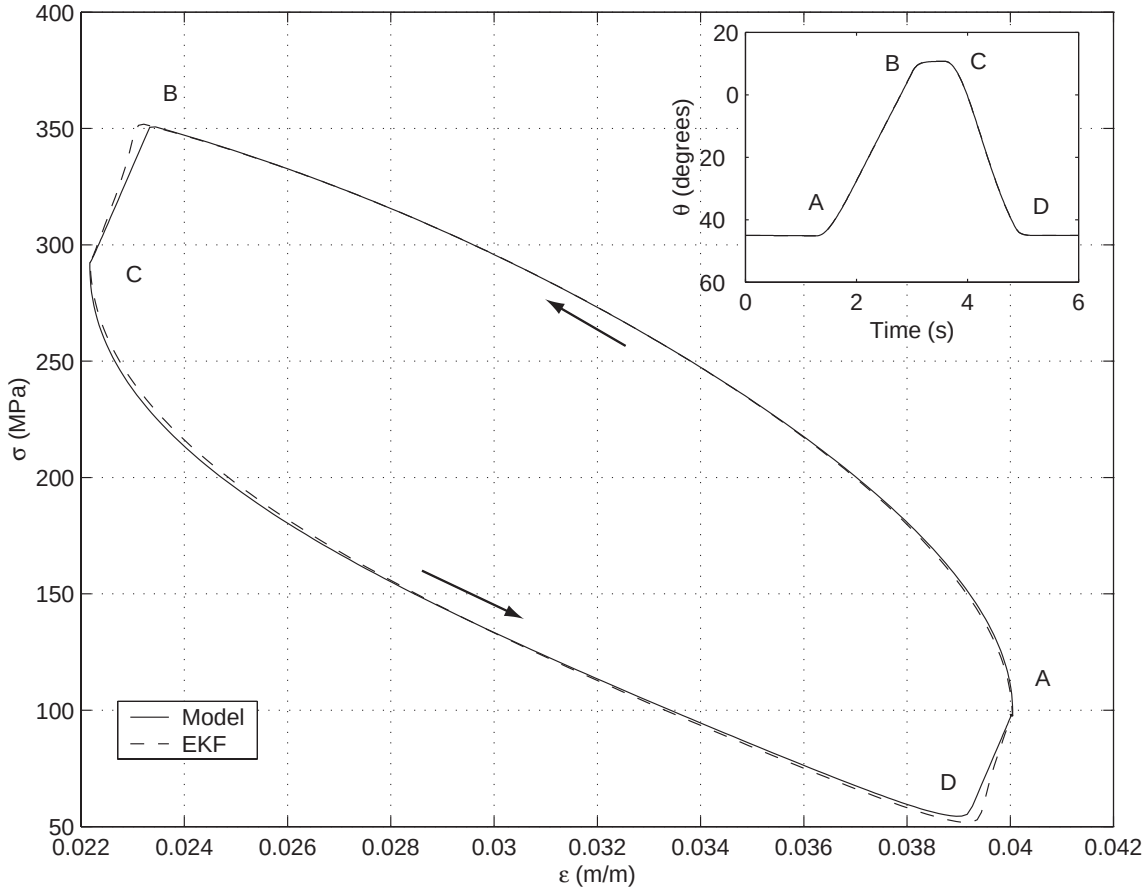

Figure 4.10: Comparison of the simulation and EKF estimated parameters in prediction the hysteretic behavior of SMA

4.6 Temperature-Based VSC

The variable structure control was introduced in Section 4.4 using the switching function $\mathbf{s}(\mathbf{x})$ as:

$$u(\mathbf{x},t) = \begin{cases} u^{+}(\mathbf{x},t) & \text{if } \mathbf{s}(\mathbf{x}) > 0 \\ u^{-}(\mathbf{x},t) & \text{if } \mathbf{s}(\mathbf{x}) < 0 \end{cases}$$

The main switching condition (surface) is a weighted combination of the position and velocity errors,

$$s_1 = (\frac{d}{dt} + \lambda)\widetilde{\theta} = \dot{\widetilde{\theta}} + \lambda\widetilde{\theta} \tag{4.33}$$

where $-\lambda$ is the slope of sliding surface in the phase plane. A boundary layer is introduced around the switching surface s_1, to suppress chattering. Denoting the layer thickness as ϕ, the control input is written as

$$u = \begin{cases} V_{\text{high}} & \text{if} \quad \dfrac{s_1}{\phi} < -1 \\ V_{\text{low}} & \text{if} \quad \dfrac{s_1}{\phi} > +1 \\ Ks_1 & \text{if} \quad -1 < \dfrac{s_1}{\phi} < +1 \end{cases} \tag{4.34}$$

where K is a proportional gain. Generally, increasing the boundary layer thickness, reduces chattering but increases steady-state error. In other words, this controller cannot simulta-

neously solve both overshoot and steady-state error problems.

A faster and more energy efficient control algorithm can be developed by estimating the unmeasured state variables of the systems using the EKF. As shown in Equations (3.3) and (3.5), phase transformation of the SMA wire, from martensite to austenite, depends on both stress and temperature. The reverse phase transformation, which provides upward arm rotation, takes place only when the wire temperature is within the stress-dependent-reverse actuation temperature range (between austenite start, A'_s, and final, A'_f, temperatures):

$$A'_s = A_s + \frac{\sigma}{C_A} \quad \text{and} \quad A'_f = A_f + \frac{\sigma}{C_A} \tag{4.35}$$

An extra structure can be added to the variable structure controller developed in Section 4.4.3 that will be referred to as VSC here. The added structure consists of a new switching condition based on the time derivative of the phase transformation temperatures. The control algorithm remains the same as previous VSC except where the arm is passing through the maximum stress position. The new switching condition is in terms of time derivative of the austenite final temperature:

$$s_2 = \frac{dA'_f}{dt} \tag{4.36}$$

It is worth noting that all the transformation temperatures drop around the angle corresponding to the maximum stress, as shown in Fig. 4.11. The control structure, when the arm gets close to this angular position, switches from the VSC, based on angular position and velocity, to a proportional temperature control in order to maintain the SMA wire tem-

perature within the actuation range. The resulting control algorithm, that is called NVSC, can be written as:

$$u = \begin{cases} \text{VSC output} & \text{if} \quad \frac{s_2}{\phi_T} > 1 \\ K_p(T - T_d) & \text{if} \quad -1 < \frac{s_2}{\phi_T} < 1 \\ \text{VSC output} & \text{if} \quad \frac{s_2}{\phi_T} < -1 \end{cases} \tag{4.37}$$

where T_d is the desired temperature and ϕ_2 is the thickness of the boundary layer around the switching surface s_2. A linear approximation is used to calculate the desired temperature of the SMA wire as a function of desired position, transformation temperatures, and the EKF estimated SMA wire temperature. Figure 4.12 shows the schematic of the control algorithm.

The performance of the temperature-based variable structure controller is compared to the position-based VSC for different desired position of the arm in Fig. 4.13. It can be seen that the overshoot problem is reduce with this controller without compromising either the speed of response or the steady-state position.

The NVSC keeps the SMA wire from overheating as can be seen in Fig. 4.14. While with the VSC the SMA wire heats up to the austenite final temperature and the arm has a larger overshoot, the temperature with the NVSC remains low. Figure 4.15 illustrates the effect of the temperature boundary thickness ϕ_T on the overshoot minimization performance of the new VSC where the desired angular position is kept constant $\theta_d = 50^o$. It can be seen that

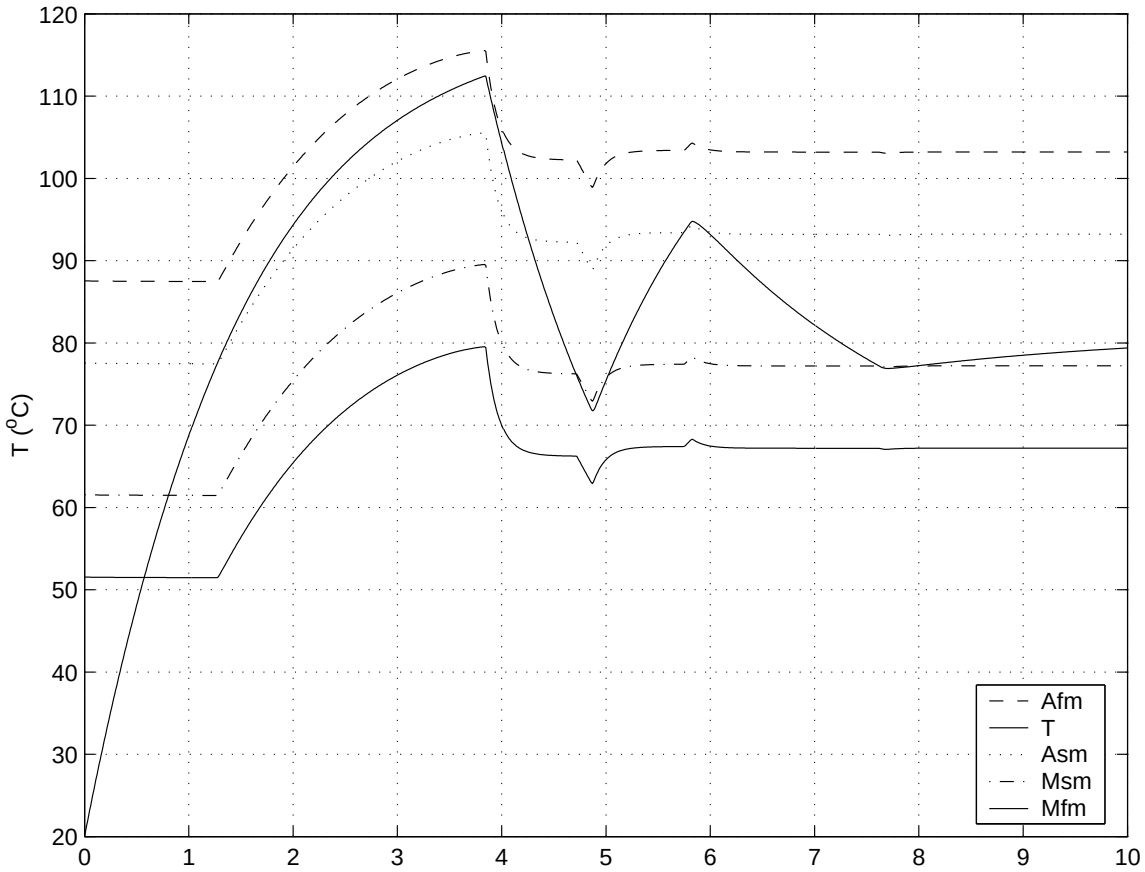

Figure 4.11: The SMA wire phase transformation temperatures drop as the result of the arm passing through the maximum stress angle while the variable structure control is stabilizing the arm at 50^o.

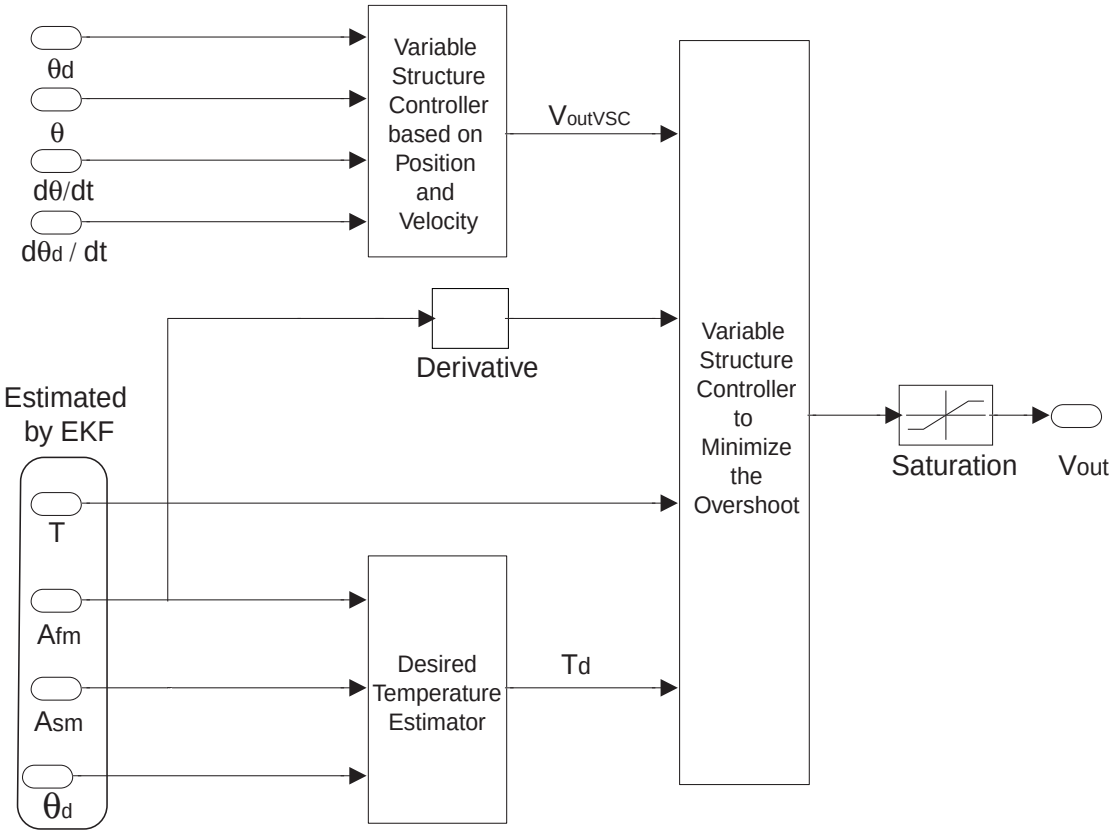

Figure 4.12: The temperature-based variable structure controller (NVSC) switches from position control to temperature control when arm is passing the maximum stress angle.

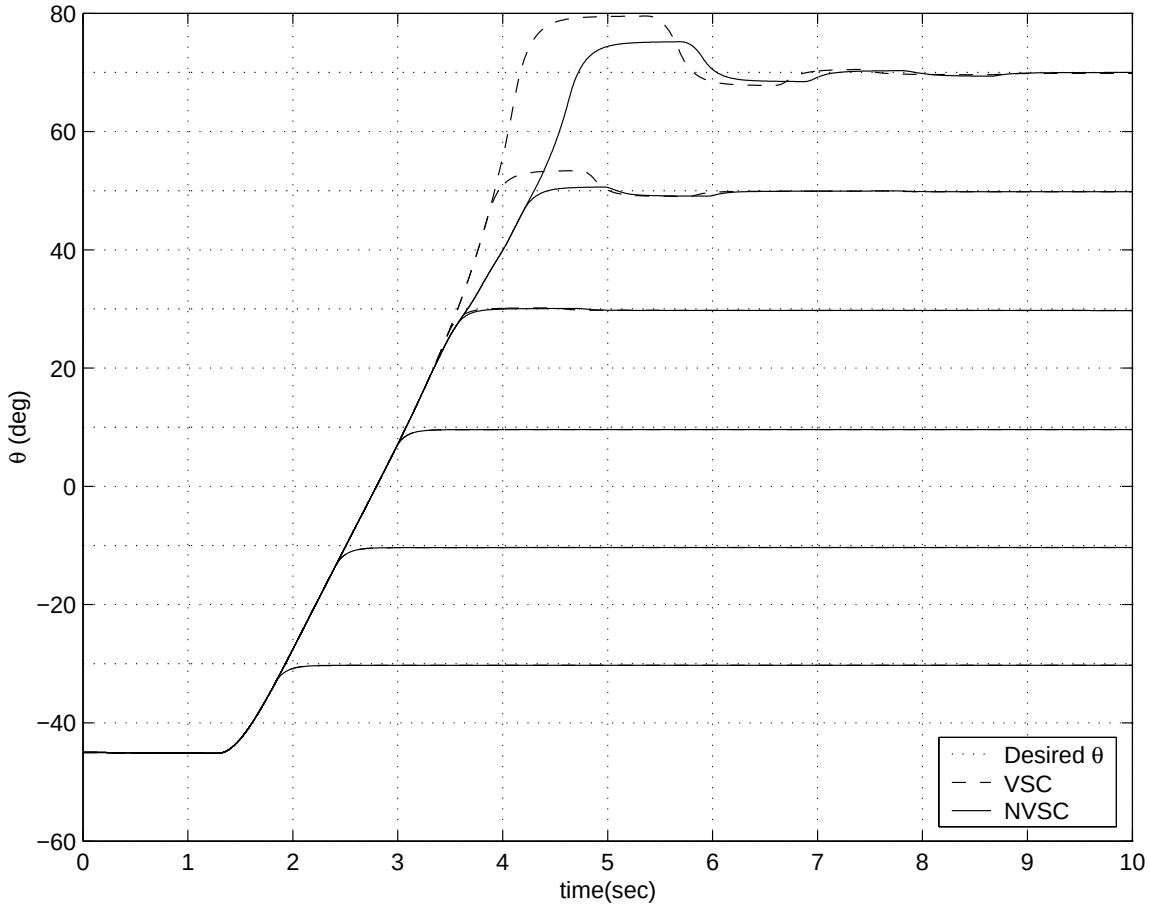

Figure 4.13: Comparing the performance of the temperature-based VSC (based on position and velocity feedbacks and the EKF estimate of temperature and stress) with the performance of the position-based VSC (based on position and velocity feedbacks only)

the overshoot is smaller for the boundary layers with larger thickness. Hence, overshoot can be avoided altogether by increasing the temperature boundary layer.

4.7 Stress-Based Sliding Mode Control

As previously discussed, the transformation temperatures of the SMA wire are stress dependent. This phenomenon adds to the complexity of the position control of the SMA-actuated

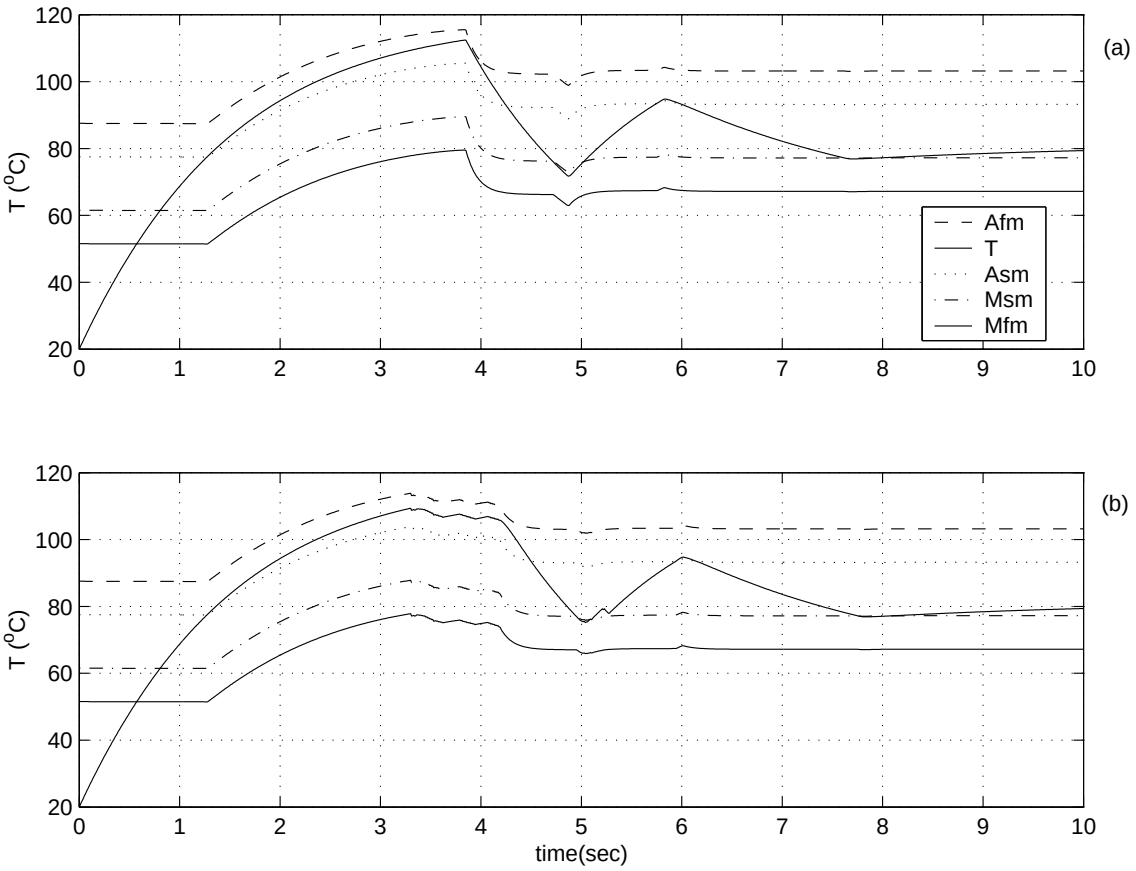

Figure 4.14: The transformations and SMA wire temperatures for (a) position-based VSC (based on position and velocity feedbacks only) and (b) temperature-based VSC (based on position and velocity feedbacks and an EKF estimator); desired angular position $\theta_d = 50^0$

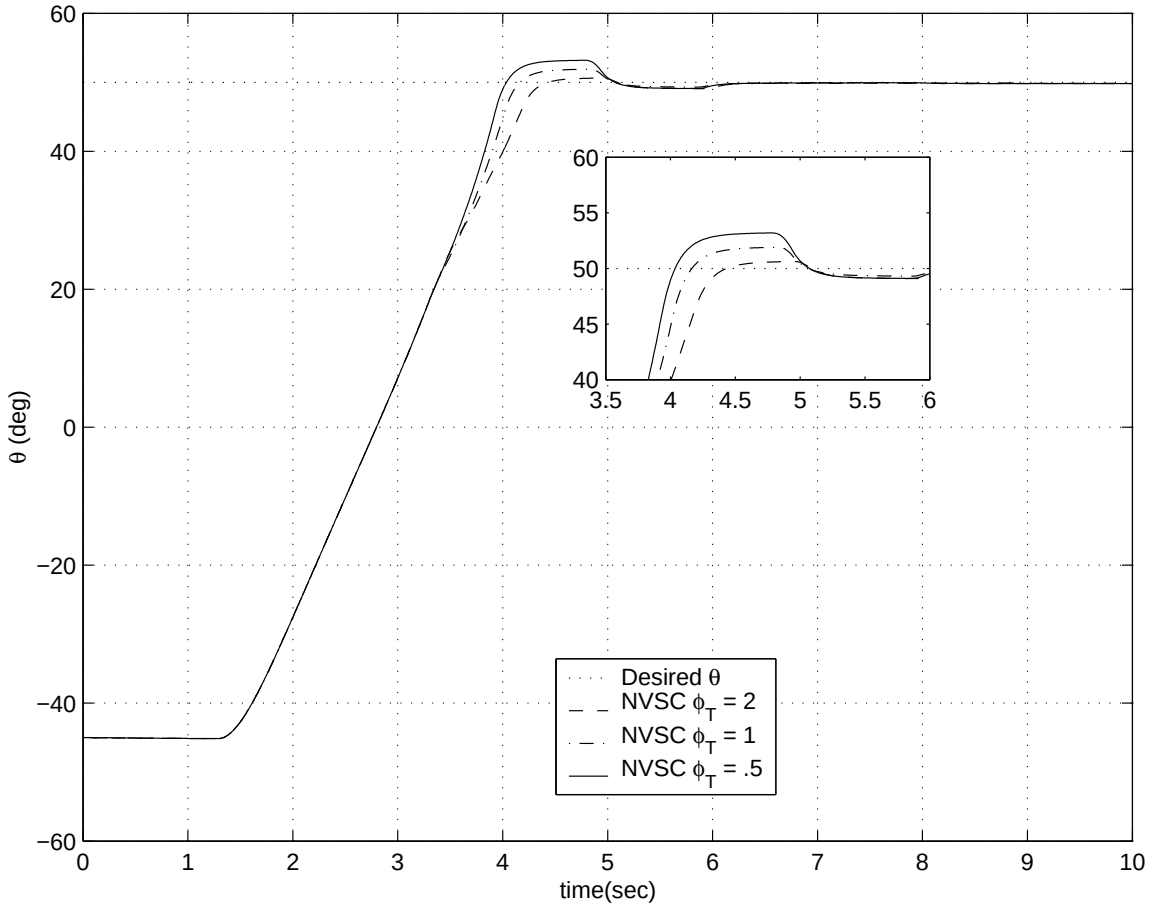

Figure 4.15: The effect of the temperature boundary thickness ϕ_T°C/sec on the overshoot minimization performance of the NVSC, for $\theta_d = 50^0$

arm. To overcome thais problem, in this section, a sliding mode controller is designed to calculate the desired stress of the wire based on the desired angular position of the arm. The stress of the wire is a better set-point for the controller since the transformation temperatures and hence the martensite fraction are functions of the wire's stress. A feedback controller maintains this desired stress by regulating the input voltage to the wire. The controller uses the Extended Kalman Filter (EKF), presented in Section 4.5, to estimate the stress of the SMA wire. The stabilization and tracking performance of this controller is presented and compared with a PID controller.

Sliding control is a robust nonlinear Lyapunov-based control algorithm in which an nth order nonlinear and uncertain system is transformed to a 1st order system. Considering a SISO system

$$x^{(n)} = f(\mathbf{x}) + b(\mathbf{x})u \tag{4.38}$$

where u and x are the scalar input and output, respectively and $\mathbf{x}$ is the state vector. For this system the nonlinear functions f and b are not exactly known. The control objective is for the system to follow a desired state vector $\mathbf{x}_d$. Furthermore, the surface $s(t)$ is defined in the state-space as:

$$s(\mathbf{x}, t) = (\frac{d}{dt} + \lambda)^{n-1}\widetilde{x} \tag{4.39}$$

where $\widetilde{x} = x - x_d$ is the tracking error and λ is a positive constant. It can be shown that tracking the desired state vector is equivalent to that of remaining on the surface $s(t)$ [67]. Therefore the control law should be selected in a way that the distance to this surface

decreases along all system trajectories (sliding condition):

$$\frac{1}{2}\frac{d}{dt}s^2 \leq \eta s \tag{4.40}$$

where η is a positive constant. As the result, all the trajectories are forced to reach the sliding surface in finite time and stay on the surface for all future times. $s(t)$ is called the sliding surface and the systems behavior once on the surface is called sliding mode ($\dot{s} = 0$). It can be shown, that the reach time from the initial state to the surface is [67]:

$$t_{\text{reach}} \leq s(t = 0)/\eta \tag{4.41}$$

Thus, a typical motion under sliding mode control consists of a reaching phase and a sliding phase. During the sliding phase the motion is confined to the sliding surface. Further details on the sliding mode control can be found in books by Slotine [67] and Khalil [68].

The sliding controller for the SMA rotary actuator is deigned to find the desired stress of the SMA wire. Referring to the equation of motion (Equation 3.8), the sliding surface can be defined as:

$$s = (\frac{d}{dt} + \lambda)\widetilde{\theta} \tag{4.42}$$

where $\widetilde{\theta} = \theta_d - \theta$. The dynamic of the system once on the sliding surface can be written as:

$$\dot{s} = 0 \tag{4.43}$$

This equation describes the dynamics of the system while it is in the sliding mode and can be used to find the desired torque of the wire:

$$\begin{aligned} \dot{s} &= \ddot{\theta} - \ddot{\theta}_d + \lambda\dot{\tilde{\theta}} = (\tau_{\mathrm{w}} - \tau_{\mathrm{g}} - \tau_{\mathrm{s}} - c\dot{\theta})/I - \ddot{\theta}_d + \lambda\dot{\tilde{\theta}} = 0 \\ \tau_{\mathrm{w}} &= \tau_{\mathrm{g}} + \tau_{\mathrm{s}} + c\dot{\theta} + I\ddot{\theta}_d - I\lambda\dot{\tilde{\theta}} + K\mathrm{sat}(s) \end{aligned} \tag{4.44}$$

where K is the control gain and the saturation term is added to the desired torque of the SMA wire to address the uncertainties in the model. Also, for the case that the initial state of the system is not on the sliding surface, force the trajectories to merge to the sliding surface. Having the desired torque, the desired stress of the SMA wire can be readily calculated as:

$$\sigma_d = \frac{\tau_{\mathrm{w}}}{2r_{\mathrm{p}}A_{\mathrm{w}}} \tag{4.45}$$

where r_{p} is the radius of the pulley and r_{w} is the cross section area of the SMA wire. In the proposed control design, the sliding mode controller calculates the desired stress of the wire based on the desired position. A second feedback controller, which is a PID controller, maintains the desired stress by applying the required voltage to the wire. Since the controller tracks the desired stress of the wire when the arm reaches the maximum stress position the controller adjust the control input accordingly. Therefore the wire's temperature remain in the actuation range. This control system is shown schematically in Fig. 4.16. As can be seen in the figure the actual stress of the wire is estimated using an Extended Kalman Filter, that was designed in Section 4.5.

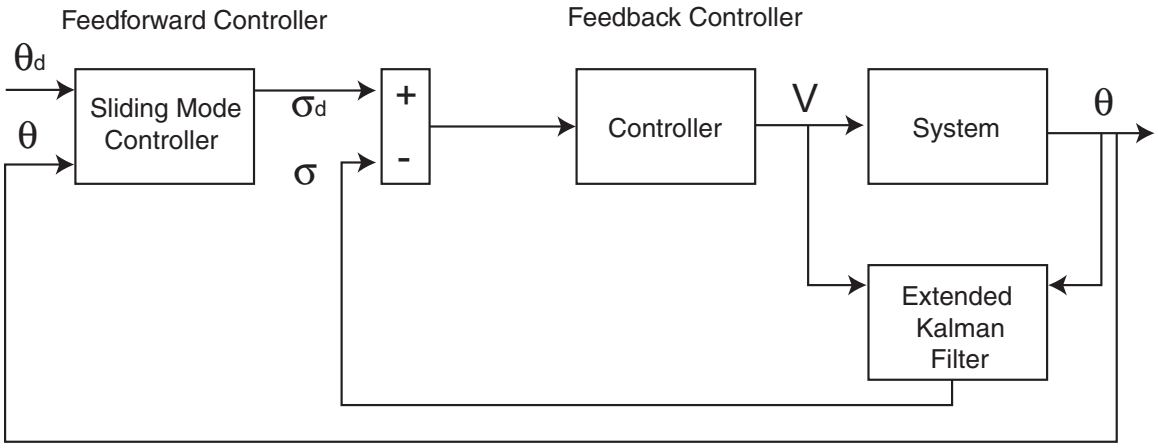

Figure 4.16: The feedforward-feedback controller schematic and the Extended Kalman Filter

The simulation results with the sliding mode controller (SLD) is presented here and compared with a PID controller. Figure 4.17 compares the regulation performance of the proposed controller with that of a PID controller. The PID controller can be tuned to perform well for certain set-points while the same SLD controller works well for all the desired positions. The regulation performance of the SLD controller for several set-points is shown in Fig. 4.18. It can be seen that the arm reaches the desired position for all the set-points in less than 4 sec even though overshoot exists especially for desired positions beyond the maximum stress position. The performance of the controller in tracking the desired stress is shown in the Fig. 4.19. The tracking performance is good and as the result arm reaches the desired angular position.

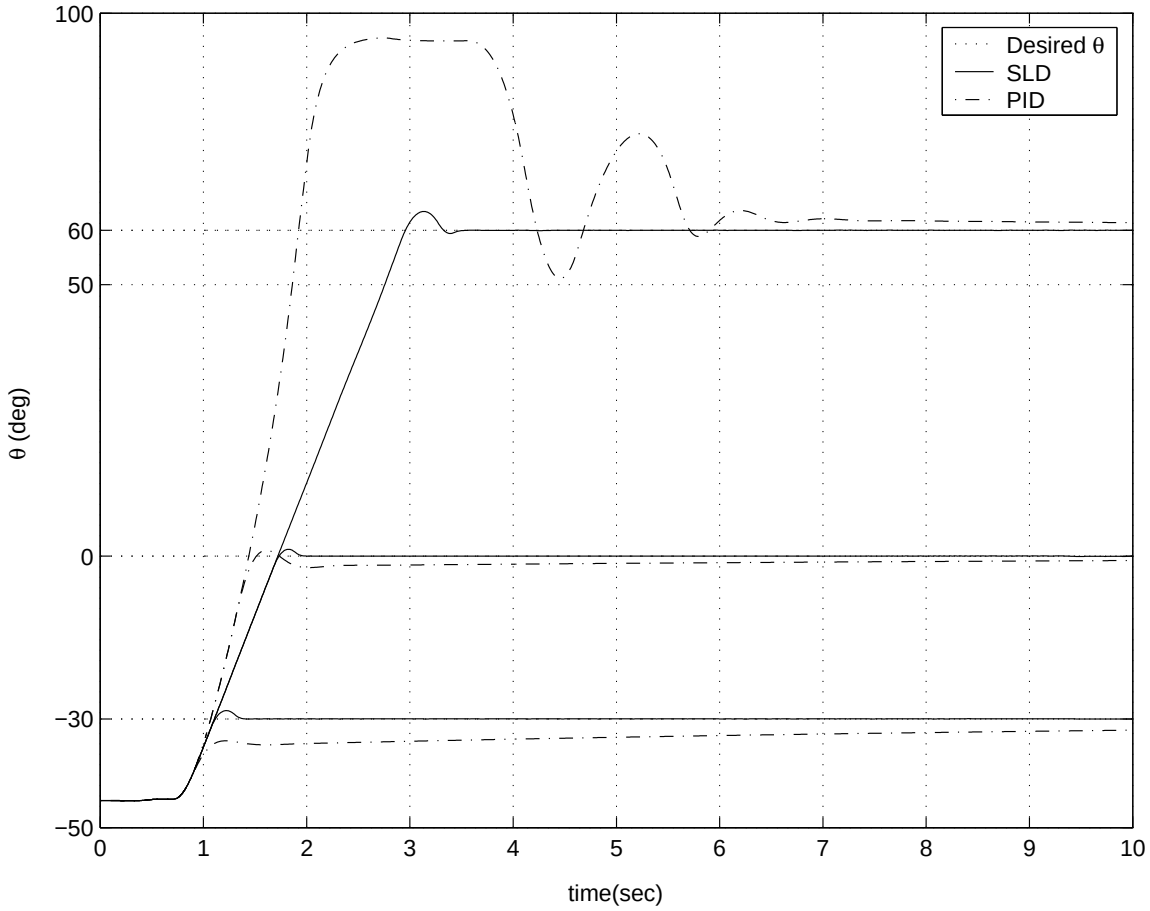

Figure 4.17: Comparing the regulation performance of the feedforward-feedback controller (SLD) with a PID controller

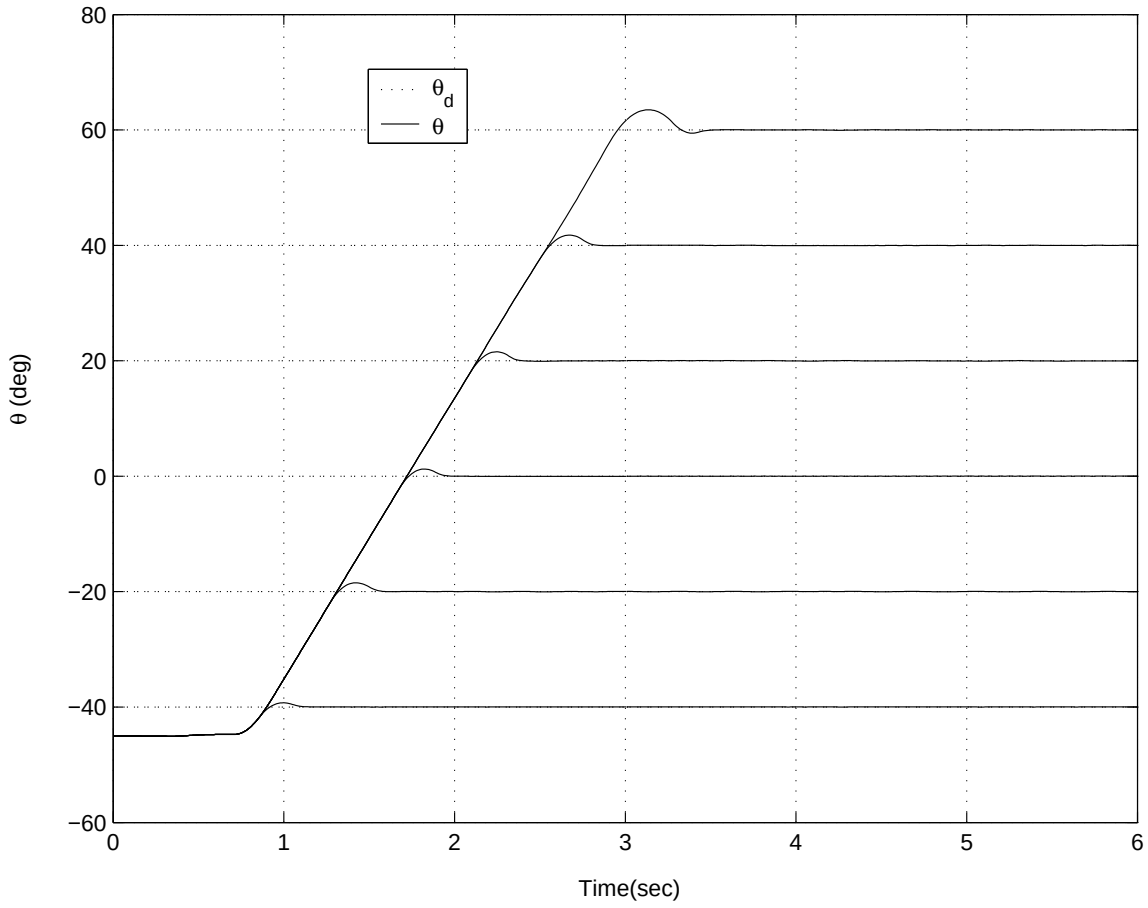

Figure 4.18: The regulation performance of the feedforward-feedback controller (SLD) for desired positions $\theta_d = -40^o$ up to $\theta_d = 60^o$

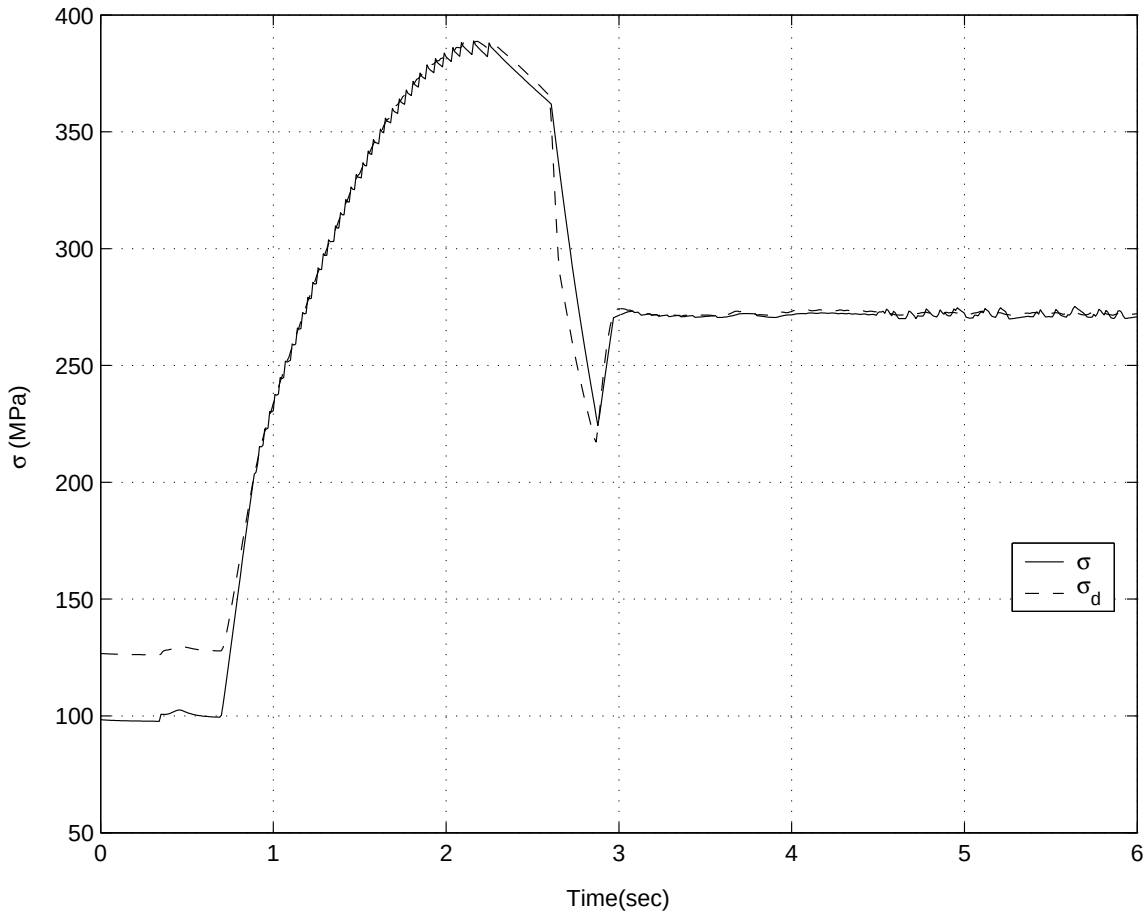

Figure 4.19: The tracking performance of the feedback part of the controller following the desired stress of the wire $\theta_d = 45^o$

4.8 Model-Based Control

Almost exclusively, all control systems applied to SMA actuators are not model-based control algorithms. Therefore, the parameters of the controller are not derived based on the system's parameters. As a result, stability analysis, a major step in designing control systems, has rarely been done for SMA-actuated systems. In this section, a nonlinear model-based controller is designed to globally asymptotically stabilize the single-degree-of-freedom SMA-actuated manipulator. The backstepping control algorithm is used to calculate the applied voltage to the SMA wire. In this algorithm, the SMA wire's stress is assumed to be the control input of the system. The stress is then chosen to asymptotically stabilize the desired position. Applied voltage to the SMA wire is the actual control input. This voltage is calculated based on the desired stress and the SMA's thermomechanical and heat transfer models. It is shown that the calculated voltage can globally asymptotically stabilize the system. Numerical simulations are performed to investigate stabilizing performance as well as other issues such as robustness.

A certain class of single-input control systems can be modeled as:

$$\begin{aligned} \dot{\boldsymbol{\eta}} &= \mathbf{f}(\boldsymbol{\eta}) + \mathbf{g}(\boldsymbol{\eta})\zeta \\ \dot{\zeta} &= u \end{aligned} \tag{4.46}$$

where $\boldsymbol{\eta}(t) \in R^n, \zeta(t) \in R$, and $\mathbf{f}(\mathbf{0}) = \mathbf{0}$. There is a stabilization technique which applies to nonlinear systems with structures similar to Equation 4.46 in which the actual control input

"trickles down" through a series of integrators to the level of a fundamental subsystem. By first designing a stabilizing control law for the fundamental subsystem, one may "backstep" through the integrators to obtain the true control law. The objective in designing a backstepping controller is to stabilize the origin $(\boldsymbol{\eta}, \zeta) = (\mathbf{0}, 0)$. The main assumption is that it is possible to design a stabilizing feedback controller for the $\dot{\boldsymbol{\eta}}$ subsystem by treating ζ as the input. In other words, we assume that by choosing $\zeta = \phi(\boldsymbol{\eta})$, with $\phi(\mathbf{0}) = 0$, the origin of the system:

$$\dot{\boldsymbol{\eta}} = \mathbf{f}(\boldsymbol{\eta}) + \mathbf{g}(\boldsymbol{\eta})\phi(\boldsymbol{\eta}) \tag{4.47}$$

is stabilized. It can be shown that, the origin is asymptotically stable by choosing the control input as [68]:

$$u(\boldsymbol{\eta}, \zeta) = -\frac{\partial V}{\partial \boldsymbol{\eta}}\mathbf{g}(\boldsymbol{\eta}) - k(\zeta - \phi(\boldsymbol{\eta})) + \frac{\partial \phi}{\partial \boldsymbol{\eta}}(\mathbf{f}(\boldsymbol{\eta}) + \mathbf{g}(\boldsymbol{\eta})\zeta) \tag{4.48}$$

where $V(\boldsymbol{\eta})$ is a Lyapunov function proving asymptotical stability for the closed-loop $\dot{\eta}$ subsystem shown in Equation 4.47.

The SMA manipulator, presented in Section 3.2, is a candidate for the backstepping control. While the real control input is the applied voltage to the SMA wire, the SMA wire's stress, is the input for the dynamic subsystem of Equation 3.8:

$$I_{\mathrm{e}}\ddot{\theta} + c\dot{\theta} + [\tau_g(\theta) + \tau_s(\theta)] = \tau_w(\sigma) = \tau_w(\zeta) \tag{4.49}$$

For simplicity, the dynamic equation can be expressed as:

$$I\ddot{\theta} + h(\theta, \dot{\theta}) = \alpha\sigma \tag{4.50}$$

where $h(\theta, \dot{\theta})$ includes viscous damping and the spring and gravitational torques and $\alpha = 2r_{\mathrm{p}}A_{\mathrm{w}}$ is a constant relating the stress to the torque of the SMA wire. The actual control input of the system is the applied voltage to the SMA wire V. It appears in the heat transfer model, formulated as Equation 3.1. The SMA wire's stress is indirectly related to the applied voltage through the thermomechanical model of the wire.

Based on the work of Liang and Rogers [7, 38], the thermomechanical behavior of SMAs can be described in terms of strain (ε), martensite fraction (ξ), and temperature (T). In the simplified form, the thermomechanical constitutive equation is [10]:

$$\sigma = E(\xi)(\varepsilon - \varepsilon_L\xi) \tag{4.51}$$

where $E(\xi)$ is representative of the Young modulus of the SMA material which is defined as linear combination of the martensite Young's modulus E_M and austenite Young's modulus E_A:

$$E = \xi E_M + (1 - \xi)E_A \tag{4.52}$$

The strain of the wire causes the rotation of both the arm and the two pulleys attached to the arm. Therefore the SMA wire strain ε and the angular velocity of the arm θ are related

kinematically as:

$$\varepsilon = -\frac{2r_{\mathrm{p}}(\theta - \theta_0)}{l_0} + \varepsilon_L \tag{4.53}$$

$$\dot{\varepsilon} = -\frac{2r_{\mathrm{p}}\dot{\theta}}{l_0} \tag{4.54}$$

where r_{p} is pulleys radius, l_0 is the initial length of SMA wire, θ_0 is the initial position of the manipulator, and ε_L is the maximum stain of the SMA wire.

In the next two sections, the backstepping method is applied to the SMA-actuated manipulator. Two different approaches are investigated and the more practical approach, in terms of implementation, is chosen for performing the simulations.

4.8.1 Approach I

The equation of motion:

$$I\ddot{\theta} + h(\theta, \dot{\theta}) = \alpha\sigma$$

can be written as two first order differential equations:

$$\begin{aligned} \dot{x_1} &= x_2 \\ \dot{x_2} &= \frac{-h(x_1, x_2)}{I} + \frac{\alpha x_3}{I} \end{aligned} \tag{4.55}$$

where $x_1 = \theta$, $x_2 = \dot{\theta}$ and $x_3 = \sigma$. Assuming that the stress is the control input, the origin of the fundamental dynamic subsystem cab be stabilized. Let's define a Lyapunov function:

$$\begin{aligned} V &= \frac{1}{2}x_1^2 + \frac{1}{2}x_2^2 \\ \dot{V} &= x_1\dot{x}_1 + x_2\dot{x}_2 \\ \dot{V} &= x_1x_2 - \frac{h}{I}x_2 + \frac{\alpha}{I}x_3x_2 \end{aligned} \tag{4.56}$$

by choosing

$$\begin{aligned} x_3 &= \frac{I}{\alpha}(-x_1 + \frac{h}{I} - Kx_2) = \Phi(x_1, x_2) \\ \dot{V} &= -Kx_2^2 \leq 0 \end{aligned} \tag{4.57}$$

where $K > 0$. Therefore $x_3 = \sigma = \Phi(x_1, x_2)$ makes the origin $(\theta = 0, \dot{\theta} = 0)$ stable. By defining a new variable, the closeness of the actual and desired stress can be measured:

$$z_1 = x_3 - \Phi(x_1, x_2) \tag{4.58}$$

We need to change the voltage applied to the SMA wire in a way to maintain the desired stress, which means:

$$z_1 \to 0$$

Taking the time derivative of z_1, we will have:

$$\dot{z}_1 = \dot{x}_3 - \dot{\Phi}(x_1, x_2) \tag{4.59}$$

Now we rewrite the constitutive model, Equation 4.51, in the derivative form:

$$\begin{aligned} \dot{x}_3 &= \dot{x}_4\{(E_M - E_A)\varepsilon_L(1-2x_4) - \frac{2r_\mathrm{p}}{l_0}(x_1 - x_{10})(E_M - E_A) - E_A\varepsilon_L\} \\ &- \frac{2r_\mathrm{p}}{l_0}x_2[(E_M - E_A)x_4 + E_A] \end{aligned} \tag{4.60}$$

where $x_{10} = \theta_0$ and $x_4 = \xi$. We can defining a new variable:

$$\begin{aligned} \Gamma &= (E_M - E_A)\varepsilon_L(1-2x_4) - \frac{2r_\mathrm{p}}{l_0}(x_1 - x_{10})(E_M - E_A) - E_A\varepsilon_L \\ \dot{x}_3 &= \dot{x}_4\Gamma - \frac{2r_\mathrm{p}}{l_0}x_2[(E_M - E_A)x_4 + E_A] \end{aligned} \tag{4.61}$$

By choosing the derivative of the martensite fraction as:

$$\dot{x}_4 = \frac{1}{\Gamma}(u_1 + \dot{\Phi}(x_1, x_2)) + \frac{2r_\mathrm{p}}{l_0}x_2[(E_M - E_A)x_4 + E_A] \tag{4.62}$$

we will have:

$$\dot{z}_1 = u_1 \tag{4.63}$$

The fundamental subsystem (Equation 4.55) is stabilized when $z_1 = 0$. Thus, the problem is to choose the new feedback control law for u_1 to drive z_1 to zero in such a way that η

does not grow large. To ensure the stability, regardless of the way z_1 approaches zero, an augmented Lyapunov function can be defined as:

$$\begin{aligned} V_a &= \frac{1}{2}x_1^2 + \frac{1}{2}x_2^2 + \frac{1}{2}z_1^2 \\ \dot{V}_a &= x_1\dot{x}_1 + x_2\dot{x}_2 + z_1\dot{z}_1 \\ \dot{x}_2 &= -\frac{h}{I} + \frac{\alpha x_3}{I} = -\frac{h}{I} + \frac{\alpha(\Phi + z_1)}{I} \\ \Phi(x_1, x_2) &= \frac{I}{\alpha}(-x_1 + \frac{h}{I} - Kx_2) \\ \dot{V}_a &= x_1x_2 - \frac{h}{I}x_2 - x_1x_2 + \frac{h}{I}x_2 - Kx_2^2 + \frac{\alpha}{I}z_1x_2 + z_1u_1 \\ \dot{V}_a &= -Kx_2^2 + \frac{\alpha}{I}z_1x_2 + z_1u_1 \end{aligned} \tag{4.64}$$

V_a is a Lyapunov function if we choose u_1 as:

$$\begin{aligned} u_1 &= -\frac{\alpha}{I}x_2 - k_1z_1 \\ \dot{V}_a &= -Kx_2^2 - k_1z_1^2 \leq 0 \end{aligned} \tag{4.65}$$

where $k_1 > 0$. Therefore,

$$\dot{x}_4 = \frac{1}{\Gamma}(-\frac{\alpha}{I}x_2 - k_1z_1 + \dot{\Phi}(x_1, x_2)) + \frac{2r_{\mathrm{p}}}{l_0}x_2[(E_M - E_A)x_4 + E_A] \tag{4.66}$$

guarantees the stability of the SMA actuated arm. There is a kinetics relationship between the martensite fraction x_4 and the temperature as defined by Equations 3.3 and 3.5. When the SMA wire is undergoing through the martensite to austenite phase transformation, $\dot{\xi} < 0$,

we have:

$$\begin{aligned} x_5 &= \frac{1}{a_A}\cos^{-1}\frac{2x_4 - x_{40}}{x_{40}} + A_s + \frac{x_3}{C_A} \\ \dot{x}_5 &= \frac{1}{a_A}\frac{-2\dot{x}_4}{\sqrt{1-(\frac{2x_4-x_{40}}{x_{40}})^2}} + \frac{\dot{x}_3}{C_A} \end{aligned} \tag{4.67}$$

where $x_5 = T$ and $x_{40} = \xi_0$. Since x_4 and $\dot{x}_4$ are known, the desired temperature of the wire, x_5 and its derivative can be calculated from Equations 4.67. The required voltage of the SMA wire can then be calculated using the heat transfer model. The heat transfer equation is:

$$U(x_1, x_2, x_3, \dot{x}_3, x_4) = \frac{V^2}{R} = mc_p\dot{x}_5 + h_cA_c(x_5 - x_{50}) \tag{4.68}$$

where x_{50} is the ambient temperature. Since x_5 and therefore $\dot{x}_5$ are known, the control input voltage can be calculated as:

$$V = \sqrt{UR} \tag{4.69}$$

4.8.2 Approach II

While the first approach follows the backstepping design procedure as presented by Khalil [68], it is not the most practical design for the SMA actuator. It needs the measurement and/or estimation of five variables: x_1, x_2, x_3, $\dot{x}_3$, and x_4. Alternatively, we could use the backstepping control design through a different approach, which results in a controller that only needs three state variables to operate. Two of the variables can be measured: (x_1,

x_2), and the other one is estimated: (x_5). Similar to the first approach, the design starts with stabilizing the origin by assuming the stress of the SMA wire is the control input. As previously shown:

$$x_3 = \frac{I}{\alpha}(-x_1 + \frac{h - h_0}{I} - Kx_2) = \Phi(x_1, x_2) \tag{4.70}$$

stabilizes the origin, the term $h_0 = h|_{x_1=0,x_2=0}$ is added to make the calculated stress equal to zero at the origin. Using the constitutive model, as shown in Equation 4.51, we can calculate the martensite fraction $x_4 = \xi$.

$$\begin{aligned} x_3 &= E(\xi)(\varepsilon - \varepsilon_L\xi) \\ &= [x_4(E_M - E_A) + E_A](\frac{-2r_p}{l_0}(x_1 - x_{10}) + \varepsilon_L - x_4\varepsilon_L) \end{aligned} \tag{4.71}$$

From the feedback control law (Equation 4.70, however, we have:

$$x_3 = \frac{I}{\alpha}(-x_1 + \frac{h - h_0}{I} - Kx_2)$$

By equating the stress from the last two equations we will have a quadratic equation is x_4:

$$\begin{aligned} -\varepsilon_L(E_M - E_A)x_4^2 &+ [\frac{-2r_p}{l_0}(x_1 - x_{10})(E_M - E_A) + (E_M - E_A)\varepsilon_L - E_A\varepsilon_L]x_4 \\ -\frac{2r_p}{l_0}(x_1 - x_{10})E_A &+ \varepsilon_L E_A = \frac{I}{\alpha}(-x_1 + \frac{h - h_0}{I} - Kx_2) \end{aligned} \tag{4.72}$$

This second order polynomial equation can be solved for $1 \leq x_4 \leq 0$. The time rate of the martensite fraction, $\dot{x}_4$ can also be calculated. Next, using the appropriate phase

transformation kinetics equation, one can solve for the desired temperature of the wire x_5. When the wire is undergoing the martensite to austenite phase transformation ($\dot{x}_4 < 0$), using Equation 3.3 we can solve for the SMA wire's temperature:

$$x_5 = \cos^{-1}[\frac{2x_4 - \xi_M}{\xi_M}]\frac{1}{a_A} + A_s + \frac{x_3}{C_A} = \Phi_1(x_3, x_4) \tag{4.73}$$

similarly when the wire is undergoing the austenite to martensite phase transformation ($\dot{x}_4 > 0$), using Equation 3.5 we can solve for the wire's temperature:

$$x_5 = \cos^{-1}[\frac{2x_4 - 1 - \xi_A}{1 - \xi_A}]\frac{1}{a_M} + M_f + \frac{x_3}{C_M} = \Phi_1(x_3, x_4) \tag{4.74}$$

Defining the new variable

$$z = x_5 - \Phi_1(x_3, x_4) \tag{4.75}$$

$$\dot{z} = \dot{x}_5 + \frac{1}{a_A}\frac{2\dot{x}_4}{\sqrt{1 - (\frac{2x_4 - x_{40}}{x_{40}})^2}} - \frac{\dot{x}_3}{C_A}$$

$$\begin{aligned} \dot{x}_3 &= \frac{I}{\alpha}(-\dot{x}_1 + \frac{\dot{h}}{I} - K\dot{x}_2) \\ &= \frac{I}{\alpha}\{-x_2 + \frac{\dot{h}}{I} - K[-\frac{h - h_0}{I} + \frac{\alpha}{I}(\frac{I}{\alpha}(-x_1 + \frac{h - h_0}{I} - Kx_2))]\} \\ &= \frac{I}{\alpha}[-x_2 + \frac{\dot{h}}{I} - K(-x_1 - Kx_2)] \end{aligned} \tag{4.76}$$

From the heat transfer model, Equation 3.1 we have:

$$\dot{x}_5 = \frac{U}{mc_p} - \frac{h_c A_c}{mc_p}(x_5 - x_{50}) \tag{4.77}$$

Therefore,

$$\dot{z} = \frac{U}{mc_p} - \frac{hA_c}{mc_p}(x_5 - x_{50}) + \frac{1}{a_A}\frac{2\dot{x}_4}{\sqrt{1-(\frac{2x_4-x_{40}}{x_{40}})^2}} - \frac{\dot{x}_3}{C_A} \tag{4.78}$$

where $U = \frac{V^2}{R}$. We will have

$$\dot{z} = v \tag{4.79}$$

by choosing the control input U, as

$$U = mc_p[v + \frac{hA_c}{mc_p}(x_5 - x_{50}) - \frac{1}{a_A}\frac{2\dot{x}_4}{\sqrt{1-(\frac{2x_4-x_{40}}{x_{40}})^2}} + \frac{\dot{x}_3}{C_A}] \tag{4.80}$$

Therefore, by choosing $v = -K_1 z$, where $K_1 > 0$, we will drive $z \to 0$, which in turn will stabilize the origin. The final control input, therefore, is

$$U(x_1, x_2, x_5) = mc_p[-K_1 z + \frac{hA_c}{mc_p}(x_5 - x_{50}) - \frac{1}{a_A}\frac{2\dot{x}_4}{\sqrt{1-(\frac{2x_4-x_{40}}{x_{40}})^2}} + \frac{\dot{x}_3}{C_A}]$$

And the control voltage is

$$V = \sqrt{UR}$$

It is worth noting that the control input is for martensite to austenite phase transformation

and it will change accordingly if the wire goes through the austenite to martensite phase transformation ($\dot{x}_4 > 0$).

4.8.3 Stability Analysis

Using Lyapunov direct method we showed that the origin is stable. In this section using the Chetaev's method we further investigate the stability of the system. Redefining the Lyapunov function as

$$V(x_1, x_2) = \frac{1}{2} \begin{bmatrix} x_1 \\ \\ x_2 \end{bmatrix} . \begin{bmatrix} 1 & \epsilon \\ \\ \epsilon & 1 \end{bmatrix} \begin{bmatrix} x_1 \\ \\ x_2 \end{bmatrix} \tag{4.81}$$

This function is positive definite if the matrix is positive definite which is true if and only if its principal determinants are positive

$$1 > 0 \quad \text{and} \quad 1 - \epsilon^2 > 0 \tag{4.82}$$

Thus, we must choose $|\epsilon| < 1$. In order to calculate the time derivative of V we need to consider the following:

$$\begin{aligned} V &= \frac{1}{2}x_1^2 + \epsilon x_1 x_2 + \frac{1}{2}x_2^2 \\ \dot{V} &= x_1\dot{x}_1 + x_2\dot{x}_2 + \epsilon(\dot{x}_1 x_2 + x_1\dot{x}_2) \\ \dot{x}_2 &= -\frac{h}{I} + \frac{\alpha}{I}x_3 \\ x_3 &= \frac{I}{\alpha}(-x_1 + \frac{h}{I} - Kx_2) \end{aligned}$$

Thus

$$\dot{V}(x_1, x_2) = \frac{1}{2} \begin{bmatrix} x_1 \\ \\ x_2 \end{bmatrix} . \begin{bmatrix} -K\epsilon & -K\epsilon/2 \\ \\ -K\epsilon/2 & -(K-\epsilon) \end{bmatrix} \begin{bmatrix} x_1 \\ \\ x_2 \end{bmatrix} \tag{4.83}$$

$\dot{V} < 0$ if and only if $-\dot{V} > 0$ which is true if and only if

$$K\epsilon > 0 \quad \text{and} \quad K\epsilon(K-\epsilon) - K^2\epsilon^2/4 > 0 \tag{4.84}$$

In order to find the stable range of K we divide the second condition by $K\epsilon$.

$$K - \epsilon - \frac{K\epsilon}{4} > 0$$
$$K > \frac{\epsilon}{4}(K+4)$$

therefore for $\frac{K}{K+4} > \frac{\epsilon}{4}$ the origin is asymptotically stable.

In order to maintain the stability of the origin while z approaches zero, we define the augmented Lyapunov function as:

$$\begin{aligned} V_a(x_1, x_2) &= \frac{1}{2} \begin{bmatrix} x_1 \\ \\ x_2 \end{bmatrix} . \begin{bmatrix} 1 & \epsilon \\ \\ \epsilon & 1 \end{bmatrix} \begin{bmatrix} x_1 \\ \\ x_2 \end{bmatrix} + \frac{1}{2} z^2 \\ \dot{V}_a &= (\epsilon - K)x_2^2 - \epsilon K x_1 x_2 - \epsilon K x_1^2 + \frac{\alpha}{I} x_2 z_1 + \frac{\alpha}{I} \epsilon x_1 z_1 + z v \end{aligned} \tag{4.85}$$

where z is defined by Equation 4.75. We can cancel x_3 between Equations 4.75 and 4.58 and

find a z_1 az a function of z.

$$z_1 = C_A(x_5 - \cos^{-1}[\frac{2(x_4 - 1)}{\xi_M}]\frac{1}{a_A} - A_s - z) \tag{4.86}$$

Therefore we choose v as:

$$v = -K_1 z + C_A \frac{\alpha}{I}(\epsilon x_1 + x_2) \tag{4.87}$$

which guarantees the asymptotic stability of the origin. It is worth noting that:

$$x_5 - \cos^{-1}[\frac{2x_4 - \xi_M}{\xi_M}]\frac{1}{a_A} - A_s \leq 0 \tag{4.88}$$

therefore these terms are not included in v. It can be easily shown that the for cooling we will have:

$$v = -K_1 z + C_M \frac{\alpha}{I}(\epsilon x_1 + x_2) \tag{4.89}$$

replacing for v in the control input Equation 4.80 will result in a control input that globally asymptotically stabilize the origin $x_1 = 0$ and $x_2 = 0$. It is worth noting that if the calculated voltage for the SMA actuator is negative a zero voltage should be applied.

4.8.4 Simulation Results

This section presents the control simulation results using the second backstepping approach. Figure 4.20 shows the stabilizing performance of the controller. The controller heats the wire which causes the arm to rotate upward, the applied voltage is then decreased which

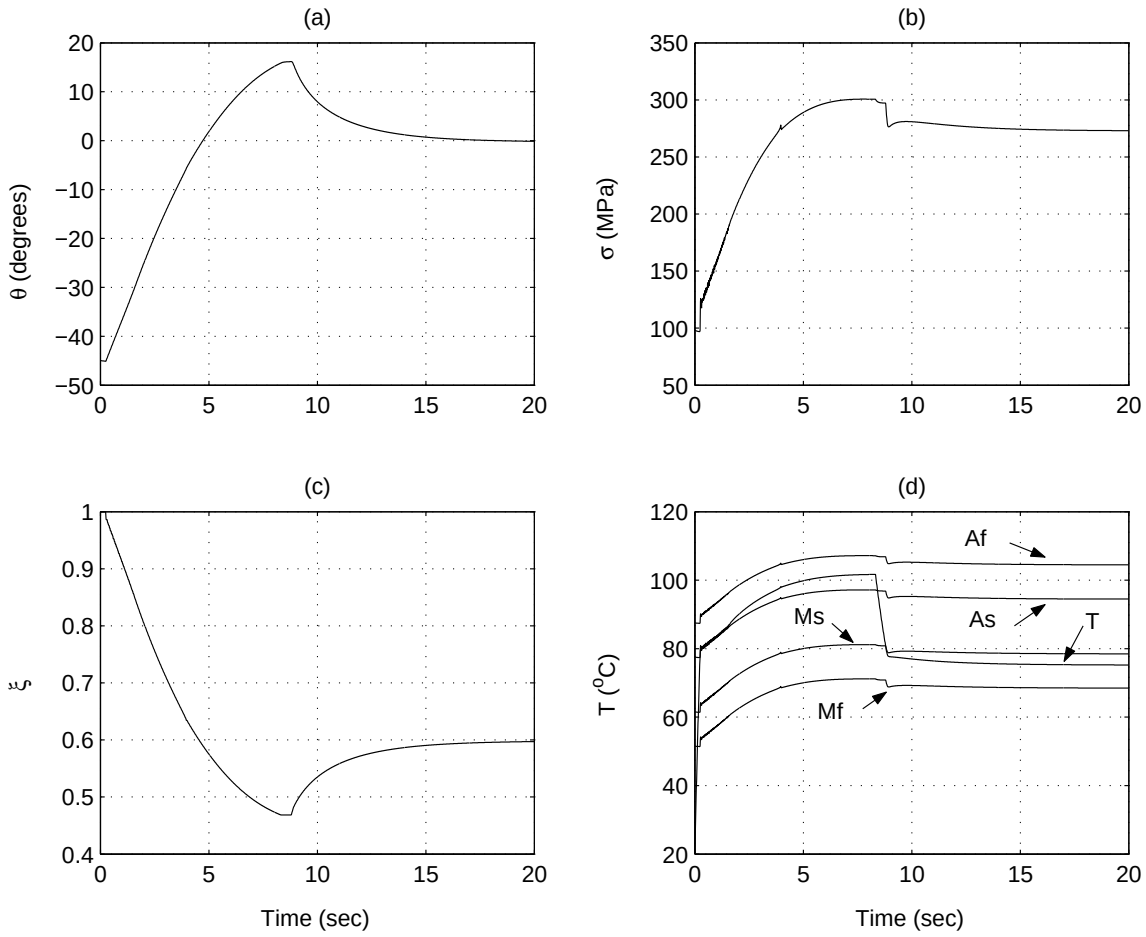

Figure 4.20: Backstepping control simulation results; (a) angular position of the SMA-actuated arm, (b) stress of the SMA wire, (c) martensite fraction of the SMA wire, (d) temperature of the wire and the transformation temperatures

causes the SMA wire to cool down and the arm finally settles at the desired position. The manipulator has overshoot which means the SMA wire has to cool down through natural convection.

The controller's performance is a function of two controller gains K and K_1. The variation of the first gain, that presents the contributes of angular velocity in computing the desired-stress, changes the performance of the closed-loop system. Choosing smaller values for K,

allows the manipulator to gain large angular speed that in turn causes larger overshoots. As this gain moves close to zero the closed-loop system gets unstable. On the other hand, greater K means that the manipulator is slowed down before reaching the desired position. This is shown in Fig. 4.21. The second gain K_1, represents the effect of the temperature error on the control input voltage. Large gain means that the controller emphasizes more on the SMA wire temperature error which can cause the wire to undergo consecutive heating and cooling. Smaller gain on the other hand, means that the temperature error is not weighted enough therefore the SMA wire does not cool enough, which results in large steady state error (see Fig. 4.22).

To investigate the robustness of the controller, we have used different parameter values for calculating the control voltage input than the parameter values used in the model. The effect of moment of inertia is shown in Fig. 4.23. It can be seen that using a value for the moment of inertia that does not match the true moment of inertia, does not significantly degrade the controller's performance. Figure 4.24 shows that the changes in the damping coefficient cr has, on the other hand, a significant affect on the closed-loop response of the system. If the damping coefficient used for calculating the control voltage is lower that the actual damping coefficient the system behaves similar to undamped system while using greater damping coefficient in the controller results in a more damped response.

Finally the effect of the coefficient of convection heat transfer on the performance of the backstepping controller is shown in Fig. 4.25. If the value for h_c used in the controller is smaller that the true value of h_c, the control voltage appears to be smaller than the required

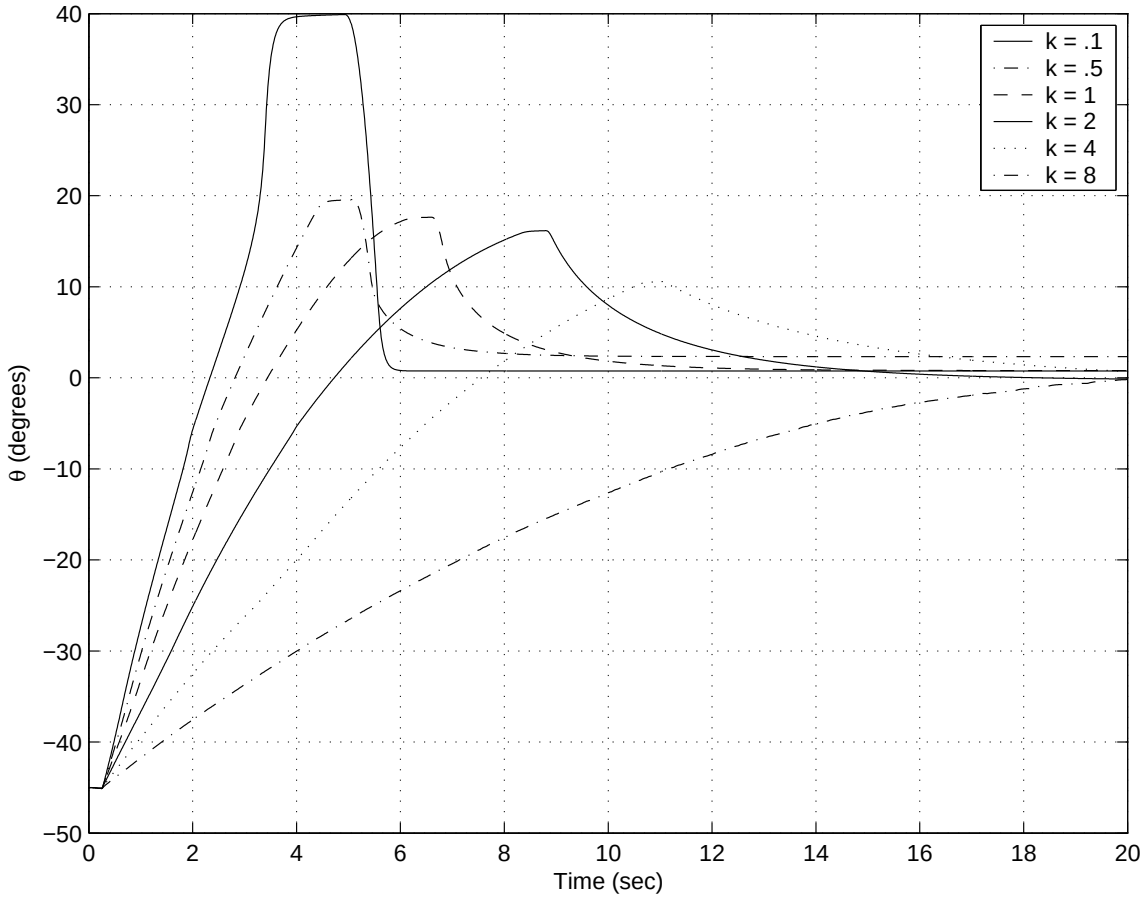

Figure 4.21: Effect of the controller gain K on the performance of the controller

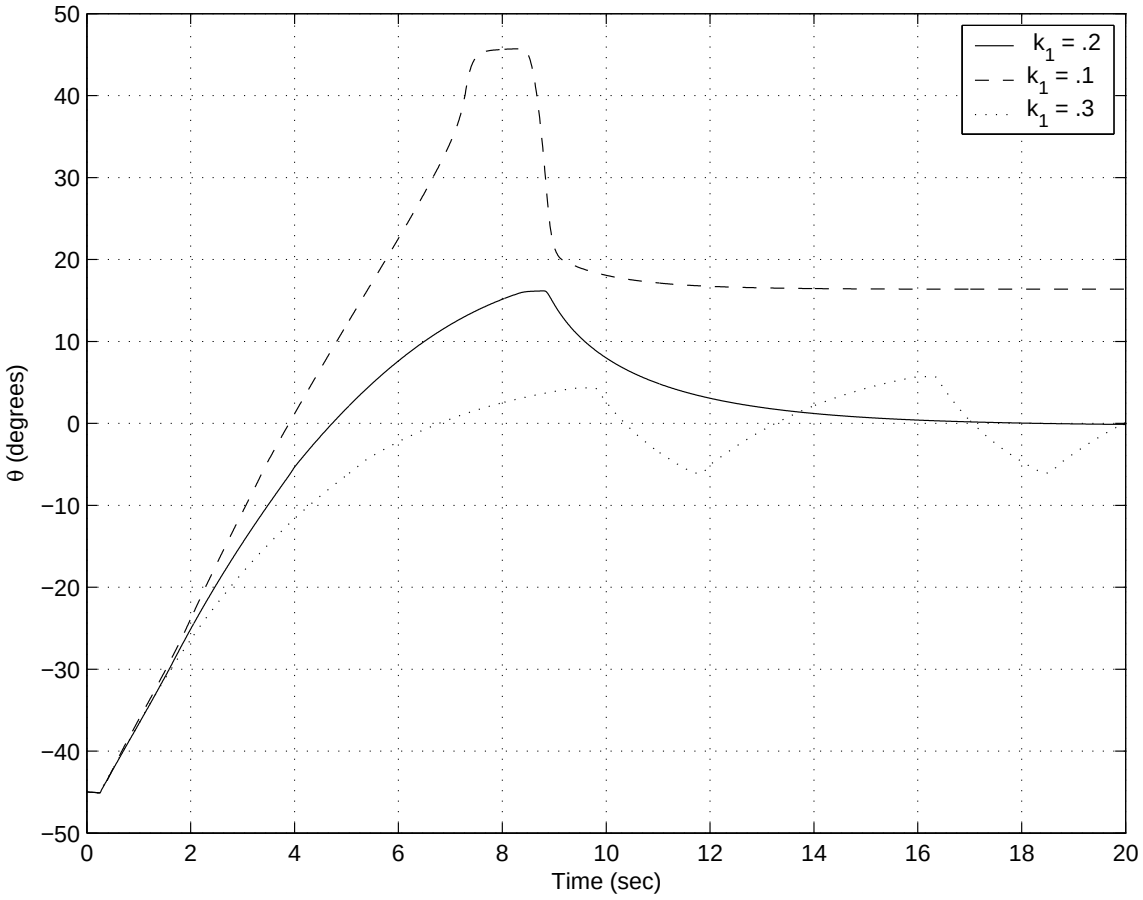

Figure 4.22: Effect of the controller gain K_1 on the performance of the controller

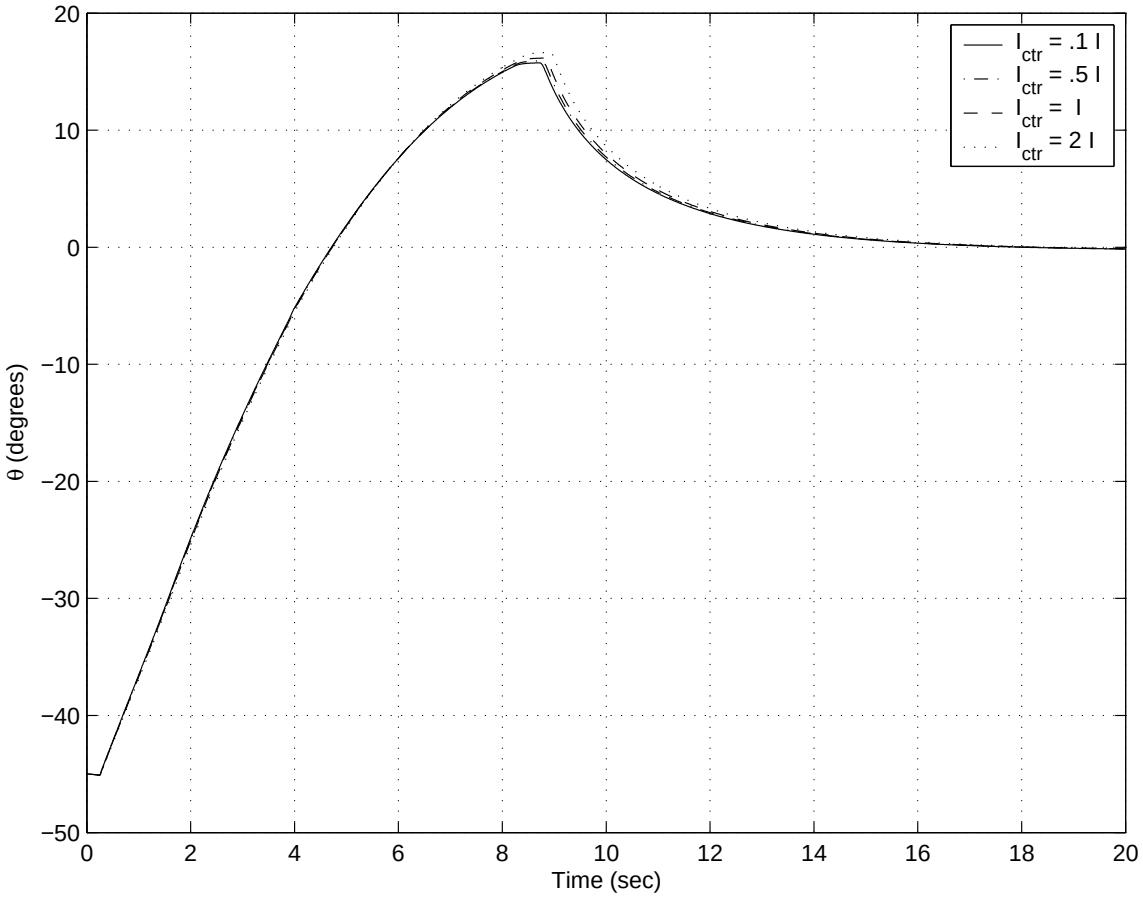

Figure 4.23: Robustness of the backstepping controller, effect of choosing different values for moment of inertia, in the controller and the model

voltage and therefore the manipulator moves less than required. Overestimating h_c, on the other hand, causes the controller to put large voltage into the SMA wire and overheat it which will in turn over-actuate the manipulator.

It is worth noting that the disturbances could have similar effect as over or underestimating the parameters of the system. As an example, changing the ambient temperature essentially changes the natural convection heat transfer coefficient. Therefore, the changes in the ambient temperature have similar effect on the performance of the closed-loop system.

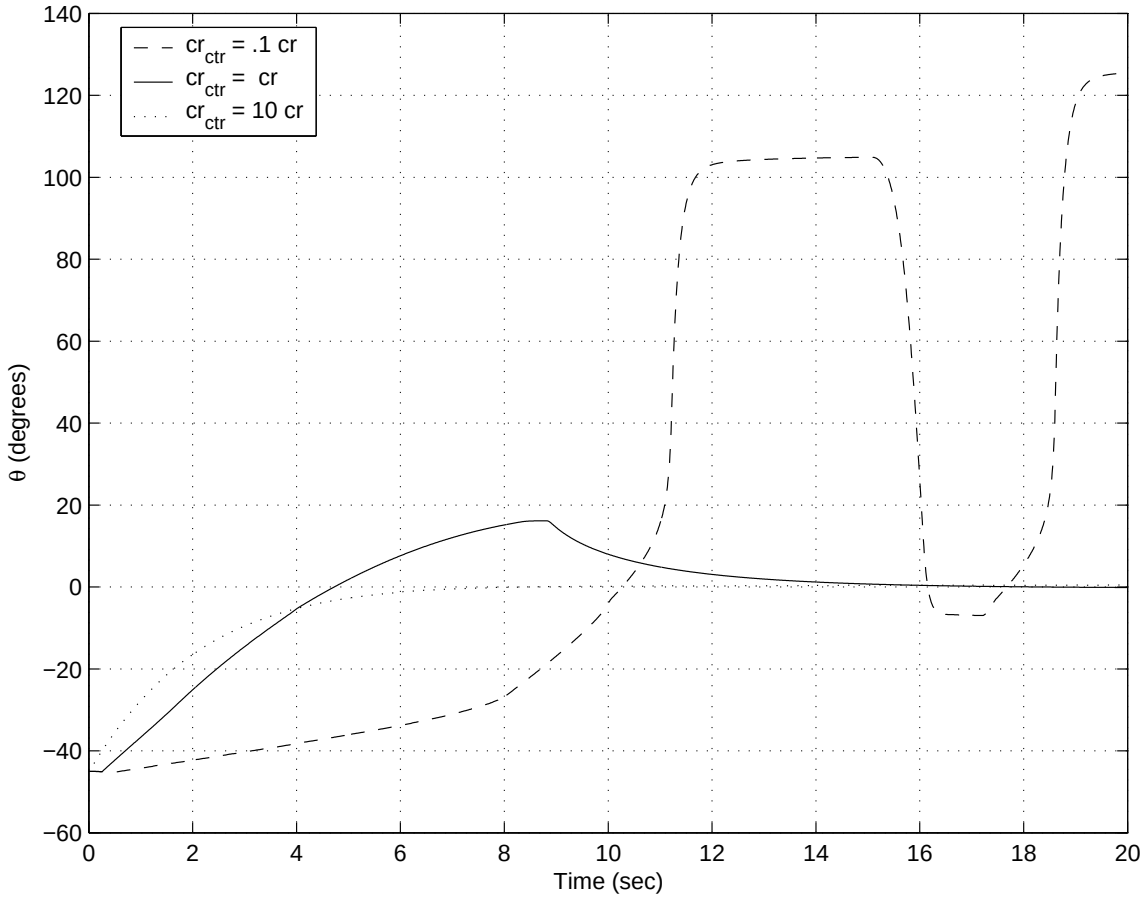

Figure 4.24: Robustness of the backstepping controller, effect of choosing different values for damping coefficient, in the controller and the model

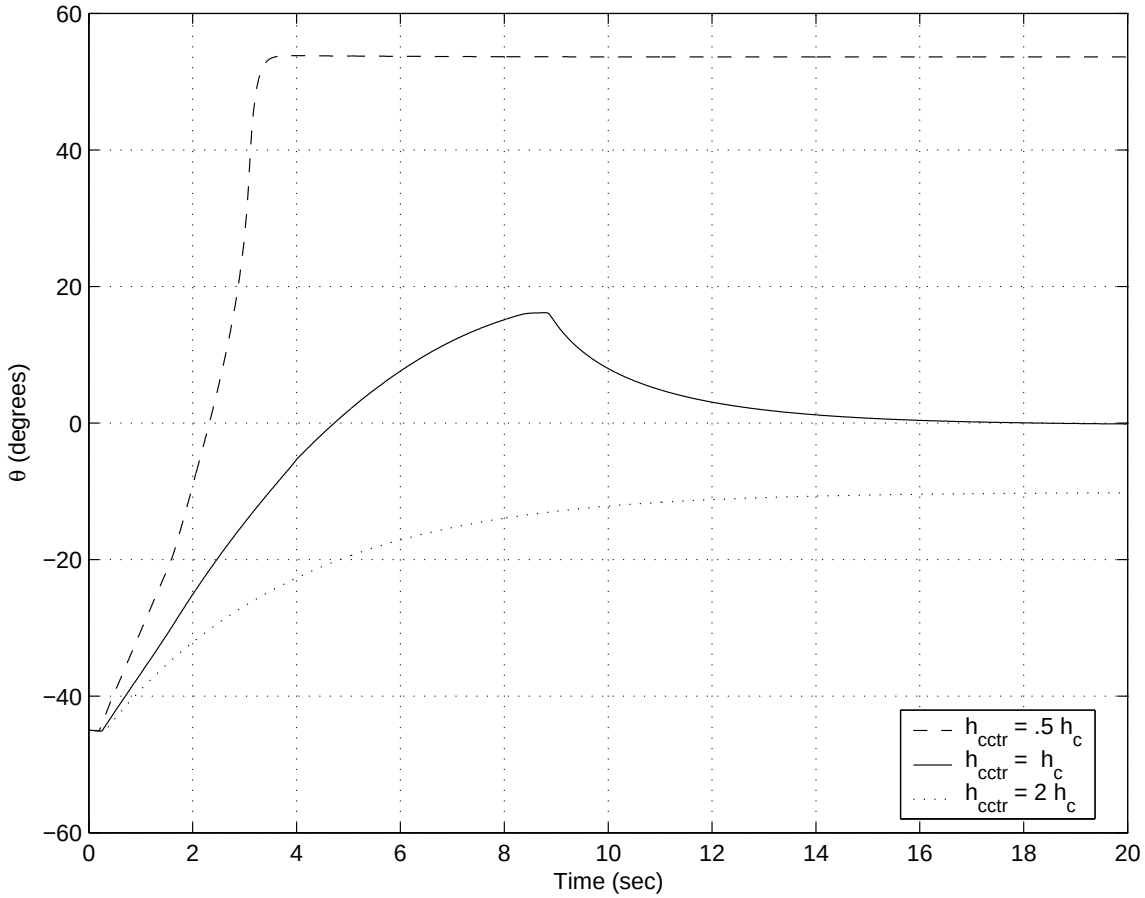

Figure 4.25: Robustness of the backstepping controller, effect of choosing different values for convection heat transfer coefficient, in the controller and the model

4.9 Summary

In this chapter we used the SMA-actuated robotic arm, which is modeled in Chapter 3, to demonstrate the general control challenge of the SMA actuators. The underlying reason for the shape memory effect is the phase transformation that is caused by heating or cooling the SMA elements. The stress dependency of the transformation temperatures is the major difficulty of the control of such systems. Linear and nonlinear control techniques along with an estimator, based on the Extended Kalman Filter, are presented along with their simulation results. Each of these control algorithm has their own benefits that makes them more appropriate for certain SMA actuators. Model-based controllers, which make the stability analysis possible, have more complicated structure and therefore require more computational power. Moreover, design of model-based controllers for SMA actuators is based on the model of the system and its parameters. Non-model-based controllers on the other hand are mainly designed intuitively and based on the simulation and experimental results.